JOURNAL OF THE AERONAUTICAL SCIENCES

VOLUME 22 FEBRUARY, 1955 NUMBER 2

ST. LOUIS PUBLIC LIBRARY FEB 14 1955

CONTENTS

A Theoretical and Experimental Study of Shock-Tube Flows.....I. I. GLASS AND G. N. PATTERSON 73

A Method for Investigating the Influence of Flexibility of the Mounting Structure of Hydraulic Servo Systems on the Dynamic Stability Quality of Control Systems.....HANS R. FRIEDRICH 101

On Some Solutions of the Hodograph Equation Which Yield Transonic Flows Through a Laval Nozzle.....F. EDWARD EHLERS 107

On the Wake and Drag of Bluff Bodies.....ANATOL ROSHKO 124

Readers' Forum: "Differentiation of Experimental Data Using Least Squares Fitting," by Fredric F. Ehrich; "A Particular Solution of a Nonlinear Differential Equation Which Occurs in the Dynamics of Conservative Systems and Its Application to Undamped Airplane Motion," by Eugene Covert; "Further Comments on 'The Effect of Boundary Layer on Sonic Flow Through an Abrupt Cross-Sectional Area Change,'" by Robert S. Wick; "Determining the Mode Shapes and Frequencies of Low Aspect Ratio Multispar Wings," by Marvin L. Stein; "Slender Bodies of Low Wave Drag," by R. N. Haskell and G. C. Grogan; "Difference Solution of Shock Diffraction Problem," by H. F. Ludloff and M. B. Friedman; "On the Design of Two-Dimensional Supersonic Nozzles by the Method of Characteristics," by Bernard Chaix and Peter Henrici; "Some Corrections and Further Contributions to 'Ripple-Type Buckling of Sandwich Columns,'" by A. E. Eringen.....133–144

Published by

INSTITUTE OF THE AERONAUTICAL SCIENCES, INC.

JOURNAL OF THE AERONAUTICAL SCIENCES

Editor: HUGH L. DRYDEN, *Director, NACA*

Associate Editor: ROBERT R. DEXTER *Managing Editor:* BERNEICE H. JARCK

Editorial Committee

Aerodynamics

Dean R. Chapman
Francis H. Clauser
Antonio Ferri
Alexander Flax
R. Paul Harrington
R. T. Jones
Carl Kaplan
H. W. Liepmann
C. C. Lin
H. F. Ludloff
Harold Luskin
John R. Markham
Clark B. Millikan
Shatswell Ober
W. Bailey Oswald
C. D. Perkins
Elliott G. Reid
H. J. E. Reid
Russell Robinson
George S. Schairer
G. B. Schubauer
W. R. Sears
John Stack
Theodore Theodorsen
Th. von Kármán

Air Transport

Charles Froesch
J. A. Herlihy
R. D. Kelly
Otto E. Kirchner
Jerome Lederer
John C. Leslie
R. Dixon Speas

Flight Testing

R. R. Gilruth
Melvin N. Gough
W. L. Howland
W. F. Milliken, Jr.
E. G. Stout

Structures and Materials

W. B. Bleakney
E. W. Conlon
John E. Duberg
E. C. Hartmann
N. J. Hoff
Samuel Levy
J. F. McBrearty
Alfred S. Niles
W. Ramberg
F. R. Shanley
C. R. Strang
S. Timoshenko
H. S. Tsien
Chi-Teh Wang

Rotating Wing Aircraft

F. B. Gustafson
K. H. Hohenemser
Bartram Kelley
R. B. Maloy
Ralph McClarren
R. H. Miller
R. H. Prewitt
Igor I. Sikorsky

Vibration and Flutter

Lee Arnold
M. A. Biot
R. L. Bisplinghoff
William Bollay
Chieh-Chien Chang
J. P. Den Hartog
I. E. Garrick
Martin Goland
Theodore Theodorsen

Aircraft Design

W. E. Beall
E. H. Heinemann
Hall L. Hibbard
Richard Hutton
C. L. Johnson
A. A. Kartveli
E. G. Stout
F. K. Teichmann
Robert J. Woods

Electronics in Aviation

Welcome W. Bender
K. C. Black
M. V. Kiebert, Jr.
David S. Little
S. B. Rogers
Paul Rosenberg
L. M. Sherer

Physiologic Problems

H. G. Armstrong
Louis H. Bauer
Robert J. Benford
W. Randolph Lovelace, II
Ross A. MacFarland

Fuels and Oils

D. P. Barnard
J. H. Doolittle
Graham Edgar
R. T. Goodwin
A. M. Rothrock

Flight Propulsion

George W. Brady
Frank W. Caldwell
L. S. Hobbs
E. E. Johnson
Joseph Keenan
R. P. Kroon
Hans Reissner
Abe Silverstein
C. Fayette Taylor
E. S. Taylor
P. B. Taylor
E. S. Thompson
H. S. Tsien

Instruments

Allan G. Binnie
Charles H. Colvin
Frank R. Cook
C. S. Draper
S. G. Eskin
O. E. Esval
C. F. Savage
R. C. Sylvander

Meteorology

C. F. Brooks
D. M. Little
F. W. Reichelderfer
K. C. Spengler

SUBSCRIPTION RATES

JOURNAL OF THE AERONAUTICAL SCIENCES, Published Monthly.—United States and Possessions: 1 Year, $12.00; Single Copies, $1.50. Foreign Countries Including Canada (American Currency Rates): 1 Year, $13.00; Single Copies, $1.50.

AERONAUTICAL ENGINEERING REVIEW, Published Monthly.—United States and Possessions: 1 Year, $3.00; Single Copies, $0.50. Foreign Countries Including Canada (American Currency Rates): 1 Year, $3.50; Single Copies, $0.50.

Notices of change of address should be sent to the Institute at least 30 days prior to actual change of address.

Manuscripts for publication, proofs, and all correspondence should be addressed to the Editorial Office of the JOURNAL.

Correspondence regarding subscriptions may be addressed to Publication Office, 20th and Northampton Sts., Easton, Pa., or to the Editorial Office of the JOURNAL OF THE AERONAUTICAL SCIENCES, 2 East 64th Street, New York 21, N.Y.

Copyright, 1955, by the Institute of the Aeronautical Sciences, Inc.

Entered as Second Class Matter at the Post Office, Easton, Pa., May 1, 1937. Acceptance for mailing at a special rate of Postage provided for in the Act of August 24, 1912. Authorized April 29, 1937.

rec
nur
cha
stu
wa
son
effe
rela
kin
ato
net
ogr
abl
zer
der
of
sho
it t
cou
exp
din
at t
are
pro
sim
sho
and
tiv
wa
of
and
end
the
lac
En
Aer

JOURNAL OF THE AERONAUTICAL SCIENCES

VOLUME 22 FEBRUARY, 1955 NUMBER 2

A Theoretical and Experimental Study of Shock-Tube Flows

I. I. GLASS* AND G. N. PATTERSON†

Institute of Aerophysics, University of Toronto, Canada

SUMMARY

During the past 10 years the shock tube has achieved singular recognition as the most important facility for the investigation of numerous fundamental problems in nonstationary fluid mechanics. The shock tube has been applied successfully to the studies of the transition through shock waves and contact fronts; wave interactions; flows in the subsonic, transonic, and supersonic flow régimes; wave diffraction and refraction; condensation effects; sound speed measurements; shock loading of structures; relaxation phenomena in gases; flame propagation; chemical kinetics; boundary-layer growth and shock-wave attenuation; atomic physics of states behind strong shock waves and magneto-hydrodynamics. (See reference 1 for an extensive bibliography.) Thermodynamic states of short duration are available that have a range of physical quantities from nearly absolute zero pressures, temperatures, and densities to high pressures, densities, and temperatures, the latter being of the order of tens of thousands of degrees Kelvin. This wide utilization of the shock tube for basic research work almost tempts one to rename it the "test tube" of nonstationary fluid mechanics.

The purpose of the present paper is to give an integrated account of the shock tube and some of the recent theoretical and experimental studies of shock-tube flows.

The reported data for real flows are based mainly on the one-dimensional, nonstationary research work that was conducted at the Institute of Aerophysics during the past 5 years. Included are theoretical and experimental investigations of the origin problem, total shock-wave attenuation, normal shock reflection, simple and double shock wave refraction, head-on collision of shock waves, head-on collision of shock and rarefaction waves, and the overtaking of two shock waves. In addition, qualitative experiments are presented on normal reflection of rarefaction waves, double refraction of rarefaction waves, head-on collision of rarefaction waves, head-on collision of shock and wire screens, and the emergence of shock and rarefaction waves from the open ends of a shock tube into the free atmosphere.

A comparison is made between theory and experiment, and the deviations are discussed. Where a theoretical treatment is lacking, the experiments are analyzed qualitatively and the flow quantities, determined from wave speed measurements, are indicated.

Received May 11, 1954.

* Research Associate and Assistant Professor of Aeronautical Engineering.

† Director, Institute of Aerophysics, and Head, Department of Aeronautical Engineering.

NOTATION

a	= speed of sound
c	= x/t, a characteristic in the (x, t)-plane
e	= internal energy per unit mass
m	= mass flow
p	= pressure
t	= time
u	= particle velocity
w	= speed of shock wave
x	= position along shock tube measured from diaphragm
ρ	= density
λ	= mean free path
μ	= viscosity
ν	= kinematic viscosity
η	= entropy
C_p	= coefficient of specific heat at constant pressure
C_v	= coefficient of specific heat at constant volume
L	= chamber length
M	= flow Mach Number
Re/l	= Reynolds Number per foot
T	= temperature
A_{ij}	= a_i/a_j
C_{ij}	= c_i/a_j
E_{ij}	= $e_i/e_j = (C_vT)_i/(C_vT)_j = \kappa_{ij}T_{ij}$
M_i	= u_i/a_i
P_{ij}	= p_i/p_j
T_{ij}	= T_i/T_j
U_{ij}	= u_i/a_j
W_{ij}	= w_i/a_j
α_i	= $(\gamma_i + 1)/(\gamma_i - 1)$
β_i	= $(\gamma_i - 1)/2\gamma_i$
γ_i	= $(C_p/C_v)_i$
κ_{ij}	= c_{v_i}/c_{v_j}
τ	= a_4t/L
Γ_{ij}	= ρ_i/ρ_j
n	= x/a_4t
X	= x/L
$\overrightarrow{S}$	= forward facing shock wave (particles enter from right)

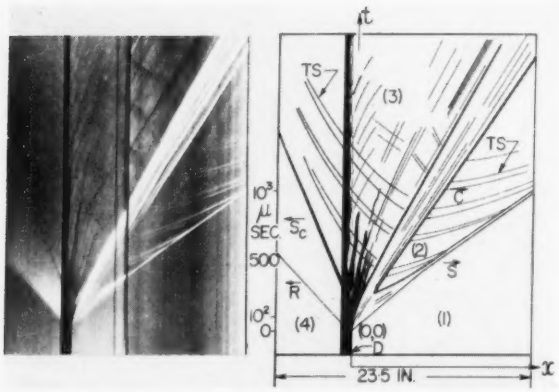

PLATE 1. The wave system produced in a real shock tube from the instant the diaphragm ruptures.

p_4 = 1,500 mm. Hg
$a_{4,1}$ = 1,132 ft. per sec.
P_{21} = 2.1
p_1 = 300 mm. Hg
W_{11} = 1.39
P_{41} = 5.00
U_{21} = 0.60
M_2 = 0.50
M_s = 0.65
S = shock wave
C = contact surface
R = rarefaction wave
D = diaphragm
TS = transverse shocks
S_c = condensation shock

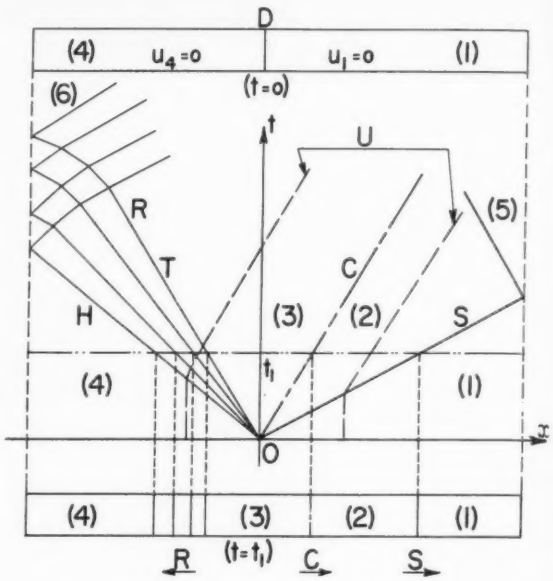

FIG. 1. Theoretical diagram of the (x, t)-plane showing the waves and states in the chamber and channel from the instant the diaphragm ruptures. U = particle path, D = diaphragm, H = head of rarefaction wave, and T = tail of rarefaction wave.

TABLE 1
Flow Quantities for Very Strong Shock Waves

(a) Case Air/Air

$P_{14} = 0$, $\alpha = 6$, $\beta = \frac{1}{7}$ * = indeterminate

E_{14}	P_{21}	Γ_{34}	A_{34}	T_{34}	Γ_{21}	A_{21}	T_{21}	W_{11}	U_{34}	U_{21}	M_3	M_2	C_{34}
0	∞	*	*	*	6	∞	∞	∞	*	∞	*	1.89	*
0.1	422	0	0	0	5.92	8.45	71.4	19.0	5	15.8	∞	1.87	5
1.0	44	0	0	0	5.30	2.88	8.30	6.16	5	5.0	∞	1.73	5

(b) Case He/Air

$P_{14} = 0$, $\alpha_1 = 6$, $\beta_1 = \frac{1}{7}$ $\alpha_4 = 4$, $\beta_4 = \frac{1}{5}$ $T_4 = T_1$

E_{14}	P_{21}	Γ_{34}	A_{34}	T_{34}	Γ_{21}	A_{21}	T_{21}	W_{11}	U_{34}	U_{21}	M_3	M_2	C_{34}
.231	132	0	0	0	5.75	4.79	23.0	10.6	3.00	8.83	∞	1.84	3

(c) Case H_2/N_2

$P_{14} = 0$, $\alpha = 6$, $\beta = \frac{1}{7}$ $T_4 = T_1$

E_{14}	P_{21}	Γ_{34}	A_{34}	T_{34}	Γ_{21}	A_{21}	T_{21}	W_{11}	U_{34}	U_{21}	M_3	M_2	C_{34}
.0735	574	0	0	0	5.94	9.82	96.5	22.2	5	18.5	∞	1.88	5

$\overleftarrow{R}$ = backward facing rarefaction wave (particles enter from left)

$\overrightarrow{C}$ = contact front moving to the right

He|Air = helium and air separated by a diaphragm in a shock tube

He||Air = helium and air separated by a contact front

Introduction

The shock tube was first utilized in France by Vieille in 1890, for flame propagation experiments. Its application was improved considerably by Payman and Shepherd, during the period of 1931 to 1943. The most recent and fruitful applications of the shock tube were made at universities and government laboratories. Noted among these are Princeton, Michigan, Toronto, Cornell, Lehigh, Brown, Johns Hopkins, NACA and NOL. The pioneering work of Prof. Walker Bleakney and his associates at Princeton has contributed directly to the development of this field of research on this continent.

The photographic records used to illustrate the various flow phenomena were obtained from the 2- by 7-in. shock tube and the 3- by 3-in. wave interaction tube at the Institute of Aerophysics.

Part (1) Theoretical Aspects

(1.1) Relevant Wave Theory

The theory of the shock tube is given in some detail in references 1 and 2. As a result only the basic concepts and fundamental equations will be presented here. The simple shock tube consists of a straight tube of uniform cross section containing a diaphragm which separates two compartments (Fig. 1). One compartment (4) is filled with a gas at a high pressure and is designated as the high pressure chamber (or simply the chamber), the other (1) contains a gas at a lower pressure and is called the low-pressure chamber (or the channel). Initially, the two gases are in thermal equilibrium. When the diaphragm is ruptured in the ideal shock tube, a wave system is generated, and its representation on the (x, t)-plane is as shown on Fig. 1. This wave model may be deduced theoretically from a discussion of the transition relations for shock fronts and rarefaction waves by utilizing the (p, u)-plane for their representation.[1] The postulated wave system is also observed in real flows, but it is of a modified form. The real flow that appears on the (x, t)-plane schlieren photograph of Plate 1 differs in many details from the idealized flow shown on Fig. 1. Theoretically, it is assumed that the diaphragm is instantaneously and completely removed at time $t = 0$. As a result a plane shock wave followed by a contact surface is instantly transmitted into the channel and a centered rarefaction wave is propagated into the chamber. The rarefaction wave is represented as a pencil of straight lines (Mach waves or characteristic lines) emanating from the origin. The flow quantities are constant along each Mach line but vary from line to line. Consequently state (2), which is compressed by the shock wave, and state (3), which is formed from the isentropic expansion of the gas in the chamber through the rarefaction wave, are uniform regions. The particle velocity and the pressure in the two uniform states are identical. However, because of the different formative processes involved, the temperature, density, and entropy of the two states are different. Essentially, they contain dissimilar gases and are therefore separated by a contact surface. If the specific heats are assumed to remain constant, then the wave speeds and the properties of the uniform states are readily determined from the initial conditions by matching the unsteady isentropic rarefaction wave values of the pressure and the velocity with those of the steady, irreversible adiabatic shock-wave relations. The utilization of these ideal conditions is justified from experimental evidence, and as a result equations may be derived which determine all of the flow properties. The theoretical basis for the following relations is discussed in reference 1. It will be noted that only the initial conditions and the shock strength are required for the calculation of the physical quantities of the flow.

(a) The Strength of the Shock Wave (P_{21}) as a Function of the Initial Conditions.—

$$P_{14} = \frac{1}{P_{21}}\left[1 - (P_{21} - 1)\sqrt{\frac{\beta_4 E_{14}}{\alpha_1 P_{21} + 1}}\right]^{1/\beta_4} \qquad (1)$$

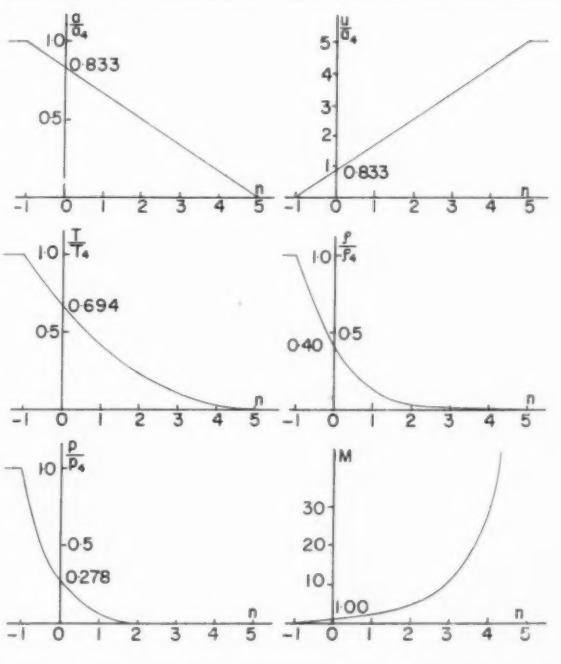

Fig. 2. Transition front profiles through a complete centered rarefaction wave showing the various flow parameters. Note: The incomplete centered rarefaction wave profiles are identical in shape up to the tail of the wave.

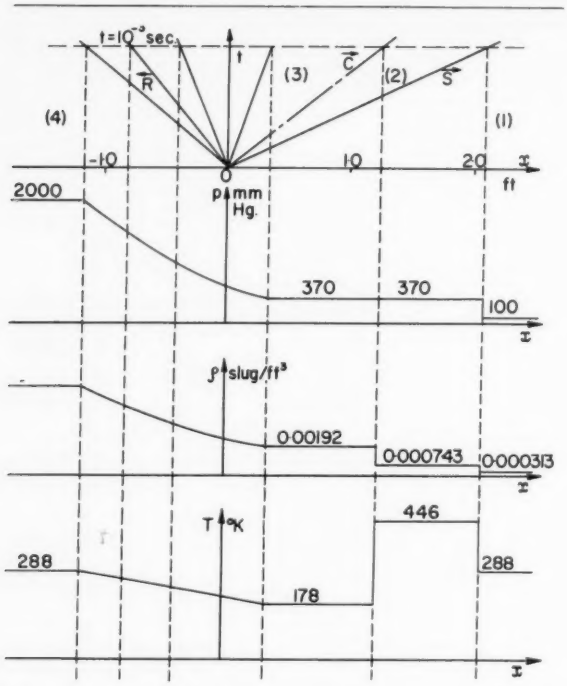

FIG. 3(a). Variation of flow properties p, ρ, T along a shock tube. Initial conditions: $t = 10^{-3}$ sec., $T = 288°$K., $p_1 = 100$ mm. Hg, and $P_{41} = 20$. Case: Air |Air.

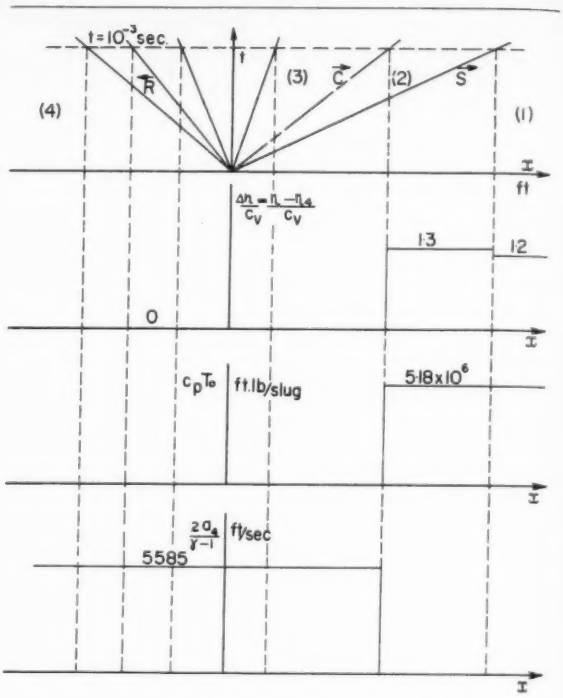

FIG. 3(c). Variation of flow properties $\Delta\eta/C_v$, C_pT_0, $2a_4/(\gamma - 1)$ along a shock tube.

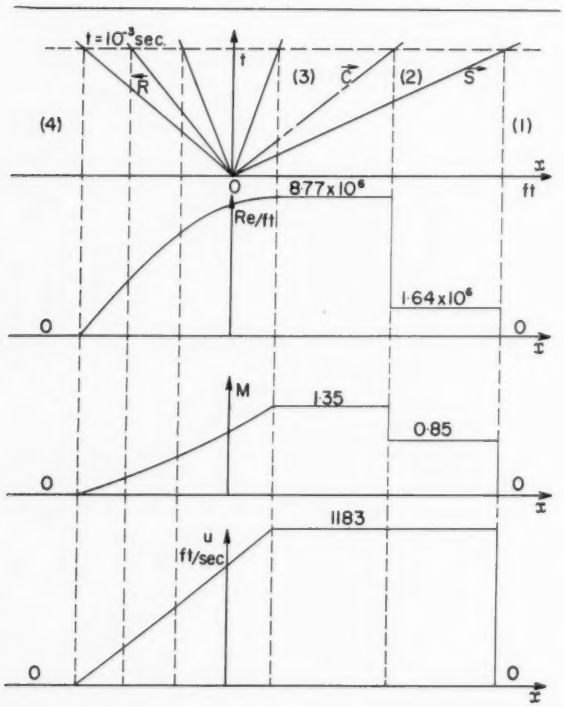

FIG. 3(b). Variation of flow properties Re per ft., M, u, along a shock tube.

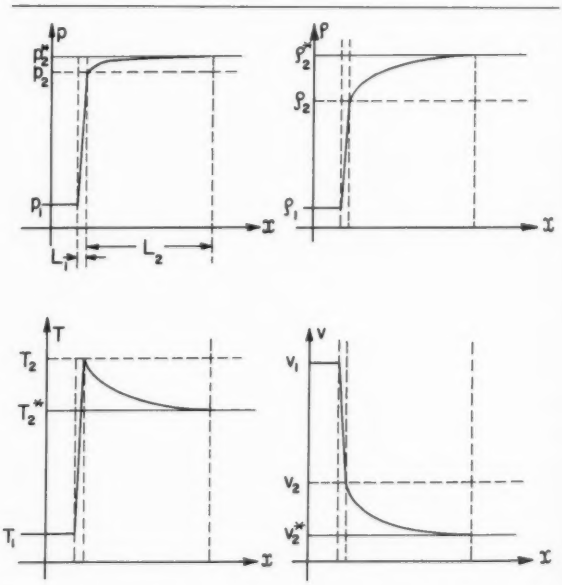

FIG. 4. Representation of the transition through a strong shock front.

---------- Rankine-Hugoniot value (active degrees)
———— equilibrium value (active and inert degrees)
L_1 = shock thickness due to active degrees
L_2 = shock thickness due to inert degrees

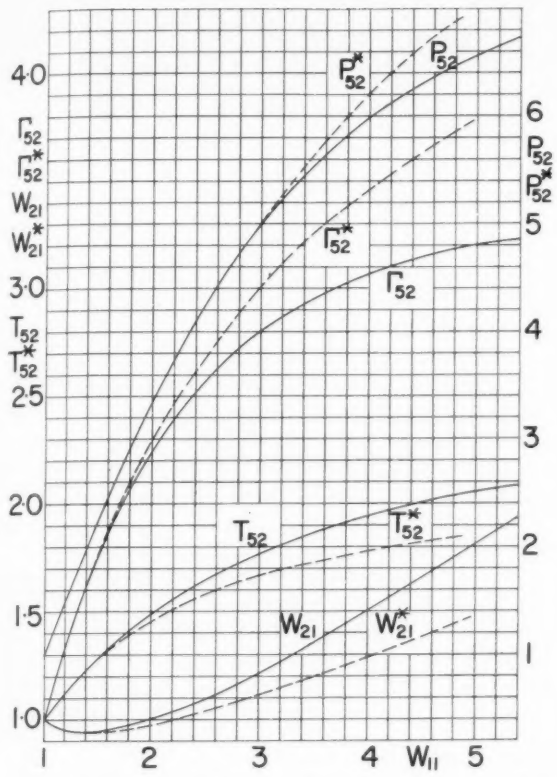

FIG. 5. Variations of the flow parameters in air behind a normal reflected shock wave with the incident shock-wave Mach Number (W_{11}).

Eq. (1) indicates that the shock pressure ratio (P_{21}) is a function of the diaphragm pressure ratio (P_{14}), the internal energy ratio across the diaphragm (E_{14}), and the specific heat ratios of the gases in the chamber (γ_4) and in the channel (γ_1).

An examination of Eq. (1) shows that there is a limit to the shock strength that may be produced even with infinite diaphragm pressure ratios, and for the case where $E_{14} \leq 1$,

$$[P_{21}]_{P_{14}=0} \backsimeq 1 + (\alpha_1/\beta_4 E_{14}) \tag{2}$$

Thus the criteria for strong shock waves produced in a simple shock tube are:

(1) A large diaphragm pressure ratio, $P_{14} \rightarrow 0$.

(2) A small energy ratio across the diaphragm, $E_{14} \rightarrow 0$.

This immediately suggests the use of such gas combinations as He|Air, H_2|A, or H_2|SF_6 which give a small E_{14} value. Heating the chamber and cooling the channel to further reduce E_{14} is possible but not practical. Subsequently, other methods employed for this purpose will be discussed.

(*b*) *The Density Ratios.*—

$$\Gamma_{34} = [P_{14}P_{21}]^{1/\gamma_4} \tag{3}$$

$$\Gamma_{21} = (1 + \alpha_1 P_{21})/(\alpha_1 + P_{21}) \tag{4}$$

(*c*) *Speed of Sound and Temperature Ratios.*—

$$A_{34} = T_{34}^{1/2} = P_{34}^{\beta_4} = [P_{14}P_{21}]^{\beta_4} \tag{5}$$

$$A_{21} = T_{21}^{1/2} = \left[\frac{P_{21}(\alpha_1 + P_{21})}{1 + \alpha_1 P_{21}}\right]^{1/2} \tag{6}$$

(*d*) *Shock Wave Velocity or Mach Number.*—

$$W_{11} = [\beta_1(1 + \alpha_1 P_{21})]^{1/2} \tag{7}$$

(*e*) *Contact Surface or Particle Velocity.*—

$$U_{21} = (P_{21} - 1)/\gamma_1[\beta_1(\alpha_1 P_{21} + 1)]^{1/2} \tag{8}$$

$$U_{34} = (1/\gamma_4\beta_4)\,[1 - (P_{14}P_{21})^{\beta_4}] \tag{9}$$

(*f*) *Velocity of Head and Tail of Rarefaction Wave.*—

$$\left.\begin{aligned} &\text{Head:}\quad C_{44} = -1 \\ &\text{Tail:}\quad C_{34} = (1/\gamma_4\beta_4)\,[1 - (P_{14}P_{21})^{\beta_4}] - [P_{14}P_{21}]^{\beta_4} \end{aligned}\right\} \tag{10}$$

(*g*) *Local Mach Numbers.*—

$$M_3 = (1/\beta_4\gamma_4)\,[(P_{14}P_{21})^{-\beta_4} - 1] \tag{11}$$

$$M_2 = (P_{21} - 1)/\gamma_1[\beta_1 P_{21}\,(\alpha_1 + P_{21})]^{1/2} \tag{12}$$

(*h*) *Local Reynolds Numbers.*—If the relation $\mu \propto T^k$ is utilized, then, for air ($k = 0.76$),

$$(Re/l)_2 = \frac{\gamma_4}{\mu_4 a_4} P_{41}\, p_1 \frac{\Gamma_{34} U_{34}}{T_{34}^{0.76}} \tag{13}$$

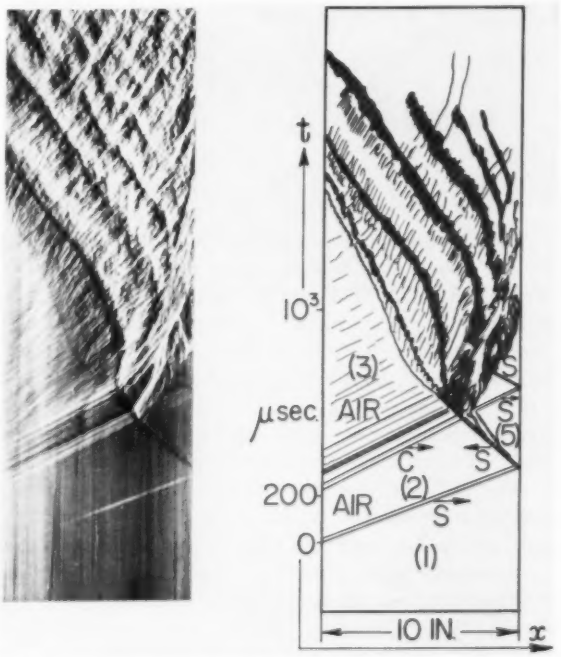

PLATE 2. Normal reflection, refraction, and progression of a shock wave through the cold region behind the contact front.

p_4 = 3.068 mm. Hg
p_1 = 20 mm. Hg
P_{41} = 153
P_{21} = 7.2
a_1 = 1,136 ft. per sec.
W_{11} = 2.34
U_{21} = 1.76
M_3 = 2.7
M_2 = 1.46

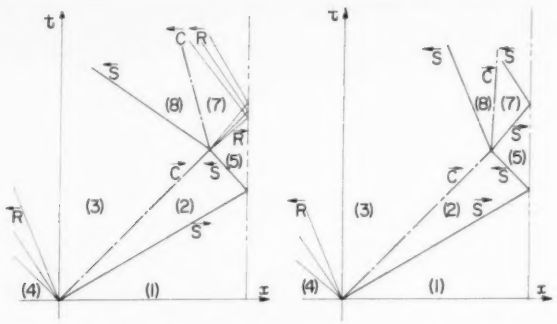

FIG. 6. Interaction of a shock wave and a contact surface.

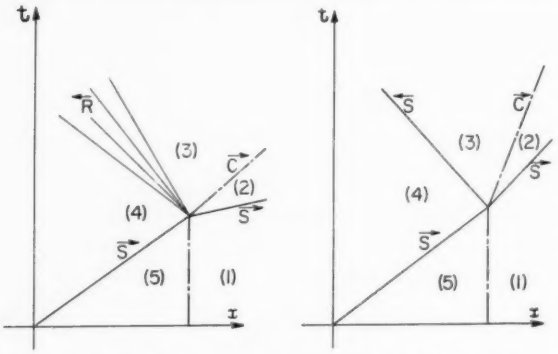

FIG. 7. The interaction of a shock wave and a stationary contact surface.

$$(Re/l)_2 = \frac{\gamma_1}{\mu_1 a_1} p_1 \frac{\Gamma_{21} U_{21}}{T_{21}^{0.76}} \tag{14}$$

$$\frac{(Re/l)_3}{(Re/l)_2} = P_{41} \frac{\Gamma_{34}}{\Gamma_{21}} \left(\frac{T_{21}}{T_{34}}\right)^{0.76} \tag{15}$$

The limiting values of the flow quantities as predicted by the above equations are given in Table 1. An examination of Table 1 reveals that the uniform states (2) and (3) possess extreme flow conditions. Very high temperatures and low Mach Numbers prevail in state (2), while very high Mach Numbers and low temperature are theoretically attainable in state (3). The attainability of such states immediately suggests that the uniform states may be employed for aerodynamic testing. So far, this has not been achieved because of the lack of reliable, rapid-response instruments that can measure directly the physical quantities of a flow of extremely short duration. Furthermore, it has not been established whether it is valid to apply nonstationary flow test results, which do not possess fully developed thermal and velocity boundary layers, to stationary flow problems.

(*i*) *Transition Properties of a Centered Rarefaction Wave Moving to the Left* (*Fig. 1*).—

$$x/t = u - a \tag{16}$$

$$u + [2a/(\gamma_4 - 1)] = 2a_4/(\gamma_4 - 1) \tag{17}$$

$$a/a_4 = 1 - [(n + 1)/\alpha_4] \tag{18}$$

$$T/T_4 = \{1 - [(n + 1)/\alpha_4]\}^2 \tag{19}$$

$$\rho/\rho_4 = \{1 - [(n + 1)/\alpha_4]\}^{1/\gamma_4\beta_4} \tag{20}$$

$$p/p_4 = \{1 - [(n + 1)/\alpha_4]\}^{1/\beta_4} \tag{21}$$

$$M = (n + 1)/(1 - \beta\gamma n) \tag{22}$$

The profiles are plotted on Fig. 2. It is seen that the shape of a rarefaction wave is fixed by the initial conditions in the chamber, and its extent depends on the diaphragm pressure ratio. When the diaphragm pressure ratio is infinite, a complete centered wave results, and the extent of the profile is complete—that is, the density, temperature, pressure, and speed of sound are zero; the particle velocity is $5a_4$; and the Mach Number is infinite at the tail of the wave. For incomplete centered rarefaction waves, all the derivatives are discontinuous at the tail and at the head of the wave. For a complete wave all the derivatives are discontinuous at the head of the wave only. At the tail of the wave they are zero for the density, pressure, and temperature, so that these profiles are tangent to the n-axis. The derivatives for the speed of sound and particle velocity are finite. The Mach Number derivative is infinite.

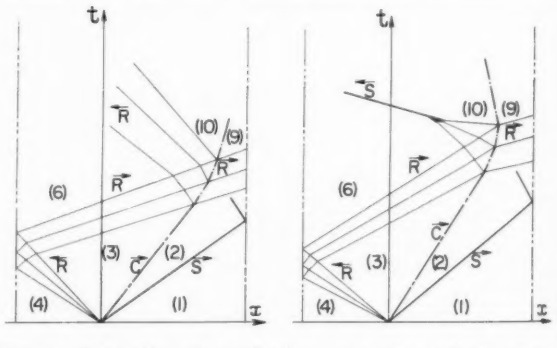

FIG. 8. Interaction of a rarefaction wave and a contact surface.

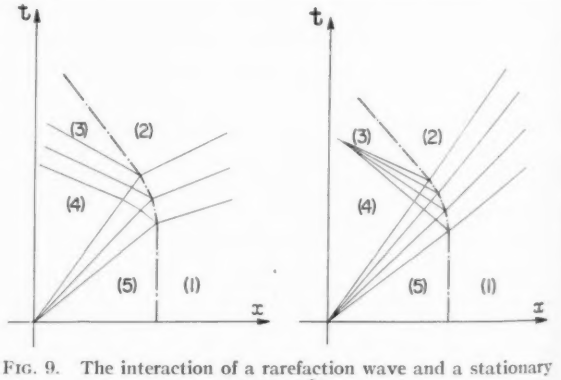

FIG. 9. The interaction of a rarefaction wave and a stationary contact surface.

A typical set of transition profiles drawn to a scale for the shock tube when $P_{41} = 20$, case Air | Air is shown on Fig. 3. The temperature discontinuity at the contact surface will give rise to a molecular transfer of heat between regions (2) and (3). The transition through the contact front is analogous to that of a shock front and requires the solution of a set of nonlinear equations in heat conduction.[3]

It should be noted that the greatest entropy change exists across the contact surface and arises from the fact that state (4) has an entropy that is much lower than state (1).

The matching of the pressure and velocity from the steady and unsteady solutions for the shock and rarefaction wave, respectively, gives rise to two conserved flow parameters on either side of the contact surface—i.e., the energy constant C_pT_0 for states (1) and (2), and the momentum constant $[2/(\gamma_4 - 1)]a_4$ for states (4) and (3).

(1.2) *Deviations in a Shock Tube Due to Variable Specific Heats*

The basic equations [Eqs. (1) to (22)] for the flow in a shock tube were derived on the assumption that the specific heats remained constant. It was shown in Table 1 that for extremely large diaphragm pressure ratios (P_{41}) and small energy ratios (E_{14}), extremely high temperatures could be achieved in state (2) and extremely low temperatures in state (3). Under these extreme temperature conditions the assumption of constant specific heat is no longer valid. For the rarefaction wave the basic equation becomes[1]

$$u_3 = u_4 + \frac{2a_4}{\gamma_4 - 1}\left[1 - \left(\frac{p_3}{p_4}\right)^{\beta_4}\Phi\right] \qquad (23)$$

where Φ is a correction that is a function of the gas properties including the deviation from constant specific heats.

The value of Φ in general is $\Phi \leq 1$, and for constant specific heat $\Phi = 1$. Thus the particle velocity (u_3) is increased as a result of the de-excitation of the rotational degrees of freedom of the molecule due to the decreased temperature. In the case of Air | Air when $P_{41} = 10{,}000$, $T_3 = 0.16 \times 300°\text{K.} = 48°\text{K.}$, which is below the boiling point of nitrogen and oxygen. Thus condensation phenomena can be expected, and constant specific heat can no longer be assumed under these conditions, which are readily obtainable in a shock tube.

For the case of the shock front, the transition profiles for constant specific heat and variable specific heat are given graphically in Fig. 4. Immediately at the shock front, the temperature jumps almost discontinuously to a high value. This is due to the fact that the active degrees of freedom (translation and rotation) are excited nearly instantaneously in the distance of a few mean free paths (λ). Since the previous equations for the shock wave were based on constant specific heat, the initial temperature jump is accurately predicted

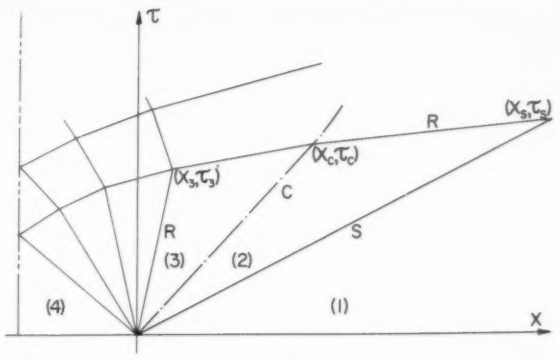

FIG. 10. Points in the (X, τ)-plane where the head of the reflected rarefaction wave overtakes the tail of the incident rarefaction wave (X_3, τ_3), the contact surface (X_c, τ_c), and the shock wave (X_s, τ_s).

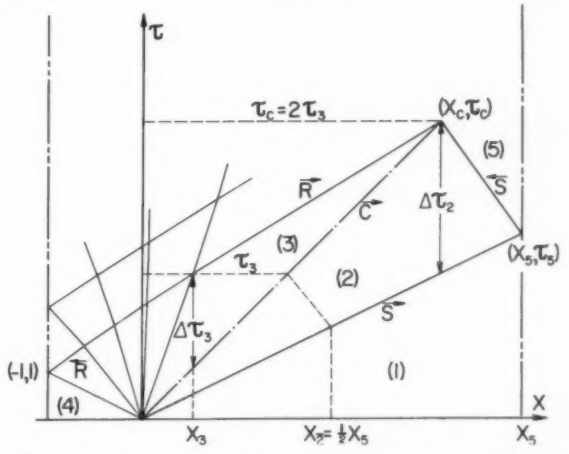

FIG. 11. Points of maximum flow duration X_3 and X_c for regions (3) and (2), respectively. $\Delta\tau_3$ = maximum flow duration for state (3). $\Delta\tau_2$ = maximum flow duration for state (2).

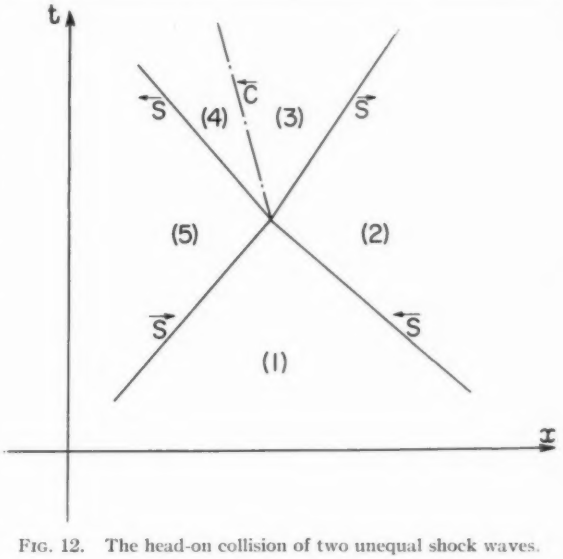

FIG. 12. The head-on collision of two unequal shock waves.

from the Rankine-Hugoniot relation [Eq. (6)]. After the initial jump, thermal equilibrium is reached in an exponential manner during the relaxation period when energy is transferred from the active to the inert degrees of freedom of the molecule (vibration, dissociation electronic excitation, and ionization). This stage is marked by a decrease in the temperature which takes place in a relatively longer time and over a greater distance than that required to excite the active degrees, and, therefore, an extended shock wave transition profile results. If it is assumed that in air the vibrational degree is the only inert degree of freedom that is excited at temperatures up to about 5,000°K., then it is possible to calculate the effects of variable specific heat by established methods (reference 4).

The deviations are as follows. Up to shock wave Mach Numbers $W_{11} \backsimeq 3$, the divergence is negligible. For $W_{11} > 3$ the deviations become monotonically greater and the temperature falls, and the density, pressure, and particle velocity rise with increasing wave Mach Number. For a given diaphragm pressure ratio the shock-wave Mach Number is somewhat smaller for the variable specific heat case. If the equilibrium values are denoted by an asterisk (*), then the above results may be expressed symbolically as

$$\rho_2^* > \rho_2,\ p_2^* > p_2,\ u_2^* > u_2,\ T_2^* < T_2, \text{ and } W_{11}^* < W_{11}$$

(1.3) Normal Reflection of Shock and Rarefaction Waves

In the previous sections the chamber and the channel were assumed to be of infinite extent. In actual shock-tube work the chamber and the channel are of finite lengths with open or closed ends. As a result, after a few milliseconds, the flow in a shock tube becomes complex because of the ensuing wave interactions.

Fig. 1 shows a simple shock-tube diagram with both ends closed and the resulting normal reflection of the rarefaction wave at the end of the chamber and the normal reflection of the shock wave at the end of the channel. Upon reflection of the shock wave, a new uniform state (5) is formed where the particle velocity behind the reflected shock is zero, but extremely high temperatures, densities, and pressures are attained. When the rarefaction wave reflects from the chamber wall, it also forms a new uniform state (6) of extremely low temperatures, densities and pressures, and zero particle velocity. It is theoretically possible to achieve a total vacuum in state (6) for Air|Air, $E_{14} = 1$, when $P_{41} = 1{,}620$ or $P_{21} = 12.6$.

The following relations apply across a normal reflected shock wave if the specific heats are assumed as constant:[1]

(*a*) *Pressure Ratio.*—

$$P_{52} = (\alpha_1 + 2 - P_{12})/(1 + \alpha_1 P_{12}) \tag{24}$$

For extremely strong shock waves $P_{12} \rightarrow 0$ and $P_{52} \rightarrow \alpha_1 + 2$.

(*b*) *Density Ratio.*—

$$\Gamma_{52} = (1 + \alpha_1 P_{52})/(\alpha_1 + P_{52}) \tag{25}$$

(*c*) *Temperature Ratio.*—

$$T_{52} = P_{52}(\alpha_1 + P_{52})/(1 + \alpha_1 P_{52}) \tag{26}$$

(*d*) *Wave Speed.*—

$$W_{21} = \frac{2 + (\alpha_1 - 1)P_{12}}{[(\alpha_1 + 1)P_{12}(\alpha_1 + P_{12})]^{1/2}} \tag{27}$$

$$W_{21}/W_{11} = [2 + (\alpha_1 - 1)P_{12}]/(\alpha_1 + P_{12}) \tag{28}$$

For extremely strong shock waves $P_{12} \rightarrow 0$ and $W_{21} \div W_{11} \rightarrow 2/\alpha_1$.

When variable specific heats are considered, Eqs. (24) to (28) are no longer applicable. The method that was utilized for the solution of incident shock wave with variable specific heats is also employed here, with the additional boundary condition that the particle velocity in state (5) behind the reflected shock wave is zero. The final results are shown on Fig. 5 for the normal reflection case without and with variable specific heats, assuming no dissociation. It will be noted that temperatures of many thousands of degrees Kelvin may be readily attained in state (5). For example, for an initial temperature of 300°K. and a wave Mach Number of 5, the variable specific heat temperature behind the reflected shock is already 3,000°K.

This region along with state (2) behind strong shock waves offers some promising possibilities in the fields of atomic physics and magneto-hydrodynamics. A typical (x, t)-plane schlieren record of a normal shock reflection appears on Plate 2.

The following equations give the properties of the uniform state (6) behind the normal reflected rarefaction wave:[1]

(*a*) *Pressure Ratio.*—

$$P_{64}^{\beta_4} = 2P_{34}^{\beta_4} - 1 = 2(P_{14}P_{21})^{\beta_4} - 1 \tag{29}$$

(*b*) *Temperature Ratio.*—

$$T_{64}^{1/2} = 2P_{34}^{\beta_4} - 1 \tag{30}$$

(*c*) *Density Ratio.*—

$$\Gamma_{64}^{\beta_4\gamma_4} = 2P_{34}^{\beta_4} - 1 \tag{31}$$

In terms of the Mach Number (M_3) in state (3), the above becomes

$$P_{64} = \left\{\frac{[2/(\gamma_4 - 1)] - M_3}{[2/(\gamma_4 - 1)] + M_3}\right\}^{1/\beta_4} \tag{32}$$

$$T_{64} = \left\{\frac{[2/(\gamma_4 - 1)] - M_3}{[2/(\gamma_4 - 1)] + M_3}\right\}^{2} \tag{33}$$

$$\Gamma_{64} = \left[\frac{[2/(\gamma_4 - 1)] - M_3}{[2/(\gamma_4 - 1)] + M_3}\right]^{1/\gamma_4\beta_4} \tag{34}$$

An (x, t)-plane schlieren record of the normal reflection of a rarefaction wave is shown on Plate 3. Only

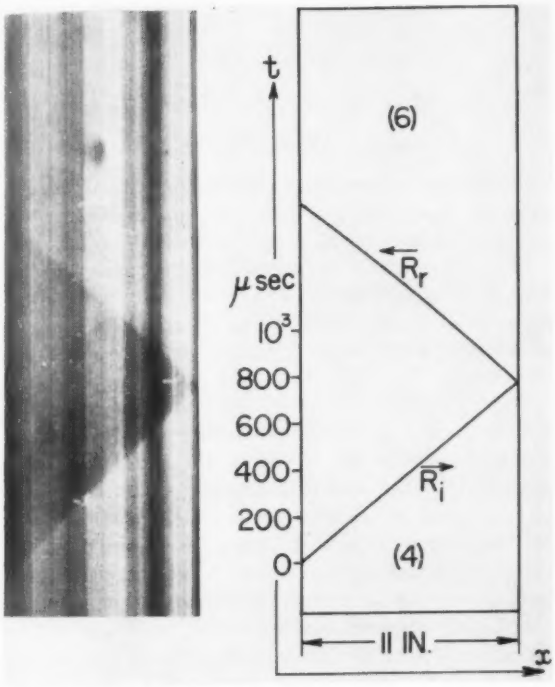

PLATE 3. Normal reflection of a rarefaction wave. Air | Air.

R_i = head of incident rarefaction wave
R_r = head of reflected rarefaction wave
P_{41} = 12.0
a_4 = 1,140 ft. per sec.
p_4 = 1,200 mm. Hg
p_1 = 100 mm. Hg

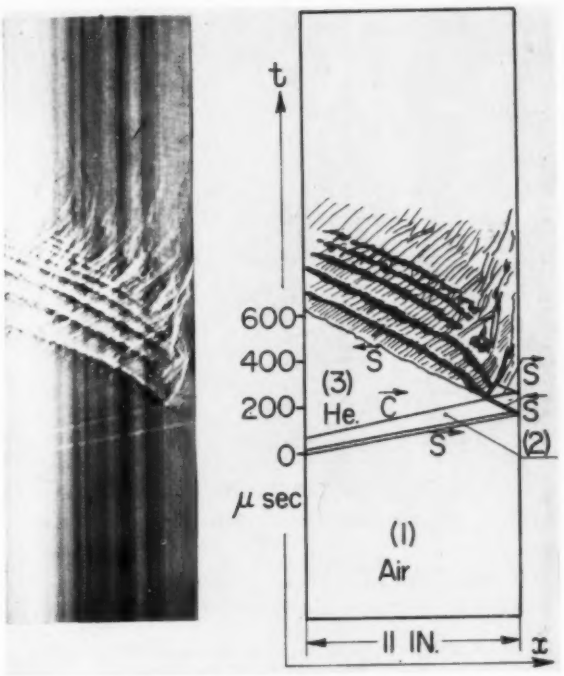

PLATE 4. Normal reflection and refraction of a shock wave at an Air|| He contact front.

S = shock wave (He) p_4 = 3,080 mm. Hg P_{21} = 27.2
C = contact surface (Air) p_1 = 4.9 mm. Hg W_{21} = 4.8
a_1 = 1,128 ft. per sec.

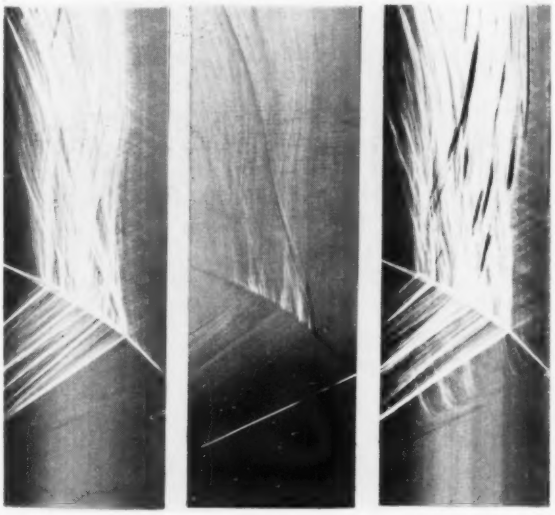

PLATE 5. The refraction of a shock wave at an Air||He contact front produced by breaking the diaphragm. P_{41} = 10, p_1 = 100 mm. Hg (Air), p_4 = 1,000 mm. Hg (He), P_{21} = 4.60, and W_{11} = 2.02.

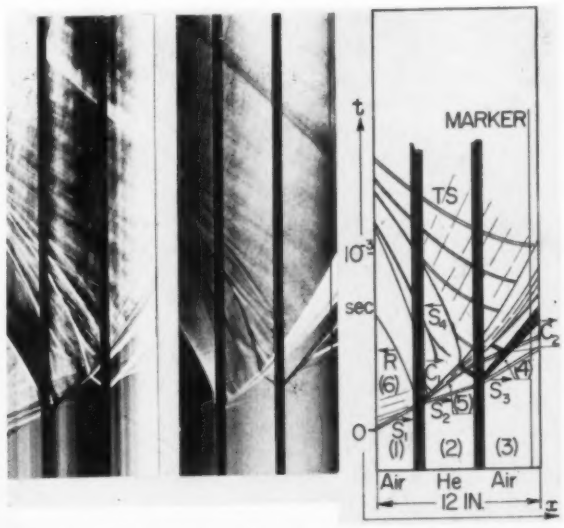

PLATE 6. The refraction of a shock wave at a layer of helium. Case: Air|| He ||Air.

S_1 = incident shock
S_2 = transmitted shock
S_3 = emergent shock
S_4 = reflected shock
R = rarefaction wave
C_1 = contact surface
C_2 = contact surface
TS = transverse shocks
$a_{1,4}$ = 1,137 ft. per sec.
$p_{1,2,3}$ = 747 mm. Hg
W_{21} = 1.82
W_{43} = 1.70
P_{21} = 3.70
P_{43} = 3.20

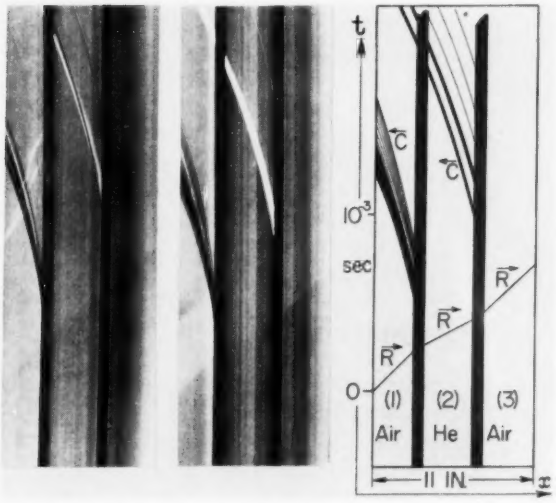

PLATE 7. The refraction of a rarefaction wave at a layer of helium.

R	= head of rarefaction wave	p_4	= 7.5 mm. Hg
C	= contact surface	P_{14}	= 100
$p_{1,2,3}$	= 754 mm. Hg	$T_{1,2,3,4}$	= 27.1°C.

the head of the wave shows up in the schlieren photograph.

(1.4) *Normal Refraction of Shock and Rarefaction Waves*

After normal reflection the shock wave eventually refracts at the contact front produced by the ruptured diaphragm. The interaction is illustrated on Fig. 6 and Plates 4 and 5.

Two cases are possible: a transmitted shock, contact front and reflected rarefaction wave, or a transmitted shock, contact front and reflected shock wave.

Mathematically it is simpler to consider this problem with a stationary contact surface. It also may be set up in this manner experimentally. The interaction is shown schematically on Fig. 7.

The case of the reflected rarefaction wave is given by the equation,[5]

$$P_{34}^{\beta_5} + f(P_{34} - P_{54}) \sqrt{\frac{\beta_5 E_{15}}{\alpha_1 P_{34} + P_{54}}} - g - 1 = 0 \quad (35)$$

where

$$f = [(\alpha_5 + P_{54})/(\alpha_5 P_{54} + 1)]^{1/2} \quad (36)$$

$$g = (1 - P_{54})\,[\beta_5/(\alpha_5 P_{54} + 1)]^{1/2} \quad (37)$$

$$E_{15} \geq (\alpha_1 + P_{54})/(\alpha_5 + P_{54}) \quad (38)$$

It is also shown that considerable attenuation or absorption of the pressure ratio across the refracted shock wave results when contact surfaces such as Air||H_2 or Air||He are employed even at room temperatures.

The case of the reflected shock wave is described by the following relation:

$$E_{15} = \frac{\alpha_1 + P_{54}P_{43}h}{(1 - P_{54}P_{43})^2}\left[k\sqrt{P_{43}} + \frac{P_{43} - 1}{\sqrt{\alpha_5 + P_{43}}}\right]^2 \quad (39)$$

where

$$h = (\alpha_5 P_{54} + 1)/(\alpha_5 + P_{54}) \quad (40)$$

$$k = (1 - P_{54})/\sqrt{\alpha_5 P_{54} + 1} \quad (41)$$

$$E_{15} \leq (\alpha_1 + P_{54})/(\alpha_5 + P_{54}) \quad (42)$$

Under these conditions the pressure ratio across the refracted shock wave is increased or amplified when contact surfaces such as Air||A or Air||CO_2 are utilized.

The problem may be extended to the case of double refraction by employing a layer of gas. This interaction is illustrated on Plate 6. A complete analysis of normal shock wave refraction may be found in reference 5.

The refraction of a rarefaction wave at a contact surface is also produced from the basic shock-tube flow as shown on Fig. 8. Here, the rarefaction wave generated by the ruptured diaphragm undergoes normal reflection at the end of the chamber and refracts at the contact surface. Two cases are possible: either a transmitted rarefaction wave and a reflected rarefaction wave, or a transmitted rarefaction wave and a reflected compression wave that steepens into a shock wave. Again the problem is simplified by considering a stationary contact surface (Fig. 9).

For a reflected rarefaction wave,

$$E_{15} = \frac{(\beta_1/\beta_5)\,[(P_{34}P_{45})^{\beta_5} - 2(P_{45})^{\beta_5} + 1]^2}{[1 - (P_{34}P_{45})^{\beta_1}]^2} \quad (43)$$

$$E_{15} \leq (\beta_1/\beta_5)\,[(1 - P_{45}{}^{\beta_5})^2/(1 - P_{45}{}^{\beta_1})^2] \quad (44)$$

For a reflected shock wave,

$$\sqrt{\frac{\beta_5}{\beta_1}}\,E_{15} = \frac{P_{45}{}^{\beta_5}\left[\dfrac{\sqrt{\beta_5}\,(1 - P_{34})}{\sqrt{\alpha_1 P_{34} + 1}}\right] + P_{45}{}^{\beta_5} - 1}{[(P_{34}P_{45})^{\beta_1} - 1]} \quad (45)$$

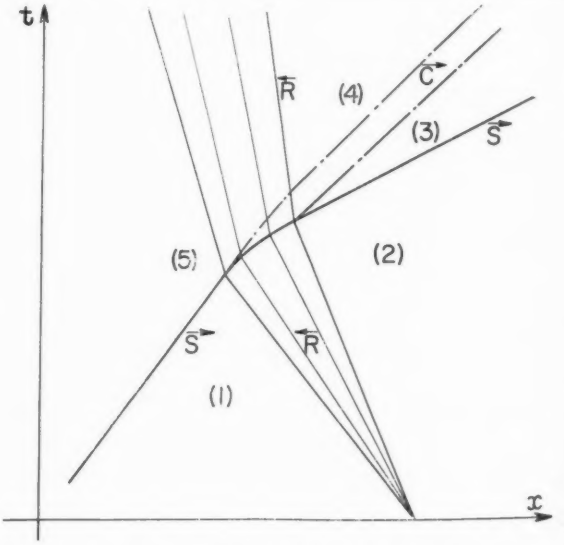

FIG. 13. The head-on collision of shock and rarefaction waves.

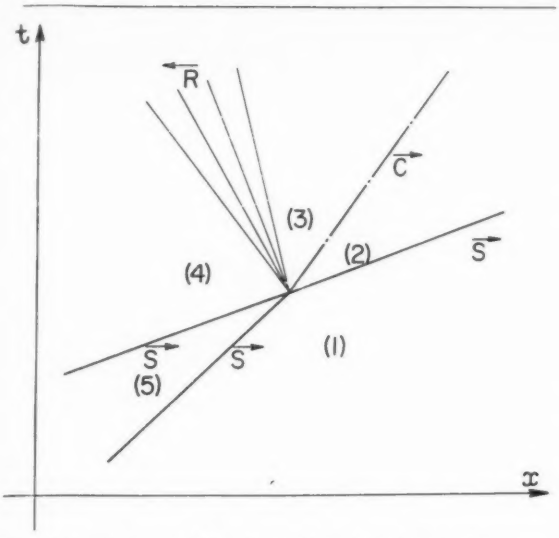

FIG. 14. The overtaking of two similarly facing shock waves.

$$E_{15} \geq (\beta_1/\beta_5)[(1 - P_{45}^{\beta_5})\ (1 - P_{45}^{\beta_1})]^2 \qquad (46)$$

In this case as well the problem may be extended to double refraction. The complete analysis of this problem will be given in a future UTIA report.

The double refraction problem for a rarefaction wave at a helium layer is illustrated by an actual schlieren photograph of the (x, t)-plane on Plate 7. The reflected waves did not appear on the records.

Another problem of interest on this record is the stability problem of a contact surface. It is seen that a contact surface of the heavy gas (air) accelerated (at 6.7×10^5 ft./sec.^{2}) into a light gas remains stable (uniformly thick Air||He contact front), whereas for the He||Air contact front, a light gas accelerated (at 2.8×10^5 ft./sec.^{2}) into a heavy gas becomes unstable.[6]

(1.5) *Optimum Chamber and Channel Lengths for a Shock Tube*

The problems of normal reflection and refraction influence the choice of optimum chamber and channel lengths. Essentially this amounts to a knowledge of the points in the flow where the reflected rarefaction wave overtakes the tail of the incident rarefaction wave (X_3, τ_3), the contact surface (X_c, τ_c), and the shock wave (X_s, τ_s). The reflected rarefaction wave eventually will destroy the flow in states (3) and (2) and will also overtake and decay the shock wave. The above points are shown on the dimensionless (X, τ)-plane in Fig. 10, and they may be determined from the following relations:[7]

$$X_3 = [\alpha_4 - 1 - \alpha_4 P_{34}^{\beta_3}]P_{34}^{-\beta_3\alpha_3/2} \qquad (47)$$

$$\tau_3 = P_{34}^{-\beta_3\alpha_3/2} \qquad (48)$$

$$X_c = 2(\alpha_4 - 1)\ [1 - P_{34}^{\beta_4}]P_{34}^{-\beta_3\alpha_3/2} \qquad (49)$$

$$\tau_c = 2\tau_3 \qquad (50)$$

$$X_s = W_{11}A_{14}\tau_s \qquad (51)$$

$$\tau_s = 2A_{21}\tau_3/(U_{21} + A_{21} - W_{11}) \qquad (52)$$

When the above relations are plotted as functions of P_{41}, it is found that shock decay starts at shorter distances from the diaphragm for low values of P_{41}. For a chamber length of 1 ft., shock decay occurs after approximately 4 ft. for He|Air and 15 ft. for Air|Air. It is essential, therefore, to use a chamber of several feet for He|Air runs in order to prevent the destruction of the flow pattern by the rarefaction wave.

An examination of Fig. 11 shows that the maximum flow duration $\Delta\tau_3$ for region (3), occurs at X_3 for all diaphragm pressure ratios (P_{41}) for which $M_3 > 1$. If $M_3 < 1$, the maximum occurs at $X = 0$. The maximum flow duration $\Delta\tau_2$ for region (2) occurs at X_c. Thus for maximum aerodynamic testing the model should be placed at X_3 and X_c. In order that the reflected shock wave does not reduce the value of $\Delta\tau_2$, the channel should be of a length X_5, such that the reflected shock meets the head of the rarefaction wave at X_c. The length X_5 is determined from the following equations:

$$\tau_c = (X_5/W_{11}A_{14}) + [(X_5 - X_c)/W_{21}A_{14}] \qquad (53)$$

$$X_5 = [\tau_c A_{14} + (X_c/W_{21})]/[(1/W_{11}) + (1/W_{21})] \qquad (54)$$

If region (3) is under investigation, then it is sufficient to use a channel length X_2, such that the reflected

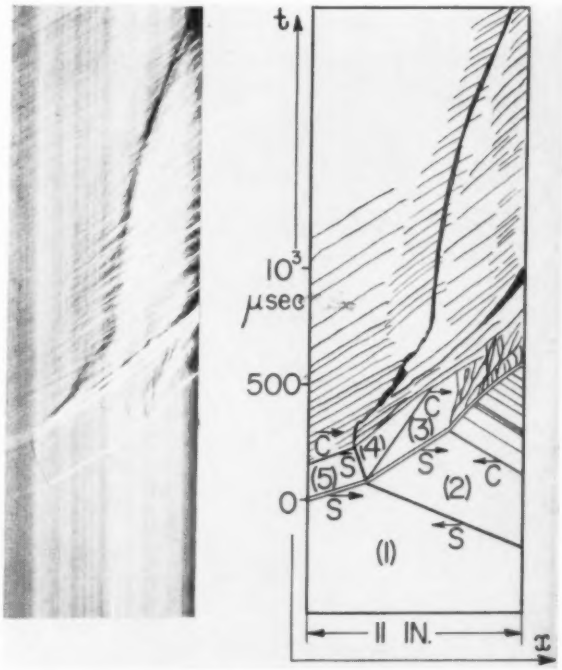

PLATE 8. Collision of two unequal shock waves in air.

$p_1 = 1.5$ mm. Hg $P_{51} = 11.13$ $P_{21} = 5.36$ $U_{21} = 0.75$
$a_1 = 1,130$ ft. per sec. $W_{31} = 3.12$ $W_{21} = 2.17$ $P_{45} = 6.50$
$P_{32} = 3.10$

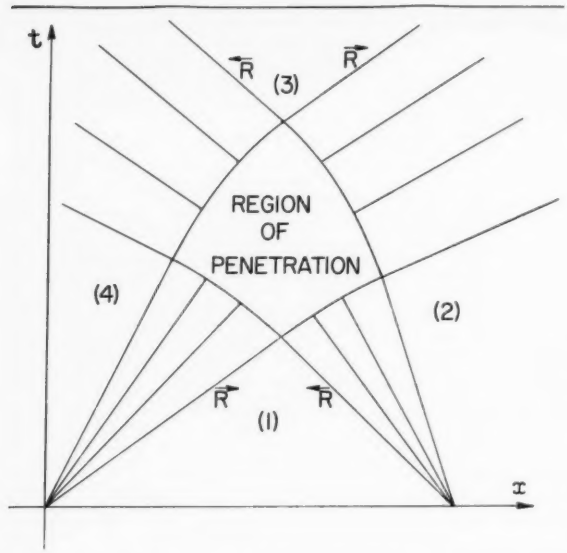

FIG. 15. The head-on collision of two unequal rarefaction waves.

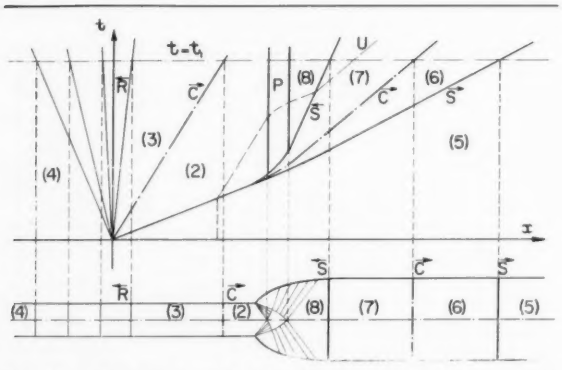

FIG. 16. The expansion of the uniform region behind the shock wave through a Busemann nozzle.

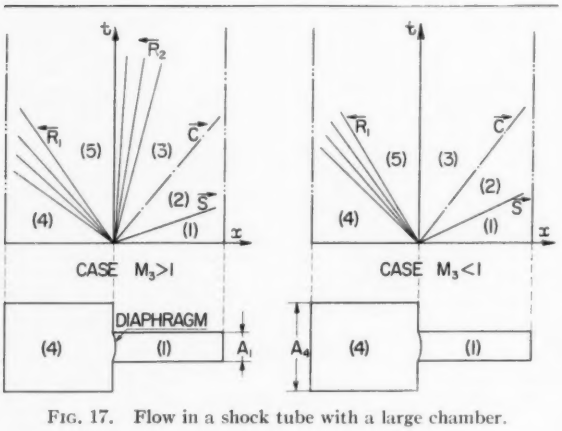

FIG. 17. Flow in a shock tube with a large chamber.

shock wave strikes the contact surface when the head of the reflected rarefaction wave overtakes the tail of the incident rarefaction wave (X_3, τ_3). This practical simplification eliminates the necessity of solving the above shock refraction relations. Since $\tau_c = 2\tau_3$, therefore,

$$X_2 = (1/2)X_5 \tag{55}$$

(1.6) *Some One-Dimensional Wave Interactions*

In addition to the previous interactions directly connected with the flows in a simple shock tube, the following interactions have been investigated by members of the Institute of Aerophysics.

(*a*) *The Head-On Collision of Two Shock Waves.*[8]—After the interaction, two receding shock waves result, separated by a contact surface, as illustrated on Fig. 12. It is desired to know the strength of the shock waves, P_{45} and P_{32}, after collision, as a function of the initial conditions in state (1) and the two incident shocks P_{51} and P_{21}. States (3) and (4), as well as the contact surface velocity, may be solved in the usual manner if the shock strengths are known. Across the contact front $p_3 = p_4$ and $u_3 = u_4$. The solution to this problem is given by

$$P_{45} = \sqrt{1 + \alpha_1 P_{45}} \times \left\{ A - C\left[B + \frac{P_{12}P_{45} - P_{15}}{\sqrt{P_{15}(\alpha_1 P_{12}P_{45} + P_{15})}} \right] \right\} + 1 \tag{56}$$

$$\left.\begin{aligned} A &= \frac{1 - P_{15}}{\sqrt{1 + \alpha_1 P_{15}}}, \qquad B = \frac{P_{12} - 1}{\sqrt{1 + \alpha_1 P_{12}}} \\ C &= \sqrt{\frac{(\alpha_1 P_{12} + 1)}{P_{12}\,(\alpha_1 + P_{12})}} \cdot \frac{P_{15}(\alpha_1 + P_{15})}{(\alpha_1 P_{15} + 1)} \end{aligned}\right\} \tag{57}$$

Since $P_{32} = P_{45} \cdot P_{12} \cdot P_{51}$, then for the case of equal shocks where $P_{15} = P_{12}$ the two roots of Eq. (56) yield the following solutions:

For the positive root,

$$P_{45} = (2 + \alpha_1 - P_{15})/(1 + \alpha_1 P_{15}) \tag{58}$$

This is identical to Eq. (24) and shows that for the collision of equal shock waves the problem is equivalent to normal reflection from a solid boundary, and no contact surface should be observed. Eq. (56) may be employed to show that for the collision of a shock and a sound wave the strength of the sound wave is increased.

For the negative root $P_{45} = P_{15}$, a linear result, which is applicable only to sonic reflection.

Actual (x, t)-schlieren photographs of the head-on collision of two unequal and equal shock waves are shown on Plates 8 and 9, respectively.

(*b*) *The Head-On Collision of Shock and Rarefaction Waves.*[9]—In the interaction illustrated in Fig. 13, the

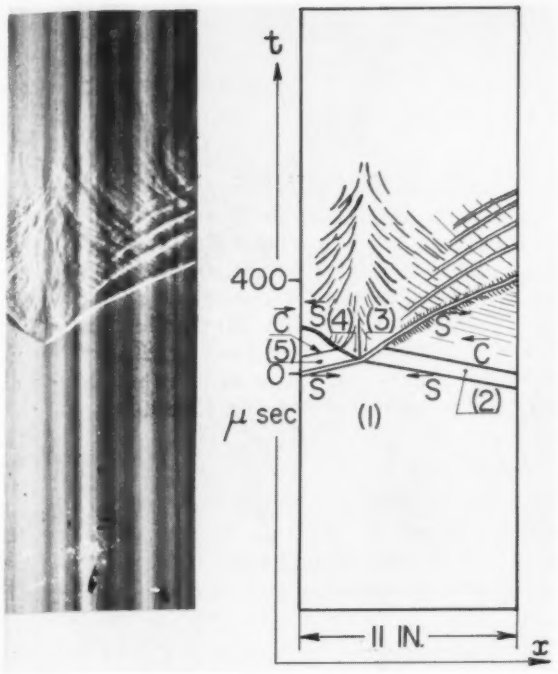

PLATE 9. Collision of equal shock waves in air. p_1 = 2.90 mm. Hg, P_{51} = 32.4 = P_{21}, W_{51} = 5.2 = W_{21}, and a_1 = 1,136 ft. per sec.

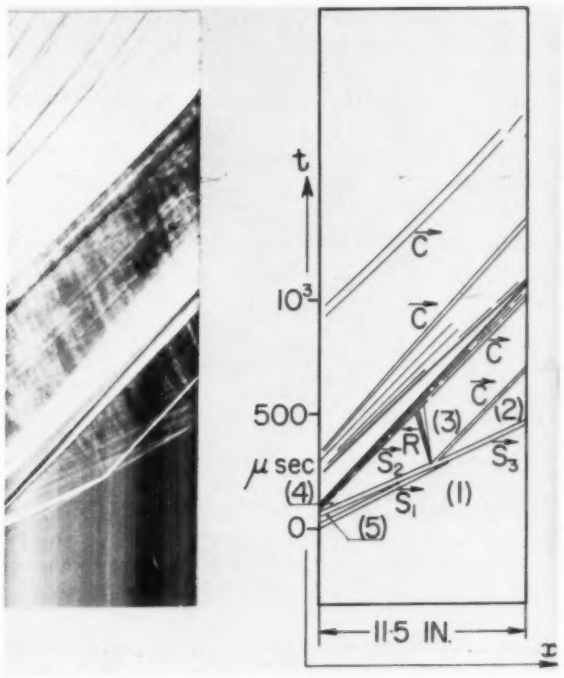

PLATE 11. The overtaking of two similarly facing shock waves.

S_1 = incident shock
S_2 = overtaking shock
S_3 = transmitted shock
a_1 = 1,130 ft. per sec.
p_1 = 747 mm. Hg
T_1 = 21.9°C.
C_{41} = 0.28 (R. W. Head)
W_{51} = 1.65 W_{21} = 1.69
W_{43} = 1.03 U_{21} = 0.90
P_{34} = 0.97

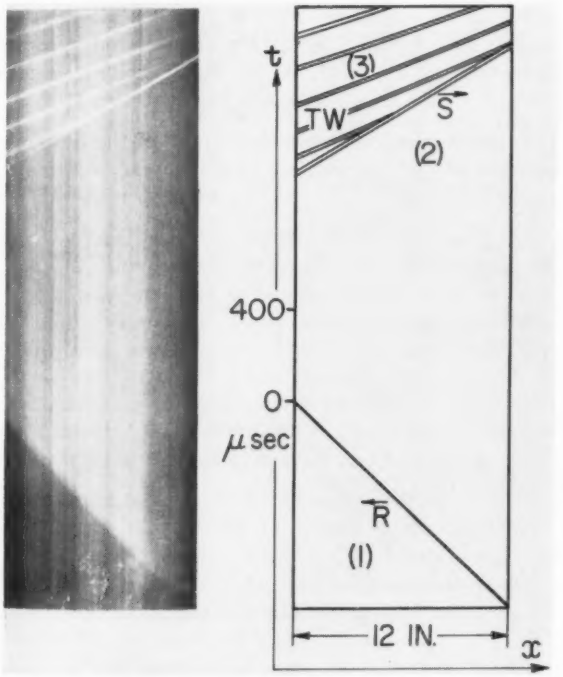

PLATE 10. Head-on collision of shock and rarefaction waves in air. TW = transverse shock waves, P_{51} = 1.96, P_{22} = 2.10, P_{21} = 0.590, p_1 = 746 mm. Hg, and a_1 = 1,135 ft. per sec.

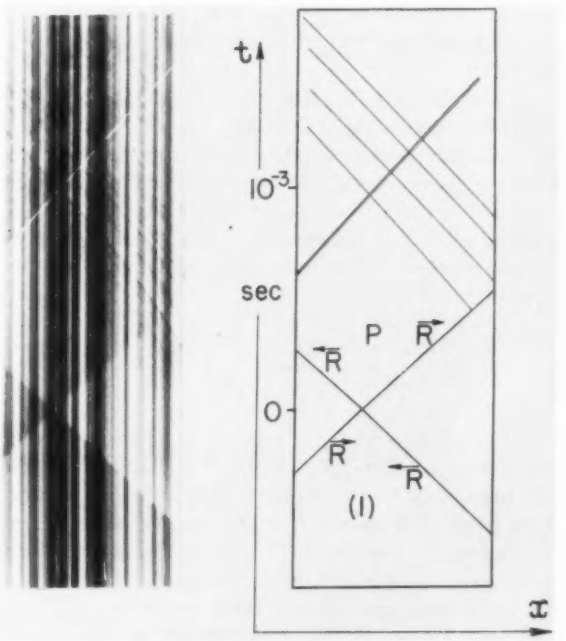

PLATE 12. Head-on collision of two equal rarefaction waves in air of strength 0.48. P = penetration region. p_1 = 3,164 mm. Hg.

initial conditions are given by state (1) and the strengths of the colliding shock and rarefaction waves. As a result of the interaction a receding shock and rarefaction wave are generated. The two waves are separated by a contact region of variable entropy that is due to the curving shock wave as it passes through the rarefaction wave. The shock-wave pressure ratio is amplified after the interaction. Across the resulting contact front $p_3 = p_4$ and $u_3 = u_4$. The solution is given by

$$P_{32} = 1 + \sqrt{1 + \alpha_1 P_{32}} \times \left\{ D - E\left[(P_{32}P_{15})^{1/(\alpha_1+1)} - (P_{12})^{1/(\alpha_1+1)} \right] \right\} \quad (59)$$

where

$$\left.\begin{aligned} D &= P_{12}{}^{1/(\alpha_1+1)} \frac{(P_{51}-1)}{\sqrt{1+\alpha_1 P_{51}}} + \sqrt{\alpha_1+1}\,[1 - P_{12}{}^{1/(\alpha_1+1)}] \\ E &= \sqrt{\alpha_1+1}\,\sqrt{P_{51}[(\alpha_1+P_{51})/(1+\alpha_1 P_{51})]} \end{aligned}\right\} \quad (60)$$

It should be noted that Eq. (59) gives a means of calculating the final uniform states and wave strengths after the collision, but it is not sufficient in itself to plot the path of the curving shock through the rarefaction wave. The procedure for tracing the shock path is outlined in reference 9. Eq. (59) may be employed to study the collision of a sound wave and a rarefaction wave. An actual (x, t)-plane schlieren photograph of a typical interaction is shown on Plate 10.

(*c*) *The Overtaking of Two Similarly Facing Shock Waves.*[10]—The above interaction is illustrated on Fig. 14. State (1) is given along with the strengths of the two overtaking shock waves. After the interaction there results a transmitted shock and a reflected rarefaction wave separated by a contact surface, for gases of $\gamma \leq 5/3$. For a fictitious gas in which $\gamma > 5/3$, a reflected shock wave is also possible. The solution for all real gases is given by

$$\sqrt{\frac{\beta_1(1+\alpha_1 P_{45})}{(\alpha_1+P_{45})(\alpha_1 P_{15}+1)P_{45}}}\left[(P_{34}-P_{14})\sqrt{\frac{(P_{15}+\alpha_1)P_{45}}{P_{14}+\alpha_1 P_{24}}} - (P_{45}-1)\sqrt{\frac{\alpha_1 P_{15}+1}{1+\alpha_1 P_{45}}} - (1-P_{15}) \right] + P_{34}{}^{\beta_1} - 1 = 0 \quad (61)$$

where

$$P_{34} = P_{14} \cdot P_{21} \quad (62)$$

A detailed discussion and a graphical analysis of this equation is given in reference 10. An actual (x, t)-plane schlieren photograph of this interaction is shown on Plate 11.

(*d*) *The Head-On Collision of Two Rarefaction Waves.*[11]—The interaction appears on Fig. 15, and the problem has been solved in a closed form for a monatomic and diatomic gas even in the region of penetration. There, the characteristic lines are no longer straight, and a general solution is obtained by using Riemann's integration method. The following results may be obtained (see Fig. 15):

$$U_{31} = (1/\gamma_1\beta_1)\,(P_{41}{}^{\beta_1} - P_{21}{}^{\beta_1}) \quad (63)$$

$$P_{31}{}^{\beta_1} = P_{41}{}^{\beta_1} + P_{21}{}^{\beta_1} - 1 \quad (64)$$

If the waves are of equal strength, then $P_{41} = P_{21}$ and $U_{31} = 0$. Similarly, $P_{31}{}^{\beta_1} = 2P_{41}{}^{\beta_1} - 1$ and is equivalent to Eq. (29) for the normal reflection of a rarefaction wave from a solid boundary. For this case it is shown in reference 11 that the last characteristic line to reach $x = 0$ is $x = a_1 t$ for a monatomic gas and $x = 2a_1 t$ for a diatomic gas. Under those conditions $P_{41}{}^{\beta_1} = 1/2$ and $P_{31} = 0$. Theoretically it is possible to achieve a complete vacuum in state (3) only after an infinitely long time.

The above condition, $P_{41}{}^{\beta_1} = 1/2$, is achieved in a shock tube for the case Air|Air when the diaphragm pressure ratio $P_{41} \approx 1{,}620$, or at an incident shock strength $P_{21} \approx 12.6$. (See Fig. 1 for notation.)

An (x, t)-plane schlieren photograph of the head-on collision of two rarefaction waves appears on Plate 12.

(*e*) *Expansion of the Uniform States Separated by the Contact Front in a Busemann Nozzle for High Mach Number Flows.*[12]—By expanding the flow behind the shock wave in a Busemann nozzle, as shown on Fig. 16, it is possible to attain high Mach Number flows in a shock tube which simulate flight conditions. It is also possible to expand the flow behind the contact front in a similar manner. A theoretical and experimental study of this problem is given in detail in reference 12.

It is interesting to note that the wave configuration after expansion is similar to the head-on collision of two shock waves. That is, two shock waves facing in opposite directions are formed, and they are separated by a contact front. In practice these waves are not plane, as shown on Plate 13. However, for a theoretical analysis this is a reasonable assumption, and the good agreement obtained between theory and experiment justifies the approach.

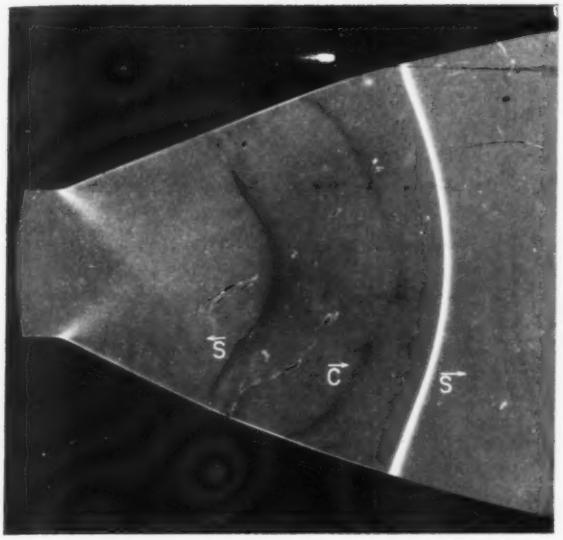

PLATE 13. The expansion of the uniform region behind the shock wave through a Busemann nozzle (see Fig. 16).

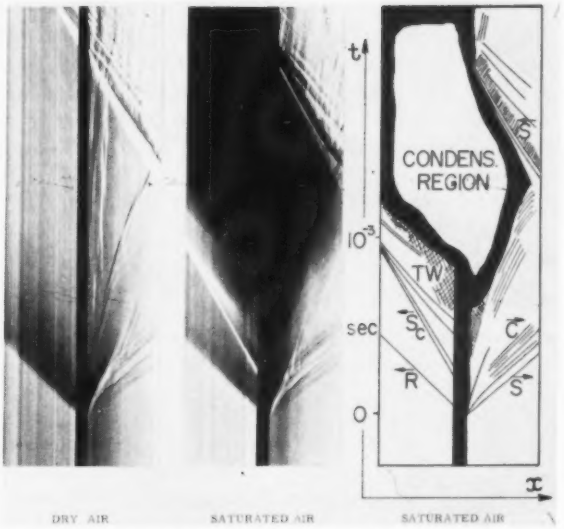

PLATE 15. Condensation effects in the rarefaction wave. $P_{41} = 10$, $P_{21} = 2.8$, $p_4 = 746$ mm. Hg, $T_{4,1} = 298°$K., $T_3 = 210°$K., $W_{11} = 1.61$, $M_3 = 1$, chamber length = 4 ft., and channel length = 1 ft. S_c = condensation shock.

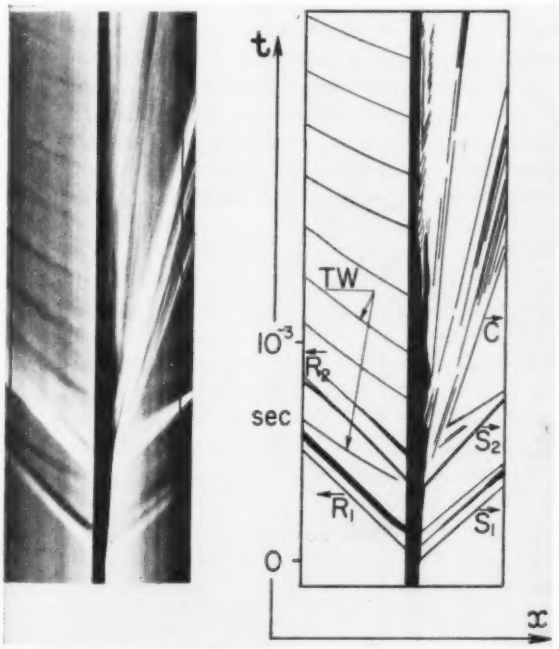

PLATE 14. The effects of nonsimultaneous rupture of two cellophane diaphragms. $p_4 = 1{,}008$ mm. Hg, $p_1 = 500$ mm. Hg, $P_{41} = 2.00$, $T_{4,1} = 21.3°$C.

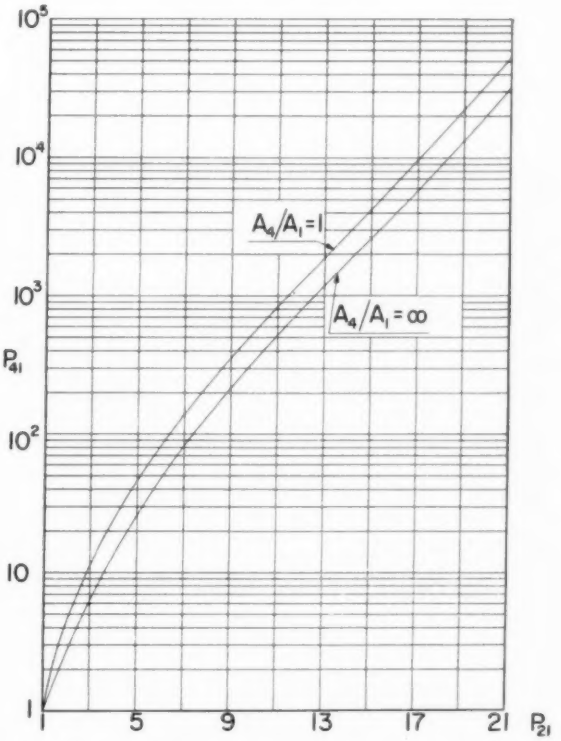

FIG. 18. Comparison of diaphragm pressure ratio (P_{41}) required to produce a shock pressure ratio (P_{21}) for a variable geometry shock tube ($A_4/A_1 = \infty$) and for a simple shock tube ($A_4/A_1 = 1$). Case: Air |Air.

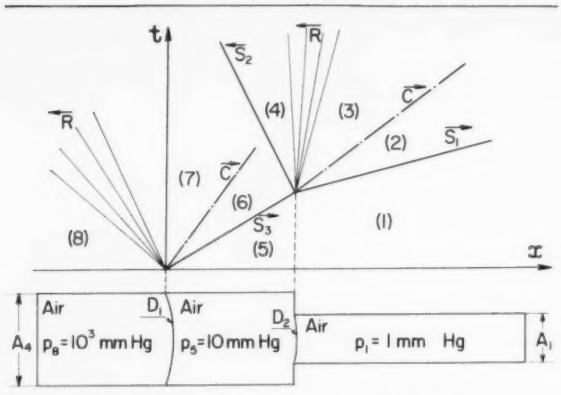

FIG. 19. The flow in a step-type shock tube.

This procedure combines one-dimensional nonstationary and two-dimensional stationary flows advantageously in order to produce a practical utilization of the shock tube as a type of high Mach Number flow intermittent wind tunnel.

(1.7) *Production of Strong Shock Waves*

The shock tube has recently been utilized for the study of the high-temperature states produced by strong incident and reflected shock waves. These states become ionized and lend themselves to investigations on magneto-hydrodynamics, relaxation phenomena, and other problems associated with atomic physics.

Strong shock waves may be produced in a practical manner by employing the following methods:

(a) The chamber is filled with a combustible mixture (say a stoichiometric mixture of oxygen and hydrogen diluted with 80 per cent helium) at high pressure, (400–1,000 lbs. per sq.in.) and is then ignited. Or the high pressure itself is raised until the metal diaphragm breaks and results in spontaneous ignition. The latter method appears preferable from the work conducted at Cornell Aeronautical Laboratories, Inc.[13] In this manner high diaphragm pressure ratios and extremely low energy ratios are produced as required by Eq. (1), in order to produce strong shocks.

(b) The gas in the chamber can be heated suddenly to a sizable temperature by passing a high voltage discharge directly through it. This process produces a high temperature and pressure in the chamber and yields extremely strong shock waves.

(c) Two reasonably strong shocks, which may be generated without undue difficulties, are made to overtake, and after the interaction produce an extremely strong transmitted shock wave [see Eq. (61)]. For example, from Fig. 1 of reference 10, it can be seen that, when two equal shocks of a pressure ratio of 100 overtake, they produce a shock wave of a pressure ratio of 4,200, which is about half the product of the pressure of the two incident shocks (this ratio approaches unity for weak shock waves) and represents an enormous increase in the transmitted shock strength.

(d) A worth-while improvement in generating strong shock waves is realized by using a variable geometry shock tube. Such a tube is shown on Fig. 17. It consists essentially of a large area chamber and a small area channel. The wave system produced when $M_3 > 1$ and $M_3 < 1$ is also sketched. The theory for this type of tube was first analyzed in reference 14 and is developed in reference 1. The greatest advantage occurs when $A_4/A_1 \to \infty$. A comparison of the shock

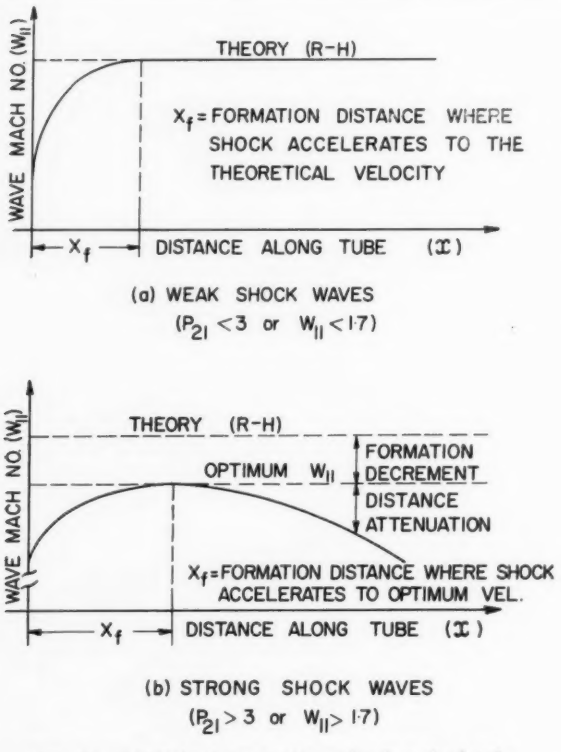
WAVE MACH NO. (W_II)
THEORY (R-H)
X_f = FORMATION DISTANCE WHERE SHOCK ACCELERATES TO THE THEORETICAL VELOCITY
X_f
DISTANCE ALONG TUBE (x)
(a) WEAK SHOCK WAVES
(P21 < 3 or W_II < 1·7)
WAVE MACH NO. (W_II)
THEORY (R-H)
OPTIMUM W_II
FORMATION DECREMENT
DISTANCE ATTENUATION
X_f = FORMATION DISTANCE WHERE SHOCK ACCELERATES TO OPTIMUM VEL.
X_f
DISTANCE ALONG TUBE (x)
(b) STRONG SHOCK WAVES
(P21 > 3 or W_II > 1·7)

FIG. 20. Total shock-wave attenuation in a shock tube.

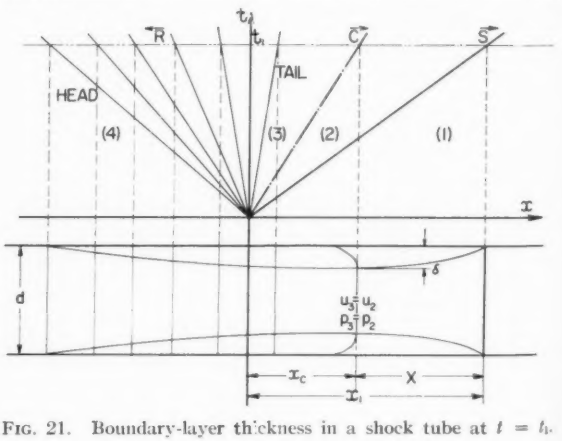

FIG. 21. Boundary-layer thickness in a shock tube at $t = t_1$.

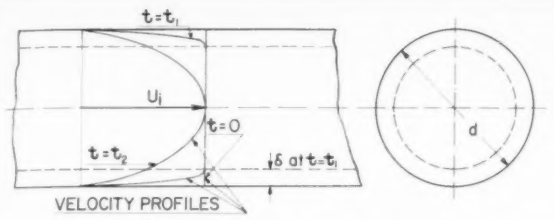

FIG. 22. Boundary-layer profiles with increasing time for the equivalent Rayleigh problem in a circular tube.

strength produced for a given P_{41} for $A_4/A_1 \to \infty$, and $A_4/A_1 \to 1$ (simple shock tube), is given on Fig. 18. A further increase in shock strength is obtained by combining a large chamber shock tube with several diaphragms in steps. A simple example appears on Fig. 19. It is assumed that, when A_4/A_1 is large, then the shock produced by breaking the first diaphragm, undergoes normal reflection at the second diaphragm, which is ruptured because of the sudden increase in pressure and temperature. This increase results in a $W_{11} = 3.9$, whereas without the first diaphragm $W_{11} = 3.3$.

Studies conducted on strong shocks[15] have already shown that a new field has been opened for the investigation of many problems in magneto-hydrodynamics and atomic physics.

PART (2) EXPERIMENTAL ASPECTS

(2.1) *Some Design and Construction Criteria for Shock Tubes*

The literature on shock tubes has become so extensive in the past 5 years that it would be a rather lengthy task to review all the applications of the shock tube and the resulting design and construction criteria. Instead, some general remarks will be made which are applicable to all shock tubes. A particular application, the 3- by 3-in. wave interaction tube, is discussed in some detail in reference 1, where the pertinent references are also listed.

The type of shock tube to be used is mainly determined by the funds available and the type of problem to be investigated. If shock waves, rarefaction waves, and contact surfaces are studied, then a simple cylindrical metal tube plus an optical system is quite adequate. If magneto-hydrodynamic effects produced by strong shock waves are investigated, a cylindrical metal chamber and a glass channel is sufficient. If flow studies over models are conducted in the uniform regions separated by the contact surface, it is necessary to use a square or rectangular metal tube that will accommodate observation windows for the optical systems and will readily permit the installation of aerodynamic models, piezo-gages, and hot-wire anemometers. The magnitude of the cross-sectional area will depend on the size of model to be tested or the Reynolds Number to be attained in the shock tube. The wall thickness of the tube will be determined by the maximum pressure in the chamber. Welded structures should be avoided because of the subsequent distortions. A combination of high pressure and large cross section will result in a heavy shock tube and may require hydraulic or other means for moving the various sections. It is convenient to have a chamber of 2 or 3 ft. and a channel composed of several sections of 2 to 8 ft. The channel sections should be interchangeable and easily aligned by means of dowel pins so that they may be used in combination as required by a particular experiment.

The viewing windows can be installed in one or two sections. These may be coupled with the remaining channel sections to give an observation window located at a desired distance from the diaphragm and will thus give a predetermined flow duration. The windows may be of standard plate glass for shadowgraph and schlieren observations. It is important that the windows be selected and installed in a manner that will give uniform refraction due to the slightly wedged surfaces that are always present in this type of glass. If the wedge surfaces in a window are not uniform and monotonic, the window should be replaced. For interferometric work the windows should be plane and parallel optical flats. The windows may be installed with Wood's metal, rubber gaskets, or recently developed plastic glass-to-metal bonding cement (for ex-

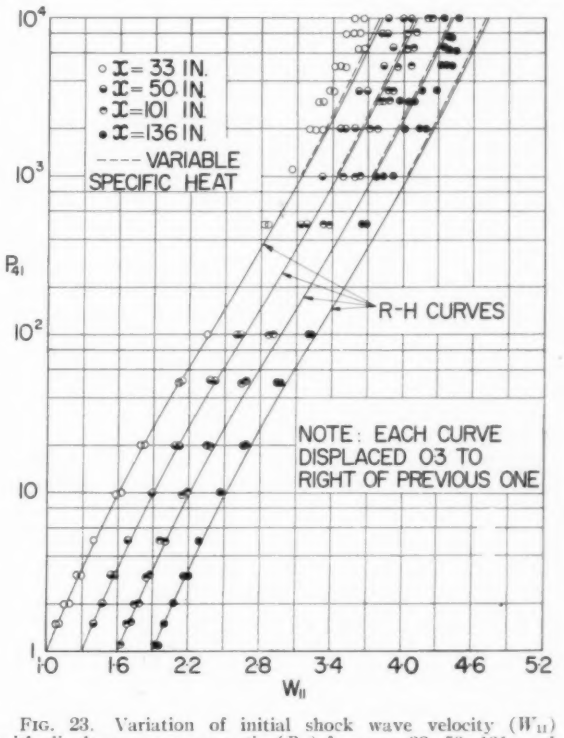

FIG. 23. Variation of initial shock wave velocity (W_{11}) with diaphragm pressure ratio (P_{41}) for x = 33, 50, 101, and 136 in.

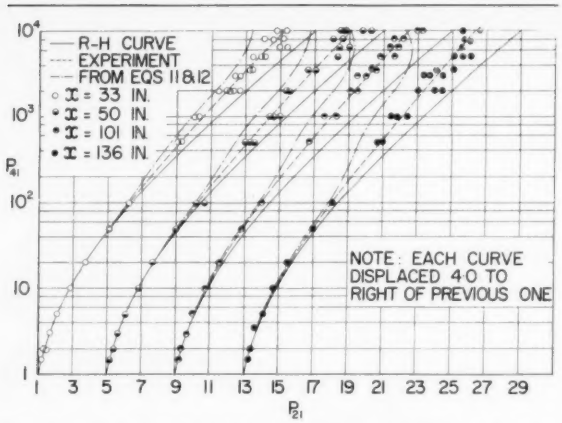

FIG. 24. Variation of the shock pressure ratio (P_{21}) with the diaphragm pressure ratio (P_{41}) and distance (x).

ample, Hysol cement) to give a flush and vacuum-tight installation.

The most satisfactory diaphragm materials are red-zip cellophane and cellulose acetate for low-pressure work and copper and aluminum sheets for high-pressure work. The red-zip cellophane has the best rupturing properties and leaves the smallest obstruction at the diaphragm cross section. Unfortunately, this material is not available in a range of thicknesses and must be used in several layers for higher pressure differences across the diaphragm. This gives rise to a small variation in the time it takes for all the diaphragms to rupture and results in an overlapping of several wave systems at the origin. (See Plate 14.)

The pressure differential at which a diaphragm will rupture depends on the material, cross-sectional shape, and area, as well as on the gasket material used to hold the diaphragm. If metal diaphragms are used, gaskets are not necessary, but the sharp edges of the channel section should be rounded to avoid cutting. If cellophane is used, rubber gaskets are bonded to the tube sections with (Pliobond or Armstrong) cement. The gaskets should have enlarged cross sections so that when the tube sections are fastened together, the gasket does not squeeze into the tube and cause a discontinuity at the origin.

Shadowgraph, schlieren, and interferometric methods have now become standard equipment for shock-tube investigations. The twin mirror, single pass, horizontal or vertical symmetrically offset schlieren system is most useful. First-surface paraboloidal mirrors corrected to a quarter wave length of aperture F6 to F10 are necessary for good schlieren resolution. The types of light sources, continuous or spark, are described in the references.

Initial conditions in a shock tube are obtained by measuring the pressure in the chamber by using mercury manometers or (Heise type) bourdon gages, and in the channel by using mercury or butyl phthalate manometers, McLeod, ionization and Pirani gages or (Wallace and Tiernan) absolute pressure gages. The temperature of the gases in the chamber and channel is generally room temperature. When gas at high pressure is admitted into the chamber, it should be allowed to reach thermal equilibrium (in about a minute) before the diaphragm is ruptured. Commercial cylinders of compressed gas (air, A, He, CO_2, H_2, N_2, or O_2) are easily available, and they have the advantage of a low dew point (about minus 40°C. or lower) which eliminates extraneous effects due to water condensation.

Final conditions in the shock tube are obtained by measuring the shock wave velocity (W_{11}) continuously[1] or by measuring the time interval for the shock wave to travel over a given base (accurately measured distance between two points). By utilizing the theoretical relations of Part (1) the flow parameters can be calculated. In addition, pressure profiles can be measured directly by using piezo-electric transducers, temperature profiles may be recorded with hot-wire anemometers, density contours are determined with an interferometer, and flow Mach Numbers are found from shock angles over conical or wedge models. When strong shock waves ($W_{11} \gtrsim 10$) are studied, the wave front itself becomes luminescent, and its velocity may be self-recorded on a drum camera without the use of a shadowgraph or schlieren system.

To date, the wave speed results, along with density and Mach Number measurements, have been the chief source for verifying the shock-tube theory. Piezo-gage data and anemometry data have been confined, so far, to weak shock waves. Light-scattering techniques have also been employed to give a measure of the degree of liquefaction in the cold region (3) behind the contact surface.

(2.2) *Experimental Procedure*

The following data are based mainly on the wave-speed measurements of the (x, t)-plane schlieren records obtained with a rotating drum camera in conjunction with the 3- by 3-in. wave interaction tube. The drum rotates at about 4,200 r.p.m. and carries a strip of 70-mm. Linagraph Pan film externally. The schlieren system is equipped with 12-in. parabolic mirrors. The arrangement makes it possible to obtain continuous (x, t)-plane records over 12 in. and about 14 millisec.

The photographic records show the propagation of discontinuities in the density derivative and, as a result, reproduce the paths of the basic flow elements found in nonstationary flows—that is, shock waves, contact surfaces, rarefaction waves, vortices, eddies, and boundary-layer effects.

The film speed is determined accurately to about 0.07 per cent. Wave angles are measured to better than 0.5 min. by means of a Hilger projector. As a result, wave velocities can be found to better than 2 per cent, even at diaphragm pressure ratios of 10,000. To produce diaphragm pressure ratios of this order it

is necessary to employ channel pressures of 0.4 mm. Hg and experimental errors of about 9 per cent are possible. By taking several runs at high pressure ratios and utilizing average results, it is possible to minimize this effect.

(2.3) *The Wave System at the Origin in a Real Shock Tube*

Plate 1 is typical of the schlieren photographs taken at the origin which are presented and analyzed in reference 1. Under pressure the cellophane diaphragm becomes a curved surface. When it ruptures, three-dimensional effects are introduced in the form of shock-wave reflection arising from shock curvature. Shock diffraction and vortices are also produced by the jagged remains of the diaphragm. As a result the assumption of one-dimensional inviscid flow at the origin is not realized.

All the records are typical, in that the shock wave at the origin appears to be formed within a network of converging characteristic lines representative of a compression wave. However, closer examination of the optical records reveals that the method of characteristics cannot be applied in order to predict the birth point of the shock wave[1] because the apparent compression wave is in fact composed of a number of coalescing shock fronts. These overtake, accelerate, and combine to form the primary shock wave. The wave is initially curved, but the resulting regular and Mach reflections form the mechanism that produces a plane primary shock wave. The reflections also give rise to a train of transverse waves that follow the primary shock wave down the tube (even as far as 50 tube cross-sectional widths). They also propagate upstream of the diaphragm. Eventually the transverse waves become sound waves. However, they act as a dissipative mechanism and contribute to the total shock-wave attenuation and to the fluctuation of physical quantities in the two uniform regions separated by the contact front.

It is shown in reference 1 that even for a weak shock wave ($P_{21} < 3$) accelerations of the order of 7×10^7 ft./sec.^{2} may be produced during the first 10 μ sec., and in this respect the rupturing process approximates the ideal case of infinite acceleration.

Plate 1 also shows that the contact front is in fact a region which in a matter of 18 in. has grown to an apparent thickness of 3 in.

The region behind the contact front and the rarefaction wave is filled with striations that are indicative of turbulent and eddying flow. The rough flow is caused by the passage of the gas from the chamber over the jagged remains of the diaphragm.

Since the ideal case of an instantaneously plane shock wave is not attained at the origin, the rarefaction wave is not of the centered type. The head of the wave appears prominently on Plate 1 but not the tail of the wave. The nonappearance of this characteristic line cannot be attributed to the fact that the rarefaction wave is not centered, since this does not affect the order of magnitude of the value of the discontinuity in the density derivative which responds to a schlieren system.

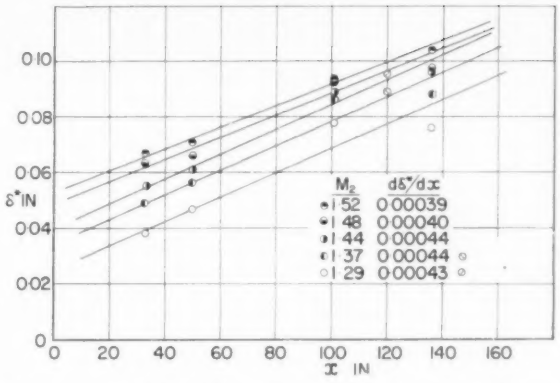

FIG. 25. Variation of boundary-layer displacement thickness (δ^*) with M_2 and distance (x) from the diaphragm.

Summing up then, it may be stated that the flow in a real shock tube is a viscous process and deviations from an inviscid flow solution may be expected.

(2.4) *Some Experimental and Theoretical Aspects of Shock-Wave Attenuation*

One of the first quantities to be determined by shock-tube investigators was the shock-wave velocity, since it was relative easy to measure. It is shown in Part (1) that a knowledge of the initial conditions and the shock-wave velocity makes it possible to calculate all the physical quantities of the flow in a shock tube. This approach was followed by many experimentalists, and they found that the agreement between theory and experiment was good for weak waves but became progressively worse for strong shock waves.

This deviation has been referred to somewhat loosely as shock-wave "attenuation." As a result of the present set of experiments it is possible to define the term "attenuation" in a more rigorous manner. It has been found that associated with each weak or strong shock wave there is a characteristic length (x_f) over which the shock forms, accelerates, and achieves a maximum velocity.[1] Based on the present results a weak shock is defined as one for which $P_{21} < 3$. The formation distance (x_f) was found to be somewhat longer for strong shocks.

For weak shock waves the achieved maximum velocity (W_{11}) is the one predicted theoretically for a given diaphragm pressure ratio (P_{41}). Confirmation of this point appears on Fig. 23, and it may be noted that the wave speed did not change measurably over the 142-in. length investigated during the present experiments.

For strong shock waves ($P_{21} > 3$), it is noticed that the shock wave achieves a maximum speed at the end of its formation distance (x_f), which is lower than the theoretical wave speed corresponding to the given

diaphragm pressure ratio. Beyond the formation length a deceleration occurs, and the shock velocity decreases monotonically with distance as sketched in Fig. 20b. It should be noted that during the present experiments, strong shock waves were produced by evacuating the channel to pressures as low as 0.4 mm. Hg; a procedure which resulted in correspondingly high kinematic viscosities (ν_2) behind the shock wave.

Recapitulating, it may be concluded that for strong shock waves the overall defect or total attenuation in shock speed consists of two portions: (a) a decrement due to formation and (b) a further attenuation due to the distance traversed by the shock wave. These will be referred to as a formation decrement and distance attenuation, respectively.

It is reasonable to assume in the case of strong shock waves (especially where the kinematic viscosity is high) that the formation decrement is due to viscous action produced during the shock formation process and the distance attenuation results from a boundary-layer build-up. The possible growth of the boundary layer in a shock tube is illustrated on Fig. 21. It is seen that at the position of the shock wave the boundary layer has zero thickness, since the gas particles in the tube have not been affected yet. At the contact front the boundary-layer thickness (δ) is a maximum, since there the particles have been in motion with respect to the wall for the total length of time (t_1) under consideration. Just behind the contact front the Reynolds Number increases discontinuously, and for an ideal flow without turbulence in region (3) it may safely assumed that the boundary-layer thickness will decrease in state (3) and through the rarefaction wave until it is zero again at the head of the wave.

Thus the boundary layer in a shock tube at a given time (t) is a function of position (x). The thickening of the boundary layer with time will diminish the induced mass flow behind the shock wave, and as a result its speed will be reduced to balance the lower mass flow. No definite mechanism for reducing the shock speed is postulated. However, since shock decay is caused by a rarefaction wave, it is generally considered that the contact front slows up. The deceleration produces a rarefaction wave analogous to the classical one-dimensional motion of a piston in a cylinder.[1] It will be shown subsequently that the very opposite happens in a real flow—that is, the contact front actually speeds up. For this reason, the above concept may appear rather artificial. Nevertheless, even if the mechanism for slowing up the shock wave is not known, it is reasonable to state that the boundary-layer growth reduces the mass flow, which in turn decreases the shock speed and is the cause of the distance attenuation.

The present problem may be compared with Rayleigh's analysis of an infinite flat plate that has been started instantaneously from rest to a uniform velocity u_t at $t = 0$.[16] In the present analysis the equivalent problem is considered—that is, the plate is at rest and a flow is generated instantaneously such that its speed is zero at $t = 0$, $u = u_t$ for $t \geq 0$. This is illustrated for a cylindrical shock tube in Fig. 22 and was solved in reference 17. It is seen that at small times the boundary layer is thin and uniform over the infinite tube. For large times the boundary layer approaches the center of the tube, and the motion becomes a pipe flow. In a real shock tube the boundary layer does not grow uniformly, and it occupies only a finite length of the tube. Furthermore, the end boundary conditions are complex because of the presence of the shock wave and the contact region, which extends right to the diaphragm station due to the no-slip condition at the wall. However, it will be shown subsequently that some useful results may be obtained by considering the two problems as equivalent.

A dimensional analysis of the instantaneously started smooth tube (otherwise a roughness parameter must be included) indicates that the boundary-layer thickness (δ) or displacement thickness (δ^*) (see Fig. 21), neglecting heat transfer, is a function of the following quantities (for a real flow the tube walls are cold and heat transfer exists between the gas and the walls, and the Prandtl Number is an important parameter):

$$\delta = \delta(p, \rho, \mu, \gamma, u, d, t) \tag{1}$$

$$F(\delta, p, \rho, \mu, \gamma, u, d, t) = 0 \tag{2}$$

Therefore, there are five dimensionless π-functions, such that Eq. (2) may be expressed in terms of the following dimensionless parameters as:[18]

$$f\left(\frac{\delta}{d}, \frac{u^2}{\gamma p/\rho}, \frac{\rho u d}{\mu}, \frac{\nu t}{d^2}, \gamma\right) = 0 \tag{3}$$

$$\delta/d = g[M, Re, (\nu t/d^2), \gamma] \tag{4}$$

Therefore, if tube roughness and heat transfer are neglected, then for a given gas (γ) the distance attenuation that depends on the boundary layer may be expected to vary with the Mach Number (M), the Reynolds Number (Re), and the time parameter ($\nu t/d^2$).

In the case of the shock tube the gas particles at the contact front are in motion with respect to the wall for the greatest length of time, and it is the time that apparently would correspond to the time considered in the equivalent Rayleigh problem. If the total shock wave attenuation is neglected, this time (t_1) is computed as (Fig. 21),

$$t_1 = \frac{x_C}{u_2} = \frac{x_1}{w_1} = \frac{X}{w_1 - u_2} \tag{5}$$

since they are all identical. It is convenient to measure t_1 in terms of the shock position from the diaphragm ($t_1 = x_1/w_1$), and the time parameter may be expressed as

$$\nu_2 t/d^2 \equiv \nu_2 x/Aw \tag{6}$$

where A is the cross-sectional area proportional to d^2.

The above type of analysis cannot be applied directly to the formation decrement, since it would also depend on the diaphragm rupturing process, which is a complex three-dimensional viscous problem.

In order to check some of the factors contributing to the formation decrement and the distance attenuation, the following experiments were conducted: To investigate the formation decrement, different types and combinations of cellophane diaphragms were employed. The diaphragms were maintained at a constant pressure difference $\Delta p = (p_4 - p_1)$, of 100, 500, and 1,000 mm. Hg over a wide range of diaphragm pressure ratios (P_{41}) in order to study influence of static loading.

The chamber pressure (p_4) was limited to about 7 atm. It was not possible, therefore, to maintain a constant channel pressure (p_1) over a large P_{41} range. Instead p_1 was varied to obtain a wide range of P_{41}.

The influence of extraneous disturbances on the formation decrement produced by the shredded diaphragm or the diaphragm breaker plunger were also observed. The broken diaphragm introduces a discontinuity at the origin. This effect was emphasized by placing protruding metal frames at the diaphragm station and noting the differences produced in the formation decrement. By placing the diaphragm breakers upstream or downstream of the diaphragm under identical conditions, similar effects could be investigated.

Finally, to study the distance attenuation, the shock velocities were measured with a wave speed camera and schlieren system continuously over a 12-in. length at distance intervals starting at the origin and beyond, up to 142 in. (0- to 50-tube width) from the diaphragm station. The range of diaphragm pressure ratio (P_{41}) was simultaneously varied over the range $1 < P_{41} \leq 10{,}000$. (On the graphs that follow x is the distance from the diaphragm station to the center of the 12-in. schlieren beam.)

The experimental results may be summarized as follows: Cellophane diaphragms, CIL MSTL 600, used singly or in combination, gave the closest approximation to an ideal rupture when they were loaded to about half or greater of their static rupturing load. The energy contributions from the breaking cellophane diaphragms may be neglected. Introducing discontinuities at the origin or small protrusions has no measurable effect on the shock-wave velocity. The formation distance where the shock becomes plane and achieves a straight path on the (x, t)-plane varies. For weak waves ($P_{21} < 3$) about 4-tube widths are required. For strong shocks where $P_{21} \gtrsim 17$, the formation distance extends over about 8-tube widths.

The effects of distance attenuation and the formation decrement for $1 < P_{41} \leq 10{,}000$ and 33 in. $\leq x \leq 142$ in. are summarized on Fig. 23.

The theoretical relations [Eqs. (1) and (7), Part (1)] may be approximated by the equation,

$$\log P_{41} = 1.34\,(W_{11} - 1) + 0.176 \tag{7}$$

Whereas, all the present experimental results are described quite well by the expression

$$\log P_{41} = 1.33x^{0.03}\,(W_{11} - 1) + 0.08 \tag{8}$$

It was desirable to have a relation that would be applicable to all shock tubes. As a possible solution the viscous incompressible equations of motion were solved for a square tube having the following initial and boundary conditions:

$$\left.\begin{aligned} \partial u/\partial t &= \nu[(\partial^2 u/\partial z^2) + (\partial^2 u/\partial y^2)] \\ u(z, y, 0) &= u_i \text{ for } \begin{cases} 0 < z < z_0 \\ 0 < y < y_0 \end{cases} \\ \left.\begin{matrix} u(0, y, t) \\ u(z, 0, t) \\ u(z_0, y, t) \\ u(z, y_0, t) \end{matrix}\right\} &= 0 \text{ for } t > 0 \end{aligned}\right\} \tag{9}$$

The solutions for the velocity distribution and the mass flow are given by the following:

$$\frac{u}{u_i} = \sum_{a=1}^{\infty}\sum_{b=1}^{\infty} \frac{4}{ab\pi^2}\,(1 - \cos a\pi)\,(1 - \cos b\pi)e^{(-\nu t/A)\,(a^2 + b^2)\pi^2} \cdot \sin\frac{a\pi z}{z_0} \cdot \sin\frac{b\pi y}{y_0} \tag{10}$$

$$\frac{m}{m_i} = \frac{4}{\pi^4}\sum_{a=1}^{\infty}\sum_{b=1}^{\infty} \frac{(1 - \cos a\pi)^2\,(1 - \cos b\pi)^2}{a^2b^2} \cdot e^{(-\nu t/A)\,(a^2 + b^2)\pi^2} \tag{11}$$

If the shock attenuation is due to a defect in the mass flow, then this may be expressed for air as

$$\frac{m}{m_i} = \left(\frac{P_{21} - 1}{P_{21} + 6}\right)\sqrt{\frac{6P_{21} + 1}{6(P_{21})_i + 1}}\left(\frac{(P_{21})_i + 6}{(P_{21})_i - 1}\right) \tag{12}$$

By assuming that both problems were equivalent [i.e., Eqs. (11) and (12)], it was possible to plot Fig. 24. The results indicate that the viscous flow analysis gives a good description of the real flow up to diaphragm pressure ratios of 200. Beyond 200 the attenuation predicted by the present analysis is too large. This confirms the previous statement that, when the time parameter $(\nu t/A)$ is large, the viscous effects may be expected to be too great, since the flow becomes a nonstationary pipe flow analogous to the Poiseuille flow for the stationary case.

A more realistic approach is to assume that the flow consists of an inviscid core and a viscous boundary layer.

The boundary-layer thickness varies with x at a given t, between the shock and the contact front. But it is assumed that the boundary-layer displacement thickness (δ^*), at the contact front, controls the defect in mass flow which in turn causes the shock-wave attenuation. The mass flow ratio depends on the initial and final strengths of the shock wave and is found from Eq. (12).

The mass defect at the contact front,

$$\Delta m = \rho_2 u_2 \delta^* D$$

where D = perimeter of the shock tube and ρ_2, u_2, and δ^* are measured at the contact front. For a square tube then,

$$\delta^* = (y_0/4)\,[1 - (m/m_i)] \tag{13}$$

The above definition of δ^* may be questioned. However, it can be tested experimentally, perhaps by interferometric means. Some work in this direction is presently under way at the Institute of Aerophysics.

By utilizing the results of Fig. 24 in conjunction with Eqs. (12) and (13), it is possible to plot a family of curves of δ^* vs. x for varying shock strengths or flow Mach Numbers as shown on Fig. 25. During the present experiments the ratio ν_2/Aw_1 was held constant for a given M_2 and x. The results of the above figure indicate that

$$d\delta^*/dx \backsimeq 0.0004$$

over the Mach Number range $1.3 < M_2 < 1.5$. The equivalent value for stationary flow is about tenfold. When the lines are extended toward the origin, it may be seen that δ^* is composed of a sizable formation decrement that increases with M_2 or ν_2 and a distance attenuation that exhibits an almost constant increase. The value of $\delta^* \backsimeq 0.1$ in. at the 150-in. station for $M_2 = 1.5$ is a reasonable figure. The viscous flow result of $\delta^* \backsimeq 0.3$ in. appears too large. A direct check of the above analysis by measuring δ^* at the contact front would verify the usefulness of the present approach to the problem.

It should be emphasized that at the present time there is no theoretical or empirical analysis that would account for, or unify, the various wave attenuation results obtained by different investigators.

For low diaphragm pressure ratios it is possible to discern the rear and front boundaries of the contact region, as shown on Plate 1. As the diaphragm pressure ratio increases, the rear boundary merges with the rough flow of state (3) and, finally, at low channel pressures even the front boundary is difficult to distinguish. (For channel pressures below 0.3 mm. Hg the shock wave itself becomes indistinguishable.) Typical results for the speed of the front of the contact region (U_{21}) as a function of P_{41} and x are plotted on Figs. 26 and 27. Briefly, the behavior of the contact front is opposite to that of the shock front (see Fig. 28). For weak and strong contact fronts there is a deceleration of the initial jet of gas following the rupture of the diaphragm.[1] At the end of the formation distance an optimum velocity is reached. For weak contact fronts, the optimum velocity is the one predicted by Eq. (8) [Part (1)], and appears to be independent of distance (x). For strong contact fronts the velocity at the end of the formation distance is greater than the theoretical value, and the velocity further increases with the distance traversed by the contact front.

To summarize, beyond the formation distance strong shock waves decelerate, whereas strong contact fronts accelerate concurrently. The increase in contact front velocity cannot be explained on the basis of the heat conduction solution for a "laminar" contact region.[3] It is not known what effect this speed-up has on the flow quantities in the shock tube.

In a real flow the boundary-layer growth is a function of position and time. The continuity equation indicates that the gas properties and the effective tube area will also be a function of the above independent variables, and what influence this has on the contact front velocity is not known.

Nevertheless, any new approach to a unifying solution of shock-wave attenuation must consider the contact front acceleration simultaneously if it is to describe the real physical processes. An experimental determination of the flow quantities between the shock wave and the rarefaction wave appears as a necessary step to aid in the formulation of a realistic mathematical model.

(2.5) *Real Flows in the Two Uniform States Separated by the Contact Region*

Since shock-wave attenuation, contact front acceleration, transverse waves, and eddying occurs in a real flow, it may be expected that deviations will occur from an inviscid analysis. So far, a systematic investigation of the two uniform states by measuring density, temperature, pressure (and particle velocity) over a wide range of shock Mach Numbers has not been done.

Most of the available data on the measurement of physical quantities deal with flows induced by extremely weak shock waves. This includes pressure, temperature, and density profiles of the entire flow.

For strong shock waves the data consist almost entirely of Mach Number measurements determined from cone- or wedge-type models. The results are not useful for predicting the actual values of the flow quantities or the flow uniformity. (Some piezo pressure profiles in reference 3 show that deviations of about 30 per cent are not uncommon for diaphragm pressure ratios of about 1,000.) Typical wedge measurements of the Mach Numbers M_2 and M_3 as a function of P_{41} (from reference 19) are shown on Figs. 29 and 30. It is seen that the experimental results for M_2 agree quite well with the theory up to $M_2 \backsimeq 1$. For $M_2 > 1$ the Mach Number starts to decrease and is indicative of the effects of stronger shock waves. In region (3) the Mach

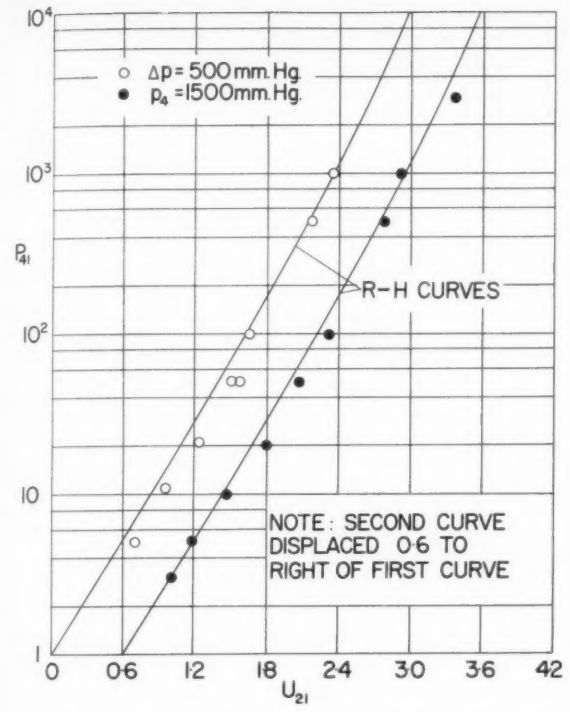

FIG. 26. Velocity of the front of contact region (U_{21}) as a function of diaphragm pressure ratio (P_{41}).

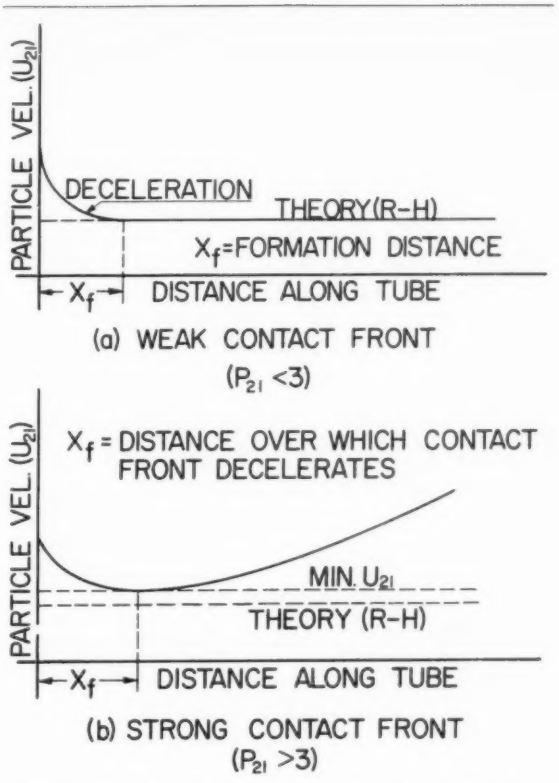

FIG. 28. The behavior of the contact front in a shock tube.

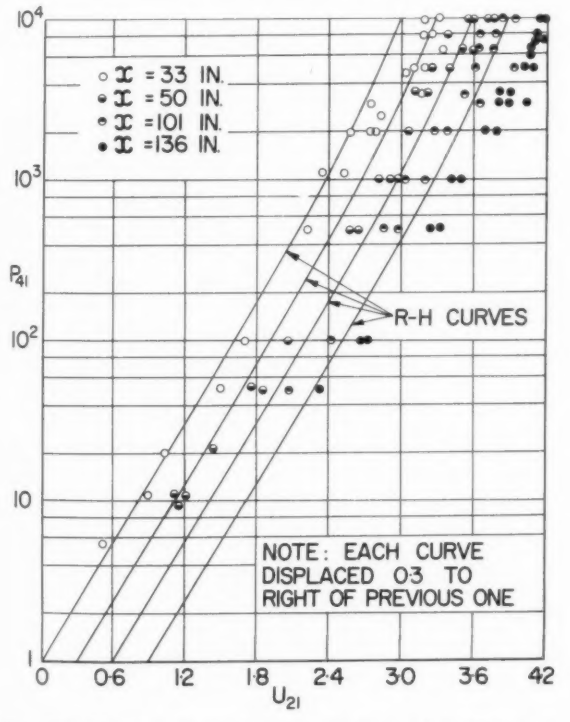

FIG. 27. Velocity of the front of contact region (U_{21}) as a function of diaphragm pressure ratio (P_{41}) and distance (x).

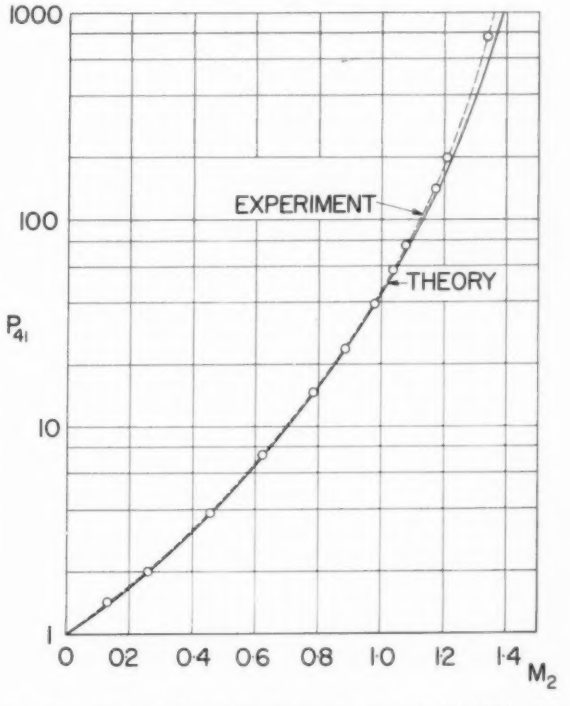

FIG. 29. The variation of Mach Number in state (2) (M_2) with diaphragm pressure ratio (P_{41}). Case: Air | Air.

Number appears to approach a limit of about $M_3 \backsimeq 4.5$ for diaphragm pressure ratios $(P_{41}) > 10{,}000$. This may be due to the fact that the predicted low temperatures in state (3) are not achieved in practice. The real reasons may become evident as soon as direct measurements of the flow quantities become available.

A check on the temperature would have been possible if the tail of the rarefaction wave had appeared on the (x, t)-schlieren records. Unfortunately, this characteristic line does not appear in a schlieren record of the rarefaction wave produced by the ruptured diaphragm. However, it was possible to utilize the head of the rarefaction wave (Plate 1) in order to determine the speed of sound from a gas dynamic point of view. The values of the sound speed at 0°C. for air = 1,087 ± 2 ft. per sec., argon = 1,009 ± 1 ft. per sec., and carbon dioxide = 844 ± 1 ft. per sec. are in good agreement with acoustic results.[20] This also bears out the previous observation that for weak shocks, starting with a sound wave, the wave speeds are in excellent agreement with theory.

It is of interest to point out that condensation effects may readily be observed in the rarefaction wave region. Plate 15 is typical of the flow at the origin for wet and dry air. The condensation shock path is straight, and its velocity is uniform at about 630 ft. per sec. relative to the tube. Theoretically, the path should be curved. The droplet precipitation as a function of time is strikingly demonstrated and suggests the possible study of the rate of nuclei formation from this type of record by using a photodensitometer.

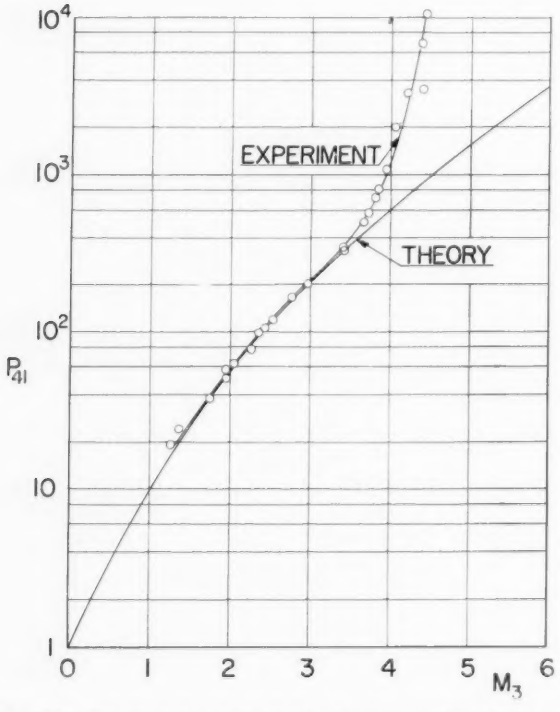

FIG. 30. The Variation of Mach Number in state (3) (M_3) with diaphragm pressure ratio (P_{41}). Case: Air|Air.

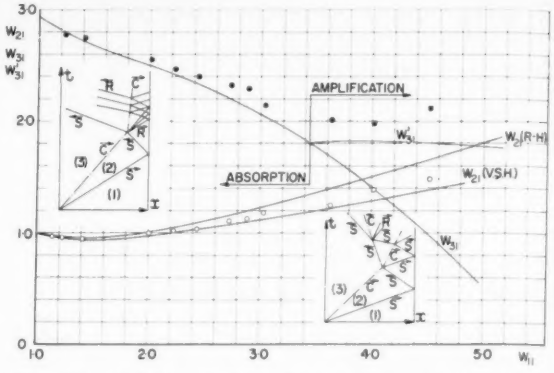

FIG. 31. Variation of the reflected wave speed (W_{21}), the refracted wave speed (W_{31}), and the shock-amplified wave speed (W'_{31}), with the incident wave speed (W_{11}). Case: HE|Air.

(2.6) *Real Flows in the Vicinity of an Open or Closed Chamber or Channel*

Plate 2 illustrated the normal shock reflection at the closed end of a channel for Air|Air and Plate 4 for He|Air. It is seen that shock wave refraction at a contact surface may also be studied from such records. Typical results from reference 21 are shown on Fig. 31. The graphs indicate that the normal reflected shock speed approaches the variable specific heat results for shock Mach Numbers $W_{21} > 3$. For incident wave Mach Numbers $W_{11} \backsimeq 5$, at channel pressures (p_1) of a few mm. Hg, luminescence produced by ionization may already be observed in state (5).

Few direct measurements of the physical quantities in state (5) are available. This region will probably be utilized extensively for the study of atomic physics and magneto-hydrodynamics. The actual refracted wave speeds (W_{31}) deviate considerably from the theoretical curve. The deviation is similar to that for M_3 for the same region (Fig. 30) and indicates that the low temperatures may not be achieved in state (3).

It is worth noting that in region (2), (Plate 2), which has the lower Reynolds Number, the shock wave does not appear to undergo too much of a change, whereas in region (3) the shock appears as broken up into multiple shock waves. The flow is typical of the interaction of a shock and a jet and is analogous to a flow with a thick boundary layer in stationary, supersonic pipe flow. Since state (3) has a rough and eddying type of flow, it produces a similar result. An additional effect due to the boundary layer, which is more pronounced in state (3) than in (2), is indicated by the refracted shock wave racing ahead inside the boundary layer.

The normal reflection of a rarefaction wave at a closed channel is shown on Plate 3. Limited information can be obtained from an (x, t)-plane schlieren record, since only the head of the waves appears. The uniform region (6) has been neglected by experimentalists to

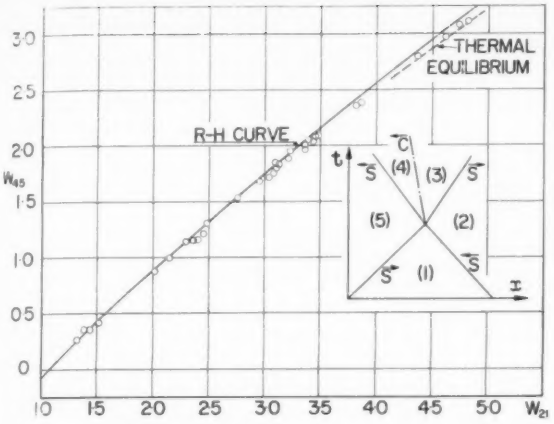

FIG. 32. Variation of the transmitted wave speed (W_{45}) with the incident wave speed (W_{21}) for the head-on collision of two shock waves in air. $W_{51} = 2.18$.

date, and yet it offers excellent possibilities for research in a low-temperature state.

When the channel is open the shock wave emerges into the free atmosphere where it diffracts and approaches a spherical wave. It is followed by an annular vortex. A rarefaction wave followed by a shock wave are also propagated back into the chamber. Large viscous effects are indicated on Plate 16. A theoretical analysis that predicts the existing wave configuration and the wave motion at the open channel is presently not available.

Plate 17 shows the emergence of a rarefaction wave into the free atmosphere. A compression wave does not appear to be reflected back into the chamber as predicted from a perfect flow analysis.[22] About 500 μ sec. after the rarefaction has emerged from the chamber, an almost stationary vortex is formed within the tube by the inflow from the open end. (The vortices from the ruptured diaphragm soon merge with this vortex.) The flow appears to be rough, judging from the large number of striations, and is typical of unfaired subsonic entries. An adequate theory to cover this type of flow has not been developed.

(2.7) *Experiments on One-Dimensional Wave Interactions*

The pertinent equations dealing with wave refraction and collisions were discussed in Part (1). The present section will supply some basic experimental data on the interactions.

Fig. 32 shows a typical result for the head-on collision of two shock waves. It is seen that the wave speeds tend toward the variable specific heat values (lower wave speed) as in the normal shock reflection case (Fig. 31), which is the symmetric case of two equal colliding shocks.

A typical experimental result[9] for the head-on collision of a shock and a rarefaction wave appears on Fig. 33. It is seen that the agreement between theory and experiment is quite good.

The case of shock refraction at an Air||A contact surface formed by a nitrate dope film of several thousand angstrom units is shown on Fig. 34 taken from reference 23.

On Fig. 31 it may be noted that the primary shock wave undergoes normal reflection at the end of the tube and subsequently refracts at the Air||He contact front that was produced at the origin. This problem is considered in detail in reference 21. It may be stated that the results for stationary contact fronts are in good agreement with the theory even for double refraction.

The theory for the refraction of a rarefaction wave, which was outlined in Part (1), is presently being tested experimentally at the University of Toronto, Institute of Aerophysics.

Plates 18 and 19 illustrate the interaction of a shock wave with a No. 40 and No. 30 mesh screen. After the interaction the wave system consists of a reflected and transmitted shock wave separated by a contact front and a vortex. The vortex is on the downstream side of the screens and appears on the records for higher wave Mach Numbers when the particle velocity is sizable enough to move the vortex downstream as on Plate 18. It has been tentatively established that the Mach Number M_5 remains quite constant for a given mesh size (see Plate 18 for notation).

The schlieren photographs show that region (3) is at a lower density than region (2). Since the pressures

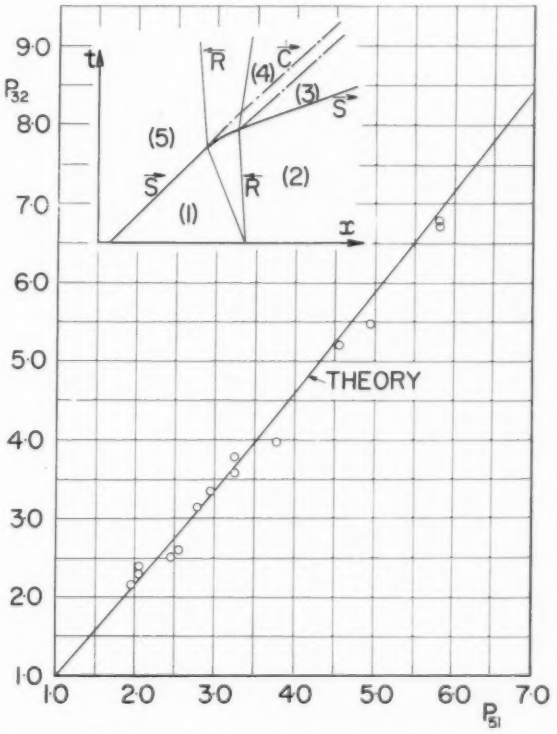

FIG. 33. Head-on collision of shock and rarefaction waves. Rarefaction strength $P_{21} = 0.500$.

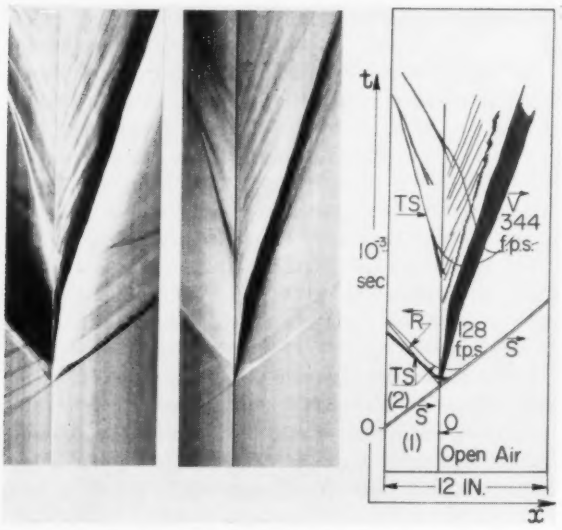

PLATE 16. Emergence of a shock wave from the open end of a 3- by 3-in. channel.

V = vortex ring	$P_{41} = 3.0$	$a_1 = 1,142$ ft. per sec.
O = open end of channel	$W_{11} = 1.28$	
$p_1 = 748$ mm. Hg	$U_{21} = 0.40$	TS = transverse shocks

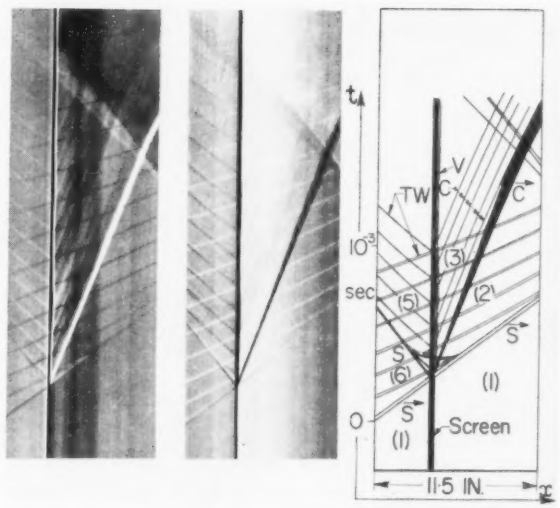

PLATE 18. The interaction of a shock wave with a No. 40 mesh screen.

V = vortex	$P_{21} = 4.00$	$W_{56} = 1.15$	$p_2 = p_3 = 1,280$ mm. Hg	
TW = transverse shocks	$W_{61} = 1.34$	$M_5 = 0.42$	$p_6 = 1,400$ mm. Hg	
a_1 = 1,137 ft. per sec.	$W_{21} = 1.26$	$M_2 = 0.33$	$p_5 = 1,935$ mm. Hg	
p_1 = 747 mm. Hg	$U_{21} = 0.36$	$M_5 = 0.18$		

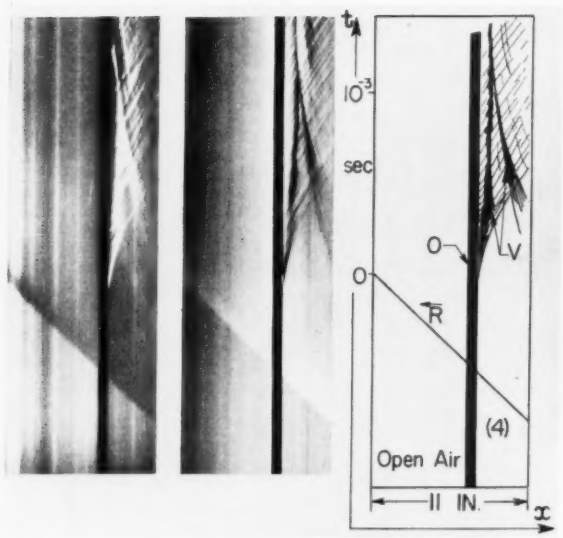

PLATE 17. Emergence of a rarefaction wave from the open end of a 3- by 3-in. chamber. R = head of rarefaction wave, V = vortices, O = open end of chamber, $p_4 = 740$ mm. Hg, $P_{41} = 370$, $T_{4,1} = 298°$K., and $a_4 = 1,135$ ft. per sec.

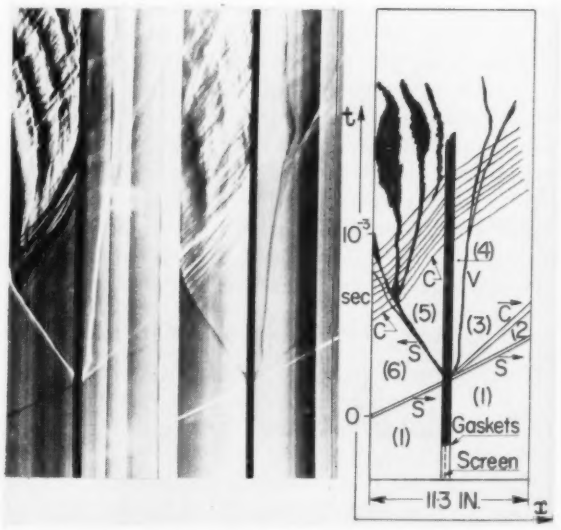

PLATE 19. The interaction of a shock wave with a No. 30 mesh screen.

V = vortex	$W_{61} = 1.98$	$U_{21} = 1.07$	$p_2 = p_3 = 59.5$ mm. Hg	
a_1 = 1,138 ft. per sec.	$W_{21} = 1.82$	$U_{41} = 0.54$	$p_6 = 71.6$ mm. Hg	
$p_1 = 16.1$ mm. Hg	$M_6 = 0.96$	$W_{56} = 1.48$	$p_5 = 172$ mm. Hg	
$P_{21} = 46.5$	$M_2 = 0.85$	$M_5 = 0.25$		

$p_3 = p_2$, the temperature $T_3 > T_2$. This is reasonable since region (5) has undergone two shock compressions, which also results in a low particle velocity u_5. Therefore, a rarefaction wave must exist which takes the high-pressure, low-velocity region (5) to the low-pressure, high-velocity region (3). The rarefaction wave is not seen on the records. However, along with the shock wave diffraction it may account for the formation of the vortex, which makes it impossible to determine state (4) from a wave speed analysis alone.

In reference 24 a solution is given for an analogous interaction that occurs for the magneto-hydrodynamic problem when a strong shock wave collides with a magnetic field. Because of the indeterminancy of state (4) it was not possible to compare the two cases.

However, the excellent reproducibility of the shock and screen interaction may lead to its utilization in the study of the "turbulent" contact front and the properties of wire gauzes in compressible flow turbulence research.

Conclusions

The theory of the shock tube is outlined in Part (1) from one-dimensional considerations. The modifications that are usually employed for flows with variable specific heats for rarefaction waves and shock waves are indicated. Some of the basic results for wave reflections, refractions, and collisions are included. For flows with large viscous effects such as in the diaphragm rupturing process, the transverse train of shock waves which follow the primary shock, the emergence of a shock wave and a rarefaction wave into free air, and the collision of a shock with a wire screen, a simple one-dimensional inviscid analysis is not possible. These problems still await adequate theoretical solutions.

In the study of the origin problem a real (x, t)-plane (see Plate 1) gives the appearance of a compression net of Mach lines which would result from the motion of a piston. Closer examination of the photographs shows that the head of the compression wave is supersonic and the region really consists of overtaking shock fronts which coalesce to form the primary shock wave.

Shock-wave attenuation is a defect in velocity which consists of a formation decrement and a distance attenuation. Both are absent for weak shock waves when viscous effects are small. The formation decrement increases with shock strength and the distance attenuation rate remains reasonably constant.

Concurrent with the shock attenuation phenomenon is associated the acceleration of the contact front. Like the shock front the contact front velocity is in agreement with theory for weak waves. It is noted that a unifying theory does not exist which will account for the shock attenuation measurements of different observers. An adequate theory must take into account the apparently paradoxical behavior of the contact front since it occurs simultaneously with shock-wave attenuation.

The flow uniformity of the constant state regions separated by the contact front has not been established experimentally over a wide range of initial conditions. Neither has it been confirmed that it is justified to derive the flow quantities from a measurement of the shock speed. These factors will have an important bearing on the use of the shock tube as an intermittent wind tunnel.

The attainability of high Mach Number in the state between the contact front and the rarefaction wave also requires an experimental decision. Little data are available on the physical quantities behind reflected shock and rarefaction waves.

One-dimensional wave interactions may be adequately analyzed by the simple wave-element theory in conjunction with the (p, u)-plane. This has been adequately substantiated by the wave interaction tube results.

Although emphasis has been placed on one-dimensional studies at the Institute of Aerophysics, some notable two- and three-dimensional work has also been conducted at Princeton University. Yet, it is difficult to state that the shock tube has proved itself as a type of intermittent wind tunnel on the basis of the work that has been done to date. The difficulties are due to

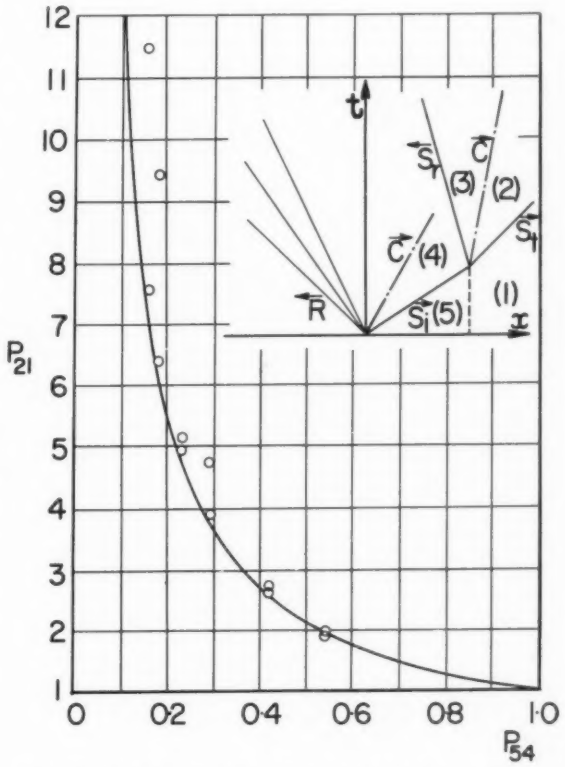

Fig. 34. Variation of the transmitted shock pressure ratio (P_{21}) with the incident shock pressure ratio (P_{45}) for the refraction of a shock wave and a contact surface. Case: Air‖A, $E_{15} = 0.431$.

the lack of direct rapid response instruments for the measurement of the transient flow quantities. Here, the interferometer has already achieved wide prominence, and other instruments are being developed. Little is known at present about the validity of applying nonstationary flow results to stationary flow which have associated boundary-layer and heat-transfer problems.

What certainly may be said without qualifications, judging from the wide utilization of the shock tube for numerous fundamental researches, is that the shock tube has proved itself to be a unique instrument for the investigation of basic problems in nonstationary fluid mechanics and possibly in the field of molecular physics.

Acknowledgments

The authors would like to express their appreciation to the former students of the Institute of Aerophysics whose names and reports are listed in the references. Their research work has aided materially in extending the knowledge of shock-tube flows.

The assistance received from J. de Leeuw in preparing the figures and proofreading the manuscript is gratefully acknowledged.

The generous financial support and encouragement of basic research by the Defence Research Board of Canada is acknowledged with thanks.

References

[1] Glass, I. I., Martin, W., and Patterson, G. N., *A Theoretical and Experimental Study of the Shock Tube*, Institute of Aerophysics, University of Toronto, UTIA Report No. 2, 1953.

[2] Bleakney, W., and Taub, A. H., *Interaction of Shock Waves*, Reviews of Modern Physics, Vol. 21, No. 4, pp. 584–605, 1949.

[3] Hall, J. G., *The Transition Through a Contact Region*, Institute of Aerophysics, University of Toronto, UTIA Report No. 26, 1953.

[4] Bethe, H. A., and Teller, E., *Deviations from Thermal Equilibrium in Shock Waves*, Aberdeen Proving Grounds, BRL Report X-117, 1945.

[5] Bitondo, D., Glass, I. I., and Patterson, G. N., *One-dimensional Theory of Absorption and Amplification of a Plane Shock Wave by a Gaseous Layer*, Institute of Aerophysics, University of Toronto, UTIA Report No. 5, 1950.

[6] Taylor, G. I., and Lewis, D. J., *The Instability of Liquid Surfaces When Accelerated in a Direction Perpendicular to Their Planes*, Proceedings of the Royal Society (London), Part 1, A201, 1950; Part 2, A202, 1950.

[7] Lobb, R. K., *On the Length of a Shock Tube*, Institute of Aerophysics, University of Toronto, UTIA Report No. 4, 1950.

[8] Glass, I. I., Correct solution for head-on collision of shock waves was given by author in an unpublished paper.

[9] Gould, D. G., *The Head-on Collision of Two Shock Waves and a Shock and Rarefaction Wave in One-dimensional Flow*, Institute of Aerophysics, University of Toronto, UTIA Report No. 17, 1952.

[10] Bull, G. V., Fowell, L. R., and Henshaw, D. H., *The Interaction of Two Similarly Facing Shock Waves*, Institute of Aerophysics, University of Toronto, UTIA Report No. 23, 1952.

[11] Steketee, J. A., *On the Interaction of Rarefaction Waves in a Shock Tube*, Institute of Aerophysics, University of Toronto, UTIA Review No. 4, 1952.

[12] Parks, E. K., *Supersonic Flow in a Shock Tube of Divergent Cross-Section*, Institute of Aerophysics, University of Toronto, UTIA Report No. 18, 1952.

[13] Hertzberg, A., and Smith, W. E., *Methods for Generating Strong Shock Waves*, Journal of Applied Physics, Vol. 25, No. 1, p. 130, 1954.

[14] Lukasiewicz, J., *Shock Tube Theory and Application*, National Aeronautical Establishment, Canada, Report No. 15.

[15] Resler, E. L., Lin, S. C., and Kantrowitz, A., *The Production of High Temperature Gases in Shock Tubes*, Journal of Applied Physics, Vol. 23, p. 1390, 1952.

[16] Goldstein, S., *Modern Developments in Fluid Dynamics*, Vol. 1, pp. 181–186; Oxford, 1938.

[17] Donaldson, C. du P., and Sullivan, R. D., *The Effect of Wall Friction on Strength of Shock Waves in Tubes and Hydraulic Jumps in Channels*, NACA TN 1942, 1949.

[18] Kuethe, A. M., and Schetzer, J. D., *Foundations of Aerodynamics;* John Wiley & Sons, Inc., New York, 1950.

[19] Lobb, R. K., *A Study of Supersonic Flows in a Shock Tube*, Institute of Aerophysics, University of Toronto, UTIA Report No. 8, 1950.

[20] Glass, I. I., *An Experimental Determination of the Speed of Sound in Gases from the Head of a Rarefaction Wave*, Institute of Aerophysics, University of Toronto, UTIA Report No. 9, 1952.

[21] Ford, A., and Glass, I. I., *An Experimental Study of Shock Wave Refraction*, Institute of Aerophysics, University of Toronto, UTIA Report No. 29, 1954.

[22] de Haller, P., *On a Graphical Method of Gas Dynamics*, Techniche Rundschau Sulzer No. 1, pp. 6–24, 1945; RTP Translation No. 2555.

[23] Bitondo, D., *Experiments on the Amplification of a Plane Shock Wave*, Institute of Aerophysics, University of Toronto, UTIA Report No. 7, 1950.

[24] Lin, S. C., *Electrical Conductivity of an Ionized Gas Produced by Strong Shock Waves*, Ph.D. Thesis, Cornell University, 1952.

A Method for Investigating the Influence of Flexibility of the Mounting Structure of Hydraulic Servo Systems on the Dynamic Stability Quality of Control Systems

HANS R. FRIEDRICH*

Convair-San Diego Division of General Dynamics Corporation

ABSTRACT

A method is presented for investigating the influence of flexibility in the mounting structure of hydraulic servo systems on the dynamic stability quality of control systems for missiles and airplanes.

It is shown that the compliance effects can be interpreted as a fictitious bulk modulus of the hydraulic fluid and a fictitious actuator leakage coefficient. Introduction of these fictitious terms permits treating the system as though the actuator were rigidly mounted.

Formulas and curves are presented which permit obtaining the fictitious leakage coefficient and the fictitious bulk modulus as functions of the real bulk modulus and the real leakage coefficient for any given overall servo loop system gain and ratio of true natural frequency of oil compressibility resonance to natural frequency of the mounting structure.

INTRODUCTION

TO OBTAIN RAPIDLY FIRST DESIGN SPECIFICATIONS in missile and airplane control problems, structural elasticity between the final control member and the actuating servomotor is often disregarded.

With these specifications the design of the hydraulic valve and actuator system is then optimized. However, it is not realized that the mount compliance might be so detrimental that it deteriorates the otherwise high performance quality of the servo system.

This paper includes the mount compliance into the control investigations. It shows that the compliance effects can be interpreted as a fictitious bulk modulus of the hydraulic fluid and a fictitious actuator leakage coefficient. Introduction of these fictitious terms permits treating the system as though the actuator were rigidly mounted.

BASIC EQUATIONS

The basic physical features of a closed electrohydraulic servo loop are shown in Fig. 1. In deriving the basic linearized equations the following assumptions are made.

(1) The various elements within the servo loop can be represented by lumped constants.

(2) Only small perturbations about steady-state operating conditions are considered.

(3) The actuator piston is balanced.

(4) The small masses of actuator cylinder, piston, and rod are neglected compared to the considerably larger mass of the control member.

From Fig. 1 then, the basic equations become as follows.

Amplifier:

$$i_S = K_A V_E \tag{1}$$

where

i_S = differential current, ma.
V_E = error signal input, volt
K_A = amplifier gain, ma./volt

Solenoid:

$$f_S = K_S i_S \tag{2}$$

where

f_S = magnetic force, lb.
K_S = solenoid gain, lb./ma.

Valve:

$$(\ddot{X}_V/\omega_V^2) + [(2\xi_V/\omega_V)\dot{X}_V] + X_V = f_S/k_V \tag{3}$$

where

$\omega_V = \sqrt{k_V/M_V}$ = natural frequency of valve, 1/sec.
$\xi_V = (1/2)\sqrt{b_V^2/(k_V M_V)}$ = damping ratio of valve, 1
k_V = spring constant, lb./ft.
b_V = damping factor, (lb./ft.)/sec.
M_V = mass of solenoid-valve system, slug
X_V = valve spool displacement from initial equilibrium position, ft.

Hydraulic Flow:

$$K_V X_V = [(V_a/B)\dot{p}] + l_a p + a(\dot{X}_{ap} - \dot{X}_{ac}) \tag{4a}$$

$$\begin{pmatrix}\text{Total}\\ \text{flow rate}\end{pmatrix} = \begin{pmatrix}\text{Compressibility}\\ \text{flow rate}\end{pmatrix} + \begin{pmatrix}\text{Leakage}\\ \text{flow rate}\end{pmatrix} + \begin{pmatrix}\text{Displacement}\\ \text{flow rate}\end{pmatrix}$$

Received March 25, 1954.

* Dynamics Group Engineer. Also, Lecturer in Engineering, University of California, Los Angeles.

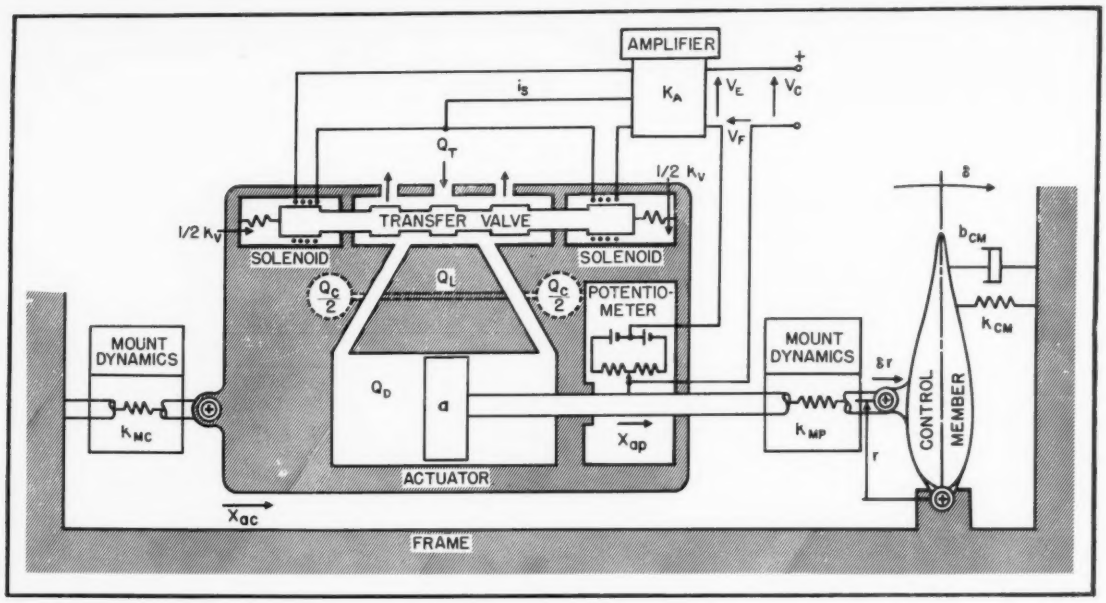

FIG. 1. Physical diagram of a hydraulic servo system.

Q_c = compressibility flow
Q_L = leakage flow
Q_D = displacement flow
Q_T = total flow

From Eq. (4a) follows

$$\frac{I_{CM}}{(ra)^2} K_V X_V = \frac{\dot{p}}{\omega_a^2} + \frac{2\xi_a}{\omega_a} p + \frac{I_{CM}}{r^2} \frac{1}{a} (\dot{X}_{ap} - \dot{X}_{ac}) \quad (4b)$$

where

ω_a = $\sqrt{[B(ra)^2]/(V_a I_{CM})}$ = natural frequency of oil compressibility resonance, 1/sec.
ξ_a = $(1/2) l_a \sqrt{(B I_{CM})/[V_a (ra)^2]}$ = damping ratio of oil compressibility resonance, 1
V_a = volume under compression, ft.^{3}
B = bulk modulus, lb./ft.^{2}
p = pressure across actuator piston, lb./ft.^{2}
l_a = leakage coefficient, (ft.^{3}/sec.)/(lb./ft.^{2})
a = actuator piston cross sectional area, ft.^{2}
X_{ap} = actuator piston displacement from initial equilibrium condition, ft.
X_{ac} = actuator cylinder displacement from initial equilibrium, ft.
r = arm from actuator piston to hinge point of final control member, ft.
I_{CM} = control member moment of inertia, slug ft.^{2}
K_V = valve flow gain, ft.^{2}/sec.

Actuator:

Cylinder: $$ap = -k_{MC} X_{ac} \quad (5a)$$

Piston: $$ap = k_{MP}(X_{ap} - r\delta) \quad (5b)$$

Eqs. (5a) and (5b) can be combined into the following relation:

$$(r^2 a / I_{CM}) p = -\omega_{MC}^2 X_{ac} = \omega_{MP}^2 (X_{ap} - r\delta) \quad (5c)$$

where

ω_{MP} = $\sqrt{(k_{MP} r^2)/I_{CM}}$ = natural frequency of mount between piston and control member, 1/sec.
ω_{MC} = $\sqrt{(k_{MC} r^2)/I_{CM}}$ = natural frequency of mount between actuator cylinder and frame, 1/sec.
k_{MP} = spring constant of mount between piston and control member, lb./ft.
k_{MC} = spring constant of mount between actuator cylinder and frame, lb./ft.
δ = control member deflection angle, radians, 1

Control Member:

$$\frac{\ddot{\delta}}{\omega_{CM}^2} + \frac{2\xi_{CM}}{\omega_{CM}} \dot{\delta} + \delta = \frac{1}{r} \frac{\omega_{MP}^2}{\omega_{CM}^2} (X_{ap} - r\delta) \quad (6)$$

where

ω_{CM} = $\sqrt{k_{CM}/I_{CM}}$ = natural frequency of control member, 1/sec.
ξ_{CM} = $(1/2) \sqrt{b_{CM}^2/(k_{CM} I_{CM})}$ = damping ratio of control member, 1
k_{CM} = any spring-type load torque on control member, lb. ft.
b_{CM} = any viscous type damping load torque on control member, lb. ft. sec.

Feedback:

$$V_f = K_f (X_{ap} - X_{ac}) \quad (7)$$

where

V_f = feedback signal, volt
K_f = feedback gain, volt/ft.

Eqs. (4) and (5) can be combined into the following equation:

$$\left(\frac{1}{\omega_a^2} + \frac{\omega_{MP}^2 + \omega_{MC}^2}{\omega_{MP}^2\omega_{MC}^2}\right)\ddot{p} + \frac{2\xi_a}{\omega_a}\dot{p} = \frac{I_{MC}}{(ra)^2}K_V X_V - \frac{I_{CM}}{(ra)}\ddot{\delta} \quad (8)$$

Eqs. (5) and (6) can be combined into the following equation:

$$(\ddot{\delta}/\omega_{CM}^2) + (2\xi_{CM}/\omega_{CM})\dot{\delta} + \delta = (ra/k_{CM})p \quad (9)$$

Eqs. (5)–(7) can be combined into the following equation:

$$V_f = rK_f \frac{1}{[(\omega_{MP}^2\omega_{MC}^2)/(\omega_{MP}^2 + \omega_{MC}^2)]} \times \left\{\ddot{\delta} + 2\xi_{CM}\omega_{CM}\dot{\delta} + \left[\omega_{CM}^2 + \left(\frac{\omega_{MP}^2\omega_{MC}^2}{\omega_{MP}^2 + \omega_{MC}^2}\right)\right]\delta\right\} \quad (10)$$

Introducing, for simplification and abbreviation, the resultant natural frequency of the entire mount

$$\omega_M = \omega_{MP}\omega_{MC}/\sqrt{\omega_{MP}^2 + \omega_{MC}^2} \quad (11)$$

Eqs. (8) and (10) can be written as

$$\left(\frac{1}{\omega_a^2} + \frac{1}{\omega_M^2}\right)\ddot{p} + \frac{2\xi_a}{\omega_a}\dot{p} = \frac{I_{CM}}{(ra)^2}K_V X_V - \frac{I_{CM}}{(ra)}\ddot{\delta} \quad (12)$$

$$V_f = rK_f(1/\omega_M^2)[\ddot{\delta} + 2\xi_{CM}\omega_{CM}\dot{\delta} + (\omega_{CM}^2 + \omega_M^2)\delta] \quad (13)$$

Operational Block Diagram

Application of Laplace transforms to Eqs. (1)–(3), (9), (12), and (13) with all initial conditions zero results in the following set of equations:

$$i_S(s) = K_A V_E(s) \quad (14)$$

$$f_S(s) = K_S i_S(s) \quad (15)$$

$$\{(s^2/\omega_V^2) + (2\xi_V/\omega_V)s + 1\}X_V(s) = f_S(s)/k_V \quad (16)$$

$$\left(\frac{s^2}{\omega_{CM}^2} + \frac{2\xi_{CM}}{\omega_{CM}}s + 1\right)\delta(s) = \frac{(ra)}{k_{CM}}p(s) \quad (17)$$

$$\left[\left(\frac{1}{\omega_a^2} + \frac{1}{\omega_M^2}\right)s + \frac{2\xi_a}{\omega_a}\right]p(s) = \frac{I_{CM}}{(ra)^2}K_V X_V(s) - \frac{I_{CM}}{(ra)}s\delta(s) \quad (18)$$

$$V_f(s) = rK_f(1/\omega_M^2)[s^2 + 2\xi_{CM}\omega_{CM}s + (\omega_{CM}^2 + \omega_M^2)]\delta(s) \quad (19)$$

From Eqs. (14)–(18) the following forward transfer function is obtained:

$$\frac{\delta(s)}{V_E(s)} = \frac{K_A K_S K_V}{k_V(ra)} 1\Big/\left(\left\{\left[\left(\frac{1}{\omega_a^2} + \frac{1}{\omega_M^2}\right)s + \frac{2\xi_a}{\omega_a}\right](s^2 + 2\xi_{CM}\omega_{CM}s + \omega_{CM}^2) + s\left\{\left(\frac{s^2}{\omega_V^2} + \frac{2\xi_V}{\omega_V}s + 1\right)\right)\right) \quad (20)$$

Combining this forward transfer function [Eq. (20)] with the feedback transfer function [Eq. (19)] in a degenerative closed feedback loop, the following closed-loop transfer function is obtained.

$$\frac{\delta(s)}{\theta_C(s)} = K_C\Big/\left(\left\{\left[\left(\frac{1}{\omega_a^2} + \frac{1}{\omega_M^2}\right)s + \frac{2\xi_a}{\omega_a}\right](s^2 + 2\xi_{CM}\omega_{CM}s + \omega_{CM}^2) + s\left\{\left(\frac{s^2}{\omega_V^2} + \frac{2\xi_V}{\omega_V}s + 1\right) + K_C\left[\frac{s^2}{\omega_M^2} + \frac{2\xi_{CM}\omega_{CM}}{\omega_M^2}s + \left(\frac{\omega_{CM}^2}{\omega_M^2} + 1\right)\right]\right]\right) \quad (21)$$

where

$K_C = (K_A K_S K_V K_F)/(C_V a)$ = overall servo system gain, 1/sec.
$\theta_C = V_C/(rK_F)$ = reference input, radians, 1

Eq. (21) can be rewritten in the following form

$$\frac{\delta(s)}{\theta_C(s)} = \left(\frac{K_C\frac{1}{s}\left[1\Big/\left(\frac{s^2}{\omega_V^2} + 2\frac{\xi_V}{\omega_V}s + 1\right)\right]}{1 + \frac{1}{s}\left\{\left(\frac{1}{\omega_a^2} + \frac{1}{\omega_M^2}\right)s + 2\frac{\xi_a}{\omega_a} + \frac{K_C}{\omega_M^2}\left[1\Big/\left(\frac{s^2}{\omega_V^2} + 2\frac{\xi_V}{\omega_V}s + 1\right)\right]\right\}(s^2 + 2\xi_{CM}\omega_{CM}s + \omega_{CM}^2)}\right) \div \left(1 + \frac{K_C\frac{1}{s}\left[1\Big/\left(\frac{s^2}{\omega_V^2} + 2\frac{\xi_V}{\omega_V}s + 1\right)\right]}{1 + \frac{1}{s}\left\{\left(\frac{1}{\omega_a^2} + \frac{1}{\omega_M^2}\right)s + 2\frac{\xi_a}{\omega_a} + \frac{K_C}{\omega_M^2}\left[1\Big/\left(\frac{s^2}{\omega_V^2} + 2\frac{\xi_V}{\omega_V}s + 1\right)\right]\right\}(s^2 + 2\xi_{CM}\omega_{CM}s + \omega_{CM}^2)}\right) \quad (22)$$

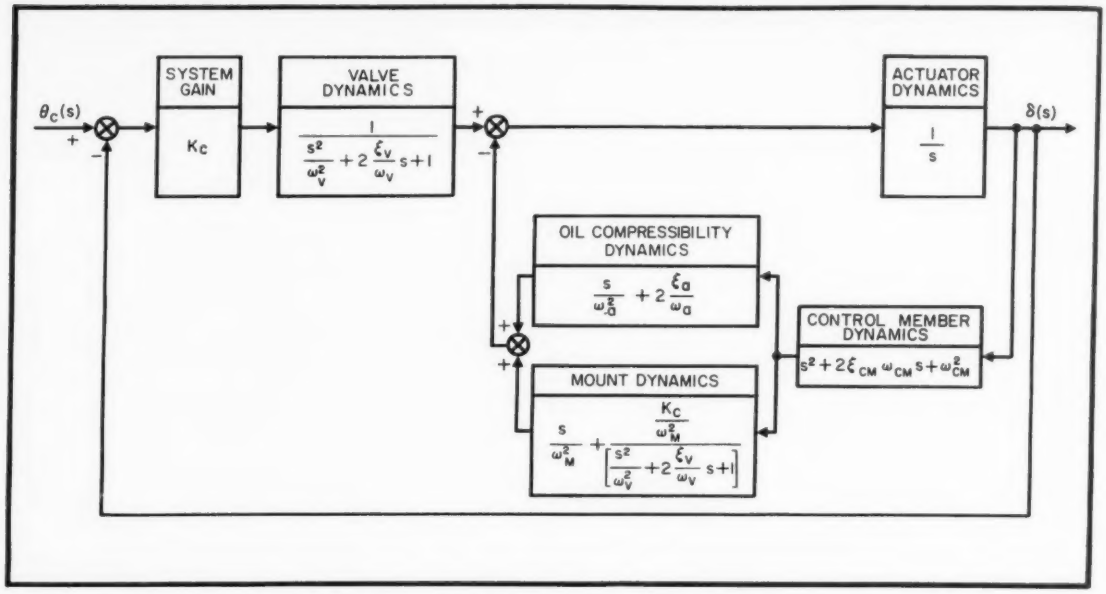

FIG. 2. Operational block diagram of servo system.

The closed-loop transfer function in the form given by Eq. (22) allows an extremely instructive block diagram representation, as shown in Fig. 2.

MODIFIED OPERATIONAL BLOCK DIAGRAM

It is generally permissible to assume that the natural frequency ω_V of the valve is high compared to the natural frequency of the structural mounts. Therefore it is possible to approximate the block "Mount Dynamics" in Fig. 2 by the following simplified transfer function.

$$(s/\omega_M{}^2) + 2\{[(1/2)\ (K_C/\omega_M)]/\omega_M\} \qquad (23)$$

This in turn permits combining the two parallel blocks, "Oil Compressibility Dynamics" and "Mount Dynamics," into one block with the following transfer function.

$$s\left(\frac{1}{\omega_a{}^2}+\frac{1}{\omega_M{}^2}\right)+2\left[\frac{\xi_a}{\omega_a}+\frac{(1/2)(K_C/\omega_M)}{\omega_M}\right]= \left\{s\Big/\left[\frac{\omega_a}{\sqrt{1+(\omega_a/\omega_M)^2}}\right]^2\right\}+ \frac{\left\{\left[1+\frac{K_c}{2\xi_a\omega_a}\left(\frac{\omega_a}{\omega_M}\right)^2\right]\Big/\sqrt{1+\left(\frac{\omega_a}{\omega_M}\right)^2}\right\}}{\left[\omega_a/\sqrt{1+(\omega_a/\omega_M)^2}\right]}\ \xi_a \qquad (24)$$

This transfer function can be interpreted as the transfer function describing the oil compressibility dynamics of a fictitious but rigidly mounted actuator with the following natural frequency and damping ratio.

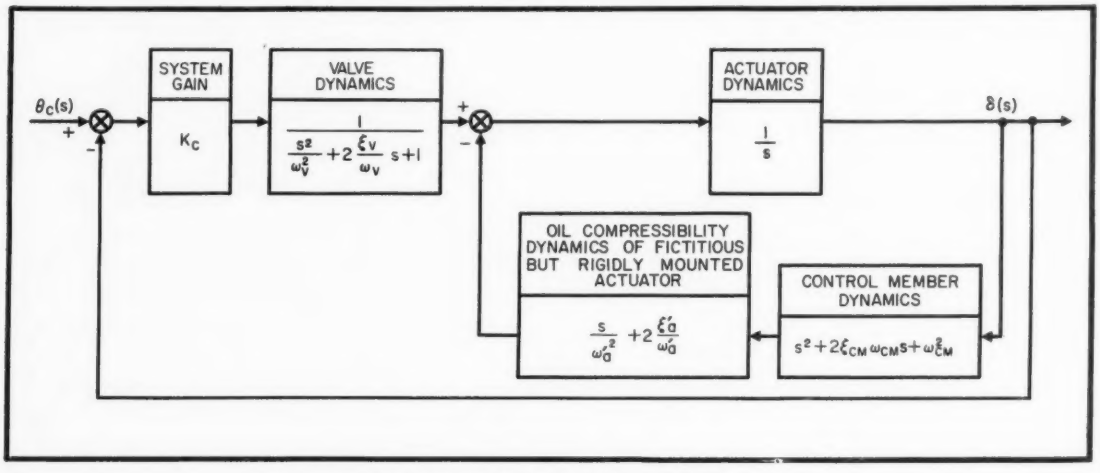

FIG. 3. Modified operational block diagram of servo system.

$$\omega_a' = \left[1 \Big/ \sqrt{1 + \left(\frac{\omega_a}{\omega_M}\right)^2}\right]\omega_a \quad \text{or}$$

$$\frac{1}{\omega_a'^2} = \left[1 + \left(\frac{\omega_a}{\omega_M}\right)^2\right]\frac{1}{\omega_a^2} \geqq \frac{1}{\omega_a^2} \qquad (25)$$

$$\xi_a' = \left\{\left[1 + \frac{K_c}{2\xi_a\omega_a}\left(\frac{\omega_a}{\omega_M}\right)^2\right] \Big/ \sqrt{1 + \left(\frac{\omega_a}{\omega_M}\right)^2}\right\}\xi_a \quad \text{or}$$

$$\frac{2\xi_a'}{\omega_a'} = \left[1 + \frac{K_c}{2\xi_a\omega_a}\left(\frac{\omega_a}{\omega_M}\right)^2\right]\frac{2\xi_a}{\omega_a} \geqq \frac{2\xi_a}{\omega_a} \qquad (26)$$

The block diagram of Fig. 2 can, therefore, be reduced to the simplified block diagram of Fig. 3.

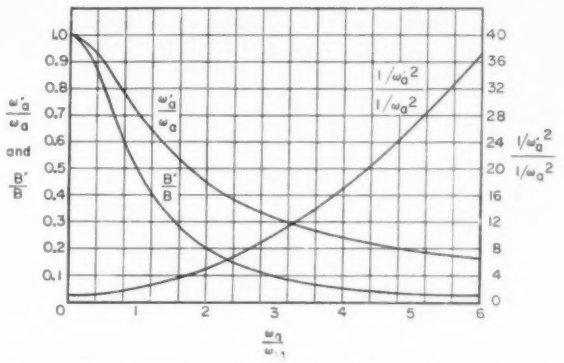

FIG. 4. Ratios B'/B; ω_a'/ω_a; and $(1/\omega_a'^2)/(1/\omega_a^2)$ versus the ratio ω_a/ω_M.

B, B' = real and fictitious bulk modulus
ω_a, ω_a' = real and fictitious natural frequency of the oil compressibility resonance
ω_M = resultant natural frequency of mount

Modified Bulk Modulus and Leakage Coefficient

Assuming for this fictitious but rigidly mounted actuator the same mechanical and geometrical properties as for the real actuator, the natural frequencies ω_a' and the damping ratio ξ_a' can be obtained as a result of a fictitious bulk modulus B' and a fictitious leakage coefficient l_a'.

The following equations hold true for the real and fictitious actuator.

$$\omega_a = \sqrt{\frac{B(ra)^2}{V_a I_{CM}}} \qquad \omega_a' = \sqrt{\frac{B'(ra)^2}{V_a I_{CM}}} \qquad (27)$$

$$\xi_a = \frac{1}{2} l_a \sqrt{\frac{BI_{CM}}{V_a(ra)^2}} \qquad \xi_a' = \frac{1}{2} l_a' \sqrt{\frac{B'I_{CM}}{V_a(ra)^2}} \qquad (28)$$

From a comparison of Eqs. (25) and (27) it follows that for the fictitious bulk modulus B'

$$\frac{B'}{B} = \frac{1}{1 + (\omega_a/\omega_M)^2} = \frac{\omega_a'^2}{\omega_a^2} \qquad (29)$$

From a comparison of Eqs. (26) and (28) it follows that for the fictitious leakage coefficient

$$\frac{l_a'}{l_a} = 1 + \frac{K_C}{2\xi_a\omega_a}\left(\frac{\omega_a}{\omega_M}\right)^2 = \left(\frac{2\xi_a'}{\omega_a'}\right) \Big/ \left(\frac{2\xi_a}{\omega_a}\right) \qquad (30)$$

These two equations indicate that the structural compliance of the servo mount acts as if the compressibility of the hydraulic fluid as well as the leakage flow of the actuator has been increased. The resultant natural frequency, ω_a', of the fictitious oil compressibility resonance of the actuator is smaller than ω_a as well as smaller than ω_M, as can be seen by rewriting Eq. (25) in the following form.

$$\omega_a' = \omega_M / \sqrt{1 + (\omega_M/\omega_a)^2} \qquad (31)$$

Fig. 4 is a graphical representation of Eqs. (25) and (29), while Fig. 5 is a graphical representation of Eqs. (26) and (30) with $K = K_C/2\xi_a\omega_a$ as a parameter.

A comparison of Figs. (4) and (5) indicates that the following relations exist for any ratio $\omega_a/\omega_M \geqq 0$

$$(\xi_a'/\omega_a')/(\xi_a/\omega_a) \lessgtr (1/\omega_a'^2)/(1/\omega_a^2) \qquad (32)$$

for $K \lessgtr 1$ or $K_C \lessgtr 2\,\xi_a\omega_a$.

It can now be shown that for practical purposes only parameter values $K < 1$—i.e., $K_C < 2\xi_a\omega_a$ should be considered.

For $\omega_M = \infty$ Fig. 3 represents the block diagram of a rigidly mounted servo system, $\omega_a' = \omega_a$; $\xi_a' = \xi_a$. The closed-loop transfer function of such a servo system can be taken from Eq. (21) for $\omega_M = \infty$.

$$\frac{\delta(s)}{\theta_C(s)} = K_C \Big/ \left\{\left[\left(\frac{s}{\omega_a^2} + \frac{2\xi_a}{\omega_a}\right)(s^2 + 2\xi_{CM}\omega_{CM}s + \omega_{CM}^2) + s\right]\left(\frac{s^2}{\omega_V^2} + \frac{2\xi_V}{\omega_V}s + 1\right) + K_C\right\} \qquad (33)$$

If the valve is idealized by assuming $\omega_V = \infty$, Eq. (33) reduces to

$$\frac{\delta(s)}{\theta_C(s)} = K_C \Big/ \left\{\left[\left(\frac{s}{\omega_a^2} + \frac{2\xi_a}{\omega_a}\right)(s^2 + 2\xi_{CM}\omega_{CM}s + \omega_{CM}^2) + s\right] + K_C\right\} \qquad (33a)$$

If additionally the actuator is idealized by assuming $\omega_a = \infty$, Eq. (33a) reduces to

$$\delta(s)/\theta_C(s) = K_C/(s + K_C) \qquad (33b)$$

Application of the servo loop as part of the forward loop in a closed control loop of an airplane or missile, as shown in Fig. 6, gives the following closed-loop transfer function for $\omega_M = \infty$.

$$\frac{\theta_0(s)}{\theta_R(s)} = \left\{ \frac{N_{FW}(s)}{D_{FW}(s)} \frac{K_C\omega_a{}^2\omega_V{}^2}{[(s + 2\xi_a\omega_a)\,(s^2 + 2\xi_{CM}\omega_{CM}s + \omega_{CM}{}^2) + \omega_a{}^2 s]\,(s^2 + 2\xi_V\omega_V s + \omega_V{}^2) + K_C\omega_a{}^2\omega_V{}^2} \right\} \div$$
$$\left\{ 1 + \frac{N_{FB}(s)}{D_{FB}(s)} \frac{N_{FW}(s)}{D_{FW}(s)} \frac{K_C\omega_a{}^2\omega_V{}^2}{[(s + 2\xi_a\omega_a)\,(s^2 + 2\xi_{CM}\omega_{CM}s + \omega_{CM}{}^2) + \omega_a{}^2 s]\,(s^2 + 2\xi_V\omega_V s + \omega_V{}^2) + K_C\omega_a{}^2\omega_V{}^2} \right\} \quad (34)$$

For the idealized valve it follows that with $\omega_V = \infty$.

$$\frac{\theta_0(s)}{\theta_R(s)} = \left\{ \frac{N_{FW}(s)}{D_{FW}(s)} \frac{K_C\omega_a{}^2}{[(s + 2\xi_a\omega_a)\,(s^2 + 2\xi_{CM}\omega_{CM}s + \omega_{CM}{}^2) + \omega_a{}^2 s] + K_C\omega_a{}^2} \right\} \div$$
$$\left\{ 1 + \frac{N_{FB}(s)}{D_{FB}(s)} \frac{N_{FW}(s)}{D_{FW}(s)} \frac{K_C\omega_a{}^2}{[(s + 2\xi_a\omega_a)\,(s^2 + 2\xi_{CM}\omega_{CM}s + \omega_{CM}{}^2) + \omega_a{}^2 s] + K_C\omega_a{}^2} \right\} \quad (34a)$$

For the idealized actuator and valve it follows that with $\omega_V = \infty$ and $\omega_a = \infty$

$$\frac{\theta_0(s)}{\theta_R(s)} = \left[\frac{N_{FW}(s)}{D_{FW}(s)} \frac{K_C}{K_C + s} \right] \Big/ \left[1 + \frac{N_{FB}(s)}{D_{FB}(s)} \frac{N_{FW}(s)}{D_{FW}(s)} \frac{K_C}{s + K_C} \right] \quad (34b)$$

where

θ_0	=	output variable of the controlled system
θ_R	=	reference variable of the controlled system
$[N_{FW}(s)]/[D_{FW}(s)]$	=	net transfer function of the forward loop outside the servo loop
$[N_{FB}(s)]/[D_{FB}(s)]$	=	net transfer function of the feedback loop

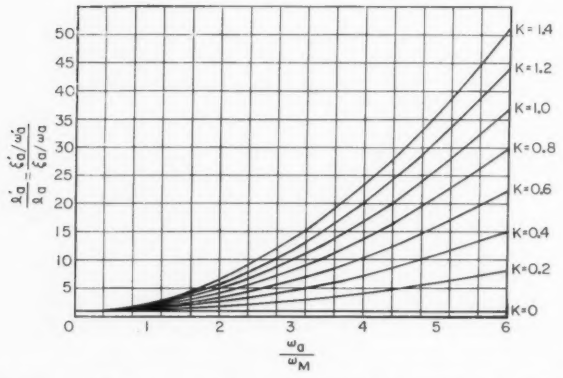

FIG. 5. Ratios l_a'/l_a and $(\xi_a'/\omega_a')/(\xi_a/\omega_a)$ versus the ratio ω_a/ω_M with $K = K_c/2\xi_a\omega_a$ as parameter.

l_a, l_a'	=	real and fictitious leakage coefficient
ξ_a, ξ_a'	=	real and fictitious damping ratio of the oil compressibility resonance
ω_a, ω_a'	=	real and fictitious natural frequency of the oil compressibility resonance
ω_M	=	resultant natural frequency of mount
K_c	=	overall servo system gain

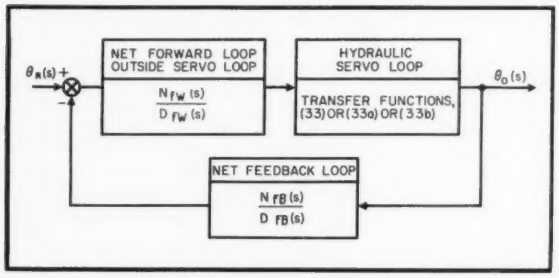

FIG. 6. Block diagram for complete control system.

For physical systems, the following nonrestricting assumption can be made for any control loop concerning missile and airplane control systems.

If as a reference input a step

$$\theta_R(s) = |\theta_R|/s \quad (35)$$

is applied to the system at $t = 0$ sec. with zero initial conditions for the output variable θ_0, the true initial error $\lim_{s\to\infty} s[\theta_R(s) - \theta_0(s)]$ is equal to the initial actuating error $\lim_{s\to\infty} s\{\theta_R(s) - [N_{FB}(s)/D_{FB}(s)]\theta_0(s)\}$ which in turn can be assumed to be equal to the step height $|\theta_R|$. This means that the product of the total forward transfer function times the total feedback transfer function of the loop has the limiting value zero for $s \to \infty$. This, in turn, means that the degree of the numerator polynomial of the product is at least one lower than the degree of the denominator polynomial. In order that even the most idealized case of Eq. (34b) describes a reasonable physical control system it is necessary that the degree of the polynomial $N_{FB}(s)N_{FW}(s)$ is less than or equal to the degree of the polynomial $D_{FB}(s)D_{FW}(s)$.

With this result and assuming for the two polynomials the expressions

$$\left.\begin{aligned} N_{FB}(s)N_{FW}(s) &= N_n s^n + N_{n-1}s^{n-1} + N_{n-2} \\ &\quad s^{n-2} + \ldots + N_2 s^2 + N_1 s + N_0 \quad N_n \geqq 0 \\ D_{FB}(s)D_{FW}(s) &= s^n + D_{n-1}s^{n-1} + \\ &\quad D_{n-2}s^{n-2} + \ldots + D_2 s^2 + D_1 s + D_0 \end{aligned}\right\} \quad (36)$$

the characteristic equations can be found from the denominators of Eqs. (34)–(34b). They are

(*Continued on page 123*)

On Some Solutions of the Hodograph Equation Which Yield Transonic Flows Through a Laval Nozzle

F. EDWARD EHLERS*

Boeing Airplane Company and Oregon State College

SUMMARY

The properties of a one parameter family of solutions of the Tricomi equation are studied which have the sonic singularity

$$(\psi_\theta)_{\psi=0} \sim (1/s)^\mu$$

as $s \to 0$ where ψ is the stream function, θ is the direction of flow, and s is a function of the velocity such that $s = 0$ for the sonic velocity. These solutions represent the stream functions for transonic flows through a Laval nozzle. For a value of the parameter $\mu = 1$, the solution yields a sonic line that is concave to the incoming flow and has positive, nonzero curvature. The acceleration across the sonic line is positive and nonzero along all streamlines. A family of solutions yielding nozzles with discontinuous wall curvature is also obtained and discussed. For $1 < \mu < 3/2$, the flow pattern is similar to that for $\mu = 1$, but the sonic line has zero curvature at the axis of the nozzle, and the acceleration at the sonic point is zero for the center streamline but positive for all other streamlines. For $3/2 \leq \mu < 1/4$, the sonic line is straight with all streamlines having zero curvature and zero acceleration at the sonic point.

For values of $\mu = 1$ and $3/2$, the hodograph solutions are simple, and the computation of the throat of a nozzle is practical. By means of Loewner's transformation of the hogodgraph equations, good agreement with the exact equations is obtained in the Mach Number range from 0.8 to 1.35. A method for designing perfect nozzles by means of these solutions is also given.

SYMBOLS

A, B, C, D, E = constants depending on the parameter μ
f = linearization for $1/\rho$, defined by $f'(s^*)/f(s^*)$
dl = element of arc length
M = Mach Number
p = pressure (equals unity for stagnation condition)
q = velocity magnitude normalized to the stagnation sound velocity
q^* = critical velocity or the flow velocity for which the local velocity equals the sound velocity
r = $(\theta^2 + 4s^3/9)^{1/2}$
s^* = $\int_q^{q^*} (\rho/q)dq$
s = $2.1120\ s^*/(1 + 1.2304\ s^*)$
t = $2r/(\theta - r)$, also used as $t = 2s^{3/2}/3$
u, v = Cartesian components of the velocity
V = specific volume, $1/\rho$
x, y = Cartesian coordinates
z = $x + iy$
α = $\{[4(-s)^{3/2}/9] - \theta^2\}^{1/2}$
β = $1/(\gamma - 1)$
γ = ratio of specific heats ($\gamma = 1.4$)
α and β also used in transformation $(\theta + it + it_0)/(\theta + it - it_0) = e^{\alpha+i\beta}$
δ = $\cos^{-1}\theta/[(4/9)(-s)^3]$
ξ = $[1.6118\ s^*/(1 + 1.2304\ s^*)]^{3/2}$ in $1/\rho$ relation; also $\xi = \sqrt{\eta}$
$\tilde{\xi}$ = $[-1.6118\ s^*/(1 + 1.2304\ s^*)]^{3/2}$, $s^* < 0$
η = $-(9/4)(\theta^2/s^3)$
ρ = density (unity for stagnation)
ρ^* = critical density
ω_1 = $1.45320 - 0.84664s$
ω^* = $(1 - M^2)/\rho^2 = 9.4204s^*/(1 - 1.2304s^*)^5$
μ = singularity parameter
θ = angle of flow
φ = velocity potential
φ' = related potential [Eq. (5)]
ψ = streamfunction
ψ' = $\omega_1\psi$

(I) INTRODUCTION

THE DISCOVERY THAT A GAS could be accelerated to supersonic velocities by forcing it through a constriction was made by a Swedish engineer, De Laval. The first attempt to construct analytically the streamlines and lines of constant velocity in the neighborhood of the throat of such a constriction was made by Meyer[1] in his 1908 dissertation. Meyer expanded the velocity potential in a power series in x and y, the Cartesian coordinates about the critical point of the nozzle. Later, Taylor,[2] using a method similar to Meyer's, computed the transonic region in a nozzle whose walls consisted of arcs of circles. Both of these methods employed series expansions, and, since there is no knowledge concerning the convergence of these power series, conclusions drawn from them cannot be relied upon with certainty.

The nature of the hodograph of the continuously accelerated flow through a nozzle was investigated by Lighthill[3] and Frankl.[4] Their analysis showed that the derivative of the streamfunction with respect to θ, the angle of flow, was singular at the critical point of the straight streamline and that the streamfunction is triple-valued in a region of the hodograph plane bounded by one pair of characteristics which pass through the sonic velocity and $\theta = 0$.

Using a transformation of the hodograph equations, Loewner[7] developed an approximate hodograph method that is based upon a hypothetical pressure density rela-

Received March 25, 1954.

* Aerodynamicist, Boeing Airplane Co., on leave from the Mathematics Department, Oregon State College.

tion that gives good agreement with the adiabatic, isentropic relation in the Mach Number range from 0.8 to 1.35. At the sonic point the values of pressure, p, and the derivatives with respect to the density ρ, $dp/d\rho$, $d^2p/d\rho^2$, and $d^3p/d\rho^3$, agree with the values obtained from the adiabatic isentropic relation: $p = \rho^7$. The resulting differential equation to be solved for the streamfunction is the Tricomi equation in the transformed hodograph variables.

In this paper we shall study some solutions of the Tricomi equation which can be shown to yield the hodographs of flows through a Laval nozzle. We shall investigate some of the properties of these flows as exhibited by the singularities of their hodograph solutions.

(II) The Approximate Hodograph Method for Compressible Flow

The equations for the isentropic, nonviscous, irrotational flow of a compressible fluid are

$$\left.\begin{aligned} \partial\varphi/\partial x &= (1/\rho)\,(\partial\psi/\partial y) \\ \partial\varphi/\partial y &= -(1/\rho)\,(\partial\psi/\partial x) \end{aligned}\right\} \tag{1}$$

where ρ is the dimensionless density and equals unity for zero velocity. The quantities ψ and φ are the streamfunction and velocity potential, respectively; and x and y are the Cartesian coordinates of the flow. Chaplygin[11] and Molenbroek[10] have shown that these equations can be linearized by transformation to the variables of the hodograph plane. With $u = \partial\psi/\partial x$, $v = \partial\varphi/\partial y$, and Eqs. (1) we have

$$\begin{aligned} d\varphi + (i/\rho)d\psi &= (udx + vdy) + i(-vdx + udy) \\ &= qe^{-i\theta}\,dz \end{aligned}$$

The quantity q is the velocity magnitude, and θ is the flow angle. Solving for dz, we obtain

$$dz = (1q)e^{i\theta}\left\{d\varphi + [(i/\rho)d\psi]\right\} \tag{2}$$

The elements dx and dy are easily found by separating Eq. (2) into its real and imaginary parts.

Let us now consider q and θ as independent variables. We then can write Eq. (2) as

$$\frac{\partial z}{\partial\theta} = \frac{1}{q}\,e^{i\theta}\left(\frac{\partial\varphi}{\partial\theta} + \frac{i}{\rho}\,\frac{\partial\psi}{\partial\theta}\right)$$

and

$$\frac{\partial z}{\partial q} = \frac{1}{q}\,e^{i\theta}\left(\frac{\partial\varphi}{\partial q} + \frac{i}{\rho}\,\frac{\partial\psi}{\partial q}\right)$$

Assuming that ρ is a function of the variable q only, we differentiate the first expression with respect to q and the second with respect to θ. Since $\partial^2 z/\partial\theta\partial q = \partial^2 z/\partial g\partial\theta$, it follows that

$$\frac{i}{q}\,e^{i\theta}\left(\frac{\partial\varphi}{\partial q} + \frac{i}{\rho}\,\frac{\partial\psi}{\partial q}\right) = e^{i\theta}\left[-\frac{1}{q^2}\,\frac{\partial\varphi}{\partial\theta} + i\,\frac{d}{dq}\left(\frac{1}{\rho q}\right)\frac{\partial\psi}{\partial\theta}\right]$$

Equating real and imaginary parts yields

$$\partial\varphi/\partial\theta = (q/\rho)\,(\partial\psi/\partial q)$$

$$q\,\frac{\partial\varphi}{\partial q} = \left[q\,\frac{d}{dq}\left(\frac{1}{\rho}\right) - \frac{1}{\rho}\right]\frac{\partial\psi}{\partial\theta}$$

These are the hodograph equations first obtained by Molenbroek.[10] Since ρ is a function of q, these equations are linear. Therefore, the principle of superposition of solutions may be applied to find the velocity potential and the streamfunction in terms of the hodograph variables. Since the resulting solutions for the streamfunction and velocity potential of a flow are expressed in the hodograph variables, the mapping to the physical plane must be obtained by integrating Eq. (2).

For our own purposes it is convenient to introduce another variable defined by $\partial/\partial s^* = -(q/\rho)\,(\partial/\partial q)$. This results in the following pair of equations.

$$\left.\begin{aligned} \partial\varphi/\partial\theta &= -(\partial\psi/\partial s^*) \\ \partial\varphi/\partial s^* &= \omega^*(\partial\psi/\partial\theta),\ \omega^* = \\ &\quad (d/ds^*)\,(1/\rho) + (1/\rho^2) \end{aligned}\right\} \tag{3}$$

We shall approximate the quantity ω^* to obtain a more simple pair of equations valid in the neighborhood of the sonic velocity.

Loewner has developed the general forms of two simultaneous differential equations in two dependent variables which reduce to the Tricomi equation for one of these variables by means of a Baecklund transformation. We shall consider one such form. Let ψ and φ be defined by the relations

$$\left.\begin{aligned} \omega_1(\partial\psi/\partial s) &= -(1/\omega_1)\,(\partial\varphi/\partial\theta) \\ (1/\omega_1)\,(\partial\varphi/\partial s) &= s\omega_1\,(\partial\psi/\partial\theta) \end{aligned}\right\} \tag{4}$$

Now consider a transformation of the dependent variables given by

$$\left.\begin{aligned} \psi' &= \omega_1\psi \\ \varphi_s' &= -(1/\omega_1)\varphi_s \\ \varphi_\theta' &= -(1/\omega_1)\varphi_\theta + (d\omega_1/ds)\psi \end{aligned}\right\} \tag{5}$$

By eliminating φ' from the preceding equations, we see that $d\omega_1{}^2/ds^2$ must be zero if the resulting expression is to be compatible with Eqs. (4). Hence, we must have

$$\omega_1 = as + b$$

Substituting Eqs. (5) into Eqs. (4) we obtain

$$\left.\begin{aligned} \psi_s' &= \varphi_\theta' \\ \varphi_s' &= -s\psi_\theta' \end{aligned}\right\} \tag{6}$$

These relations lead to the Tricomi equation

$$\psi_{ss}' + s\psi_{\theta\theta}' = 0 \tag{7}$$

by eliminating φ'. Now Eqs. (4) may be written in the same form as Eqs. (3) by the introduction of a new independent variable s^*. Thus

$$\left.\begin{aligned}\frac{\partial\psi}{\partial s^*} &= -\frac{1}{\omega_1^2}\frac{ds}{ds^*}\frac{\partial\varphi}{\partial\theta}\\ \frac{\partial\varphi}{\partial s^*} &= s\omega_1^2\frac{ds}{ds^*}\frac{\partial\psi}{\partial\theta} = \tilde{\omega}\frac{\partial\psi}{\partial\theta}\end{aligned}\right\} \tag{8}$$

By comparing these equations with Eqs. (3), we obtain

$$s^* = \int\frac{ds}{\omega^2} + \text{constant} = \frac{s}{b(as+b)}$$

and we have

$$\tilde{\omega} = s\omega_1^4$$

In terms of s^*,

$$s = b^2s^*/(1 - abs^*)$$

from which

$$\tilde{\omega} = b^6s^*/(1 - ab\,s^{*5})$$

The function $\tilde{\omega}$ can be made to approximate ω^* best by determining the two constants so that the first two derivatives of ω^* and $\tilde{\omega}$ coincide at the sonic velocity. Thus

$$\left(\frac{d\tilde{\omega}}{ds^*}\right)_{s^*=0} = \left[\left(\frac{d\omega^*}{dq}\right)\frac{dq}{ds^*}\right]_{q=2\beta/(2\beta+1)} = 2\left(\frac{\gamma+1}{2}\right)^{(\gamma+2)/(\gamma-1)}$$

$$(d^2\tilde{\omega}/ds^{2*})_{s^*=0} = -2(2\gamma+5)\,[(\gamma+1)/2]^{(\gamma+3)/(\gamma-1)}$$

From this we obtain, for $\gamma = 1.4$,

$$\begin{aligned}\tilde{\omega} &= 9.4204\,s^*/(1 + 1.2304\,s^*)^5 \qquad (9)\\ s &= 2.1120\,s^*/(1 + 1.2304\,\delta^*)\\ \omega_1 &= (1.45320 - 0.84664\,s)\end{aligned}$$

and $\psi = (1.45320 - 0.84664\,s)^{-1}\,\psi'$. The function ψ' for our purpose will have the same singularities as ψ since $1/\omega_1$ is not singular in the region in which we are interested.

(III) The Equation of State of the Gas Leading to the Tricomi Equation as the Exact Hodograph Equation

In the above analysis we have approximated the differential equation for the streamfunction ψ in the neighborhood of the sonic point by the Tricomi equation in a related function ψ'. Now from the standpoint of understanding the range of validity of our approximation, it is better to find the pressure-density relation that yields the Tricomi equation as the exact differential equation for the related function ψ'. We can then see how well this pressure-density relation approximates the adiabatic relation for the ratio of specific heats $\gamma = 1.4$. To this end, we shall write the quantity ω^* in Eq. (3) in the form

$$\omega^* = (1/\rho^2) - [(1/\rho^2)\,(d\rho/ds^*)]$$

$$\omega^* = V^2 + (dV/ds^*)$$

Here we have replaced the reciprocal of the density by the specific volume V. After substituting the approximation for $\omega^*(s)$, we obtain the following differential equation for V.

$$(dV/ds^*) + V^2 = b^6s^*(1 - abs^*)^{-5} \tag{10}$$

Since we require our solution in the neighborhood of $s^* = 0$, we shall obtain a power series for V. Accordingly, we substitute

$$V = \sum_{n=0}^{\infty} a_n s^{*n}$$

into Eq. (10). After equating coefficients of like powers of s^* and evaluating the constants, we obtain

$$1/\rho = 1.5774 - 2.4883\,s^* + 8.6354\,s^{*2} - 30.175\,s^{*3} + 88.024\,s^{*4} - 223.32\,s^{*5} + \ldots \tag{11}$$

The first four terms agree with the expansion of $1/\rho$ in powers of s^* for the adiabatic pressure-density relation for $\gamma = 1.4$.

It is now possible to check the agreement of the pressure-density relation with the actual adiabatic relation at the sonic point. First of all we must have an expression for q, the velocity magnitude for our new gas, from which we calculate the pressure p. For this we make use of the differential relation between our variable s^* and the velocity magnitude q—namely,

$$-\rho(dq/q) = ds^*$$

or

$$-(1/q^2)\,(dq/ds^*) = 1/\rho q$$

Finally

$$(d/ds^*)\,(1/q) = (1/\rho)\,(1/q)$$

The nth derivative is

$$\frac{d^n}{ds^{*n}}\left(\frac{1}{q}\right) = \sum_{n=0}^{n-1}\binom{n-1}{m}\frac{d}{ds^{*m}}\left(\frac{1}{\rho}\right)\frac{d^{m-n-1}}{ds^{*m-n-1}}\left(\frac{1}{q}\right)$$

These derivatives may be evaluated successively at $s^* = 0$; and a MacLaurin expansion for $1/q$ then may be obtained. The final expansion for $1/q$ with the proper numerical values substituted for ρ and q at $s^* = 0$ is

$$1/q = 1.0954 + 1.7280\,s^* + 1.7199\,s^{*3} - 3.9340\,s^{*4} + 6.7097\,s^{*5} - 9.5639\,s^{*6} + \ldots \tag{12}$$

The coefficients in the expansion for $1/q$ agree to the fourth power in s^* with the actual expansion of $1/q$ for $\gamma = 1.4$ and the series for q, of course, will also agree to the fourth order in s^*. Now an expansion for p may be calculated from Bernoulli's equation—namely,

$$\left.\begin{aligned} &\gamma(dp/\rho) + q\,dq = 0 \\ \text{or} \\ &\gamma(dp/ds^*) = q^2 \end{aligned}\right\} \qquad (13)$$

The quantity γ appears from normalizing p, ρ with their stagnation quantities and q with the stagnation sound velocity. Now

$$\gamma(dp/d\rho) = q^2(d\,s^*/d\rho) = \sum_{n=0}^{\infty} c_n\, s^{*n}$$

Since $d\rho/ds^*$ is correct to the second order in s^* then c_0, c_1, and c_2 will be the exact values of the coefficients for the adiabatic equation of state. Thus at $s^* = 0$, $dp/d\rho$ for our new gas will coincide with the adiabatic relation. By successive differentiations it can be seen that $d^2\rho/d\rho^2$ and $d^3p/d\rho^3$ agree with the adiabatic relations at $s^* = 0$. If $a = 0$ in the expression for ω_1 following Eq. (5), however, the p, ρ relation will agree only up to the second derivative $d^2p/d\rho^2$ at $s^* = 0$.

Knowing the expansion for q^2, we are then able to obtain the pressure-density relation in parametric form. Now from Bernoulli's equation in differential form we have

$$\gamma\frac{dp}{ds^*} = q^2 = 1\Big/\left(\sum_{n=0}^{\infty} d_n s^{*n}\right)^2 = \sum_{n=0}^{\infty} e_n s^{*n}$$

where d_n is the coefficient of s^{*n} in the expansion for $1/q$. Evaluating the coefficients e_m and integrating gives us the following expansion for $p - p_s$.

$$\gamma(p - p_s) = 0.8333\,s^* - 1.3145\,s^{*2} + 0.6912\,s^{*3} - 0.3816\,s^{*4} + 1.0939\,s^{*5} - 1.3948\,s^{*6} + \ldots \qquad (14)$$

This relation in conjunction with Eq. (11) constitutes the pressure-density relation leading to the Tricomi equation.

In the preceding paragraphs we used a power series for $1/\rho$. Unfortunately the coefficient of s^{*n} in the power series increases rapidly with n so that the series converges extremely slowly. It is possible to obtain a solution of the Riccati equation in closed form. If we let $1/\rho = f'/f$ in Eq. (10), we obtain

$$(1 + cs^*)^5 f'' = ds^* f$$

where $c = 1.2304$ and $d = 9.4204$ are substituted for convenience. This equation may be simplified by letting

$$f = (1 + cs^*)W(x)$$

where $x = 1/(1 + cs^*)$. In terms of the new variable x, the differential equation becomes

$$W_{xx} = (d/c^3)\,(1 - x)W$$

Another transformation, $\eta = (d^{1/3}/c)\,(1 - x)$, yields

$$W_{\eta\eta} - \eta W = 0$$

This is the well-known Airy equation whose solutions are

$$\eta^{1/2} I_{\pm 1/3}\left(\frac{2}{3}\eta^{3/2}\right)$$

A linear combination of these two functions gives us our general solution; thus

$$f = (1 + cs^*)\,[A\xi^{1/3} I_{1/3}(\xi) + B\xi^{1/3} I_{-2/3}(\xi)]$$

where $\xi = {}^2/_3\eta^{3/2}$. Since $1/\rho = f'/f$, we are only at liberty to determine the ratio A/B by boundary conditions on $1/\rho$. This is natural since the Riccati equation is a first-order differential equation. The specific volume v is given by

$$v = \frac{f'}{f} = \frac{c}{1 + cs^*} + \frac{[(3/2)d]^{1/3}\,[A\xi^{2/3} I_{-2/3}(\xi) + B\,\xi^{2/3} I_{2/3}(\xi)]}{(1 + cs^*)^2\,[A\xi^{1/3} I_{1/3}(\xi) + B\xi^{1/3} I_{-1/3}(\xi)]}$$

For $s^* = 0$, $v = 1.57744 = a_0$. Thus we obtain for the initial condition

$$c + (3d)^{1/3}\,[\Gamma(2/3)/\Gamma(1/3)]\,(A/B) = a_0$$

or

$$A/B = -[(a_0 - c)\Gamma(1/3)]/[(3d)^{1/3}\Gamma(2/3)]$$

Replacing the constants by their numerical values we get

$$\frac{1}{\rho} = \frac{1.2304}{1 + 1.2304\,s^*} + \frac{2.4176[\xi^{2/3} I_{-2/3}(\xi) - 0.1963\xi^{2/3} I_{2/3}(\xi)]}{(1 + 1.2304\,s^*)^2\,[\xi^{1/3} I_{1/3}(\xi) - 0.1963\xi^{1/3} I_{-1/3}(\xi)]} \qquad (15)$$

where

$$\xi = [1.6118\,s^*/(1 + 1.2304\,s^*)]^{3/2}$$

The variable ξ becomes imaginary for supersonic values of the speed ($s^* < 0$). However the functions $\xi^{1/3} I_{\pm 1/3}(\xi)$ and $\xi^{2/3} I_{\pm 2/3}(\xi)$ are regular power series expansions in the argument $1.6118\,s^*/(1 + 1.2304\,s^*)$ which converge for any finite s^* (except $s^* = -1.2304$) and are continuous across the sonic point. For supersonic values of s^*, the functions $I_{\pm v}$ must be replaced by the Bessel functions $J_{\pm v}$. Letting $\tilde{\xi} = [-1.6118\,s^* \div (1 + 1.2304\,s^*)]^{3/2}$ the relation for $1/\rho$ in the supersonic range is

$$\frac{1}{\rho} = \frac{1.2304}{1 + 1.2304\,s^*} + \frac{2.4176\,[\tilde{\xi}^{2/3} J_{-2/3}(\tilde{\xi}) - 0.1963\,\tilde{\xi}^{2/3} J_{2/3}(\xi)]}{(1 + 1.2304\,s^*)^2\,[-\tilde{\xi}^{1/3} J_{1/3}(\tilde{\xi}) - 0.1963\,\tilde{\xi}^{1/3} J_{-1/3}(\tilde{\xi})]} \qquad (16)$$

We shall now compute the relation between s^* and the velocity magnitude q. Thus

$$\rho(dq/q) = -ds^*$$

$$dq/q = -(f'/f)\,ds^*$$

Finally

$$\left.\begin{aligned} q/q^* &= f(0)/f(s^*) \\ \text{or} \\ q &= \frac{-0.1667}{(1 + 1.2304\, s^*)\,[\xi^{1/2} I_{1/3}(\xi) - 0.1963 \xi^{1/2} I_{-1/3}(\xi)]} \end{aligned}\right\} \quad (17)$$

To obtain the pressure in terms of s^* from Eq. (13) we would have to integrate numerically. However, the series expansion of Eq. (14) is sufficiently good for the range of values that we shall use. Knowing the specific volume in terms of s^* we may also compute the Mach Number from the relation

$$\left.\begin{aligned} \frac{1 - M^2}{\rho^2} &= \frac{d}{ds^*}\left(\frac{1}{\rho}\right) + \frac{1}{\rho^2} = \frac{9.4204\, s^*}{(1 + 1.2304\, s^*)^5} \\ M^2 &= 1 - [9.4204\, s^* \rho^2/(1 + 1.2304\, s^*)^5] \end{aligned}\right\} \quad (18)$$

Thus the state quantities q, p, ρ, and M for our hypothetical gas are given by Eqs. (14)–(18) in terms of the variable s^*. The pressure-density relation represented by Eqs. (14)–(16) agrees closely with the adiabatic relation for $\gamma = 1.4$ in the range $M = 0.85$ to $M = 1.35$.

(IV) The Mapping to the Physical Plane

The mapping of the streamlines in the physical plane is affected by the integration of Eq. (2). Along the streamlines, $d\psi = 0$ and $d\theta/ds = -\psi_s/\psi_\theta$. Replacing the derivatives of φ by those of ψ from Eq. (4), we obtain the following relations for the mapping of the streamlines.

$$\left.\begin{aligned} (dz/ds)_{\psi = K} &= (\omega_1^2/q) e^{i\theta} [(\psi_s^2/\psi_\theta) + s\psi_\theta] \\ (dz/d\theta)_{\psi = K} &= -(\omega_1^2/q) e^{i\theta} [\psi_s + (s\psi_\theta^2/\psi_s)] \end{aligned}\right\} \quad (19)$$

The lines of constant velocity (s = constant) in the physical plane can be found by integrating

$$dz/d\theta = (1/q) e^{i\theta} \{-\omega_1^2 \psi_s + [(i/\rho)\psi_\theta]\} \quad (20)$$

Here we made use of Eq. (3) and the fact that $ds/ds^* = \omega_1^2$.

From Eqs. (19) we can obtain expressions for the curvature of the streamlines and velocity gradient along the streamlines. These are

$$\left.\begin{aligned} \left(\frac{d\theta}{dl}\right)_{\psi = K} &= \frac{q\psi_s}{\omega_1^2 \psi_\theta^2\,[(\psi_s/\psi_\theta)^2 + s]} \\ \left(\frac{dq}{dl}\right)_{\psi = K} &= -\frac{q^2}{\omega_1^4 \rho \psi_\theta [(\psi_s/\psi_\theta)^2 + s]} \end{aligned}\right\} \quad (21)$$

dl being the element of arc length along the streamlines. The inspection of the above equations reveals that discontinuities in the derivatives of the streamfunction with respect to the hodograph variables will introduce discontinuities in the curvature of the streamlines and in the acceleration of the fluid particles. These discontinuities are, of course, only admissible along the characteristics in the hodograph plane and therefore along the Mach lines in the physical plane.

(V) The Solutions of the Tricomi Equation Which Yield Transonic Flows Through a Nozzle

Some of the solutions of the Tricomi equations which we shall investigate are those given by Tricomi[8] in his famous paper on partial differential equations of mixed type. For the streamfunction we shall use

$$\psi = \frac{1}{\omega_1} r^{1 - (2\mu/3)} \left[F_1\left(\frac{r - \theta}{2r}\right) - F_1\left(\frac{r + \theta}{2r}\right)\right] \quad (22)$$

where $r = \sqrt{\theta^2 + (4s^3/9)}$, F_1 is the hypergeometric function $F_1(x) = F[(2\mu/3) - 1, (4/3) - (2\mu/3); 2/3; x]$, and μ is an arbitrary parameter. For r real, the line $\theta = 0$ in the hodograph plane is the straight streamline $\psi = 0$, and the streamfunction ψ is an odd function of θ and yields a flow that is symmetrical about the streamline $\psi = 0$. Since the hypergeometric function converges only when the absolute value of the variable is less than unity, we need the following analytic continuations.

$$\omega_1 \psi = r^{1 - (2\mu/3)} \left[-A(\mu) F_1\left(\frac{r - \theta}{2r}\right) + B(\mu) \left(\frac{\theta - r}{2r}\right)^{1/3} F_2\left(\frac{r - \theta}{2r}\right)\right]$$

where

$$\left.\begin{aligned} &|r - \theta| < 2|r| \\ A(\mu) &= \left\{\left[\Gamma\left(\frac{2}{3}\right)\Gamma\left(\frac{1}{3}\right)\right] \div \left[\Gamma\left(\frac{5 - 2\mu}{3}\right)\Gamma\left(\frac{2\mu - 2}{3}\right)\right]\right\} - 1 \\ B(\mu) &= \left[\Gamma\left(\frac{2}{3}\right)\Gamma\left(-\frac{1}{3}\right)\right] \div \left[\Gamma\left(\frac{2\mu - 3}{3}\right)\Gamma\left(\frac{4 - 2\mu}{3}\right)\right] \end{aligned}\right\} \quad (23)$$

and

$$F_2(x) = F\left(\frac{5 - 2\mu}{3}, \frac{2\mu - 2}{3}; \frac{4}{3}; x\right)$$

For $2|r| < |\theta - r|$,

$$\omega_1 \psi = -[A(\mu)E(\mu) - B(\mu)D(\mu)] r^{1 - (2\mu/3)} \times \left(\frac{2}{\theta - r}\right)^{(2\mu/3) - 1} F_3\left(\frac{2r}{r - \theta}\right) - [A(\mu)F(\mu) - B(\mu)\,C(\mu)] r^{1 - (2\mu/3)} \left(\frac{2r}{\theta - r}\right)^{(4 - 2\mu)/3} F_4\left(\frac{2r}{r - \theta}\right) \quad (24)$$

where

$$C(\mu) = \left[\Gamma\left(\frac{4}{3}\right)\Gamma\left(\frac{4\mu - 7}{3}\right)\right] \Big/ \left[\Gamma\left(\frac{2\mu - 2}{3}\right)\Gamma\left(\frac{2\mu - 1}{3}\right)\right]$$

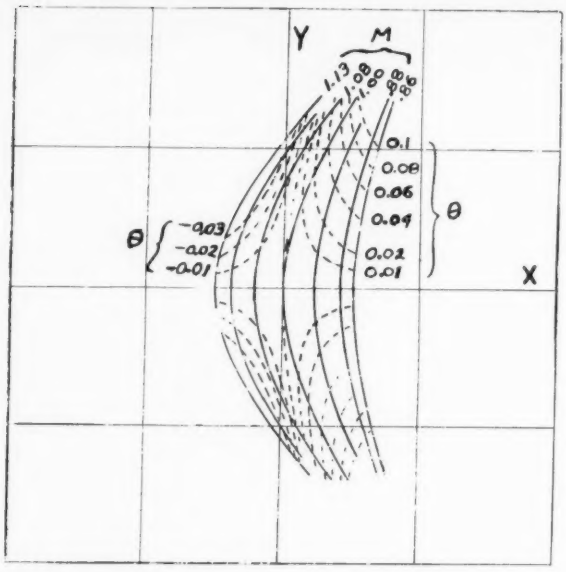

FIG. 1. Lines of constant Mach Number M and constant angle θ for $\mu = 1$.

$$D(\mu) = \left[\Gamma\left(\frac{4}{3}\right)\Gamma\left(\frac{7-4\mu}{3}\right)\right]\Big/\left[\Gamma\left(\frac{5-2\mu}{3}\right)\Gamma\left(\frac{6-2\mu}{3}\right)\right]$$

$$E(\mu) = \left[\Gamma\left(\frac{2}{3}\right)\Gamma\left(\frac{7-4\mu}{3}\right)\right]\Big/\left[\Gamma\left(\frac{4-2\mu}{3}\right)\Gamma\left(\frac{5-2\mu}{3}\right)\right]$$

$$F(\mu) = \left[\Gamma\left(\frac{2}{3}\right)\Gamma\left(\frac{4\mu-7}{3}\right)\right]\Big/\left[\Gamma\left(\frac{2\mu-3}{3}\right)\Gamma\left(\frac{2\mu-2}{3}\right)\right]$$

and

$$F_3(x) = F\left(\frac{2\mu-2}{3}, \frac{2\mu-3}{3}; \frac{4\mu-4}{3}; x\right)$$

$$F_4(x) = F\left(\frac{5-2\mu}{3}, \frac{4-2\mu}{3}; \frac{10\mu-4\mu}{3}; x\right)$$

The essential triple valued property is apparent from Eqs. (23). If the line $\theta = 0$ for r imaginary is approached on the correct branch of $[(\theta - r)/2r]^{1/3}$, the streamfunction vanishes, and we obtain the analytic continuation of the straight streamline into the supersonic region, $s < 0$. On other branches, we obtain streamlines which cut the $\theta = 0$ axis in the hodograph plane for $s < 0$.

For values of $\mu \geq 3/2$, we shall use the following solutions found by the author instead of those given above.

$$\omega_1\psi = \theta s^{-\mu} F\left(\frac{1+\mu}{3}, \frac{\mu}{3}; 3/2; -\frac{9\theta^2}{4s^3}\right) \qquad (25)$$

The singularity for $(\psi_\theta)_{\psi=0}$ at $s = 0$ is the same as the solutions in Eq. (22). The reason for this choice will be apparent later in the discussion.

Let us now investigate the nature of the mapping of the straight streamline in the neighborhood of the critical velocity. From Eq. (19) we have, since $\psi_s = 0$ for $\psi = 0$,

$$(dx/ds)_{\psi=0} = (\omega_1^2/q)s\psi_\theta$$

Now the solutions in Eqs. (23) and (25) have the singularity

$$(\psi_\theta)_{\psi=0} \propto s^{-\mu}$$

Thus

$$(dx/ds)_{\psi=0} \propto s^{1-\mu}$$

If $\mu < 2$, the sonic point $s = 0$ maps into some definite point in the physical plane. If $\mu < 1$, then

$$\left(\frac{dq}{dx}\right)_{\psi=0} = \frac{dq}{ds}\frac{ds}{dx} \propto s^{\mu-1} \to \infty \text{ as } s \to 0$$

We obtain infinite acceleration, and the solution yields a limiting line and cannot be continued into the supersonic domain. If $\mu \geq 2$, then the sonic point maps into $x = \infty$. Therefore, in order to obtain a transonic nozzle flow we must restrict μ to the range $1 \leq \mu < 2$. We shall see that we must further restrict μ to less than $7/4$ in order that ψ remain finite on two characteristics in the s, θ plane.

When s is set equal to 0 in Eq. (24), the streamfunction becomes

$$\psi = \frac{\theta^{-(2\mu/3)+1}}{1.4532}\left(1 - \left\{\left[\Gamma\left(\frac{2}{3}\right)\Gamma\left(\frac{1}{3}\right)\right] \div \left[\Gamma\left(\frac{5-2\mu}{3}\right)\Gamma\left(\frac{2\mu-2}{3}\right)\right]\right\}\right) \qquad (26)$$

For μ in the range 1 to $3/2$, the magnitude of ψ increases with increasing θ. For values of μ larger than $3/2$, $\psi \to \infty$ as $\theta \to 0$. In the ensuing discussion it will be shown that, when $1 \geq \mu < 3/2$, then the line of constant sonic velocity in the nozzle is concave to the incoming flow. The choice of μ equal to or greater than $3/2$ leads to flows where the sonic line is straight. It is apparent from Eq. (26) that when $\mu = 3/2$ the streamfunction reduces to the trivial solution $\psi \equiv 0$. However, $\mu = 3/2$ results in a definite nontrivial solution from Eq. (24).

(VI) Properties of the Flow for $\mu = 1$

When $\mu = 1$, the hypergeometric series in Eq. (11) can be summed, and, except for a multiplying constant, the streamfunction becomes

$$\psi = (1/\omega_1)\left[(r+\theta)^{1/3} - (r-\theta)^{1/3}\right] \qquad (27)$$

A section of this flow was computed by the author in reference 5. Most of the integration was performed numerically; however, the following parametric representation of the sonic line in the physical plane was obtained.

$$x = 0.964225\,\theta^{2/3}\{(3/2) + [(3/16)\theta^2] + [(1/112)\,\theta^4] + \ldots\} + \theta^{1/3}[-1.2509\,\theta + 0.2002\,\theta^3 - 0.0099\,\theta^5 + \ldots]$$

$$y = \theta^{1/3}[1.4981 - 0.6078\,\theta^2 + 0.0497\,\theta^4 + \ldots] + 0.964225\,\theta^{2/3}[(3\theta/5) - (\theta^3/22) + (\theta^5/680) - \ldots]$$

Similarly the velocity distribution on the straight streamline, $\psi = 0$, can be expressed by the following power series in s^*.

$$x_0 = 2.9372\,s^* - 3.1042\,s^{*2} + 3.1924\,s^{*3} - 2.0035\,s^{*4} - 2.5798\,s^{*5} + 14.0267\,s^{*6} + \ldots$$

Because of its simplicity, the solution of Eq. (27) is extremely practical for designing nozzles. The lines of constant velocity are easily computed by using Eq. (20). It can be shown by differentiating Eq. (27) that

$$\psi_s = -[(1/\omega_1)\,(d\omega_1/ds)\psi] - [(3/2)^{1/3}\omega_1\psi\,\psi_\theta]$$

With this substituted in Eq. (20), the coordinates of the lines s = constant are given by

$$z - x_0 = -\frac{i\omega_1}{q}\frac{dw_1}{ds}e^{i\theta}\psi + \left(\frac{3}{2}\right)^{1/3}\frac{\omega_1^3}{q}\int_0^\psi e^{i\theta}\,\psi\,d\psi + \frac{i}{q}\left(\omega_1\frac{d\omega_1}{ds} + \frac{1}{\rho}\right)\int_0^\psi e^{i\theta}\,d\psi$$

The results of some computations of the lines of constant velocity are shown in Fig. 1.

The streamfunction inside the region $(4/9)\,(-s)^3 > \theta^2$ of the hodograph plane is triple valued, because the quantity r becomes pure imaginary. In this region Eq. (27) can be written

$$\psi = \frac{2}{\omega_1}\left(\frac{2}{3}\right)^{1/3} \times (-s)^{1/2}\cos\left(\frac{\delta}{3} + \frac{2\pi n}{3}\right), \quad n = 0, 1, 2$$

where

$$\delta = \tan^{-1}\frac{\sqrt{(4/9)\,(-s)^3 - \theta^2}}{\theta} = \cos^{-1}\frac{\theta}{(4/9)\,(-s)^3}$$

A number of the streamlines are plotted in a small section of the hodograph plane in Fig. 2. A positive streamline first cuts the line $(2/3)\,(-s)^{3/2} = \theta$, then crosses the axis $\theta = 0$ and becomes tangent to the characteristic $(2/3)\,(-s)^{3/2} = -\theta$. Thus this latter characteristic is the envelope of the streamlines $\psi = K$, K being an arbitrary positive constant; and along this characteristic the Jacobian $J = [\partial(x, y)]/[\partial(s, \theta)]$ becomes infinite. The segments of the positive streamlines cut off by the characteristics are mapped into the triangular shaped region COA in Fig. 3 containing the line $\theta = 0$ for y positive. The segments of the positive streamlines beyond the envelope are mapped in the region downstream (negative x direction) of the curve $J = \infty$ for y positive. In a similar manner, the negative streamlines $\psi = -K$ cut the characteristic $(2/3)\,(-s)^{3/2} = -\theta$ and form an envelope at the characteristic $(2/3)\,(-2)^{3/2} = \theta$. The segments of the streamlines between the characteristics are mapped into the region between the Mach line COC′ and the line $J = \infty$, AOA,′ in Fig. 3, while the streamlines beyond the envelope are mapped into the region downstream of the curve $J = \infty$. This flow has the property that the fluid particles are always accelerated along the streamline; and the curvature of the streamlines are continuous, finite, and nonzero (except for the center streamline).

(VII) Nozzle Flow with a Discontinuity in the Curvature of the Wall

It is possible with the addition of a solution that vanishes on the first characteristic to obtain a channel in which the curvature of the streamlines and the velocity gradients are discontinuous along the first characteristic COC′ in Fig. 3. In the region outside the cusp of the characteristics $\theta = \pm(2/3)\,(-s)^{3/2}$, the streamfunction is defined by the equation

$$\psi = (1/\omega_1)\,[(\theta + r)^{1/3} + (\theta - r)^{1/3}],\ r = \sqrt{(4/9)s^3 + \theta^2}$$

For those segments of the streamlines which terminate on both characteristics, we use

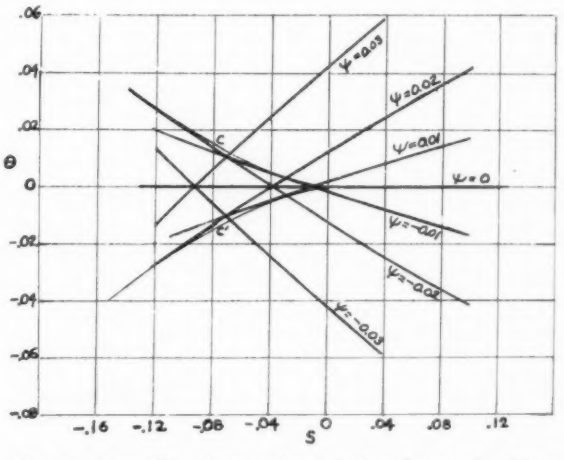

Fig. 2. Streamlines in the hodograph plane for $\mu = 1$. Lines C and C′ denote the characteristics, $\theta = (2/3)\,(-s)^{3/2}$ and $\theta = -(2/3)\,(-s)^{3/2}$, respectively.

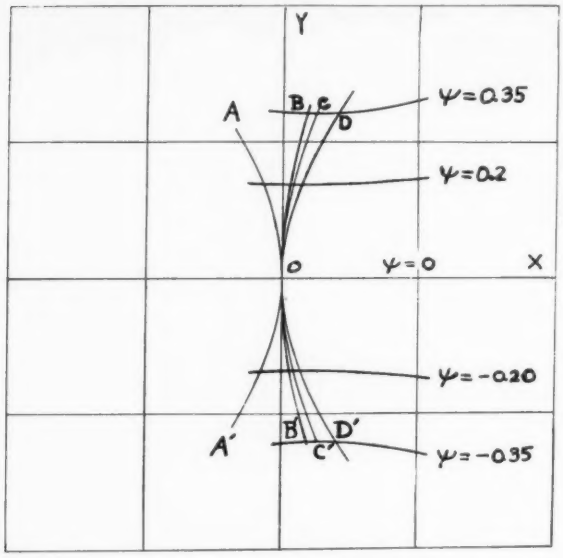

FIG. 3. Streamlines in the physical plane for $\mu = 1$. The other lines are as follows: DOD′, sonic line; COC′, Mach line; BOB′, line of angle $\theta = 0$; AOA′, Mach line on which Jacobian is infinite.

$$\psi = (1/\omega_1)\ \text{Real}\ [(\theta + i\alpha)^{1/3} + (\theta - i\alpha)^{1/3}] + Im\{c/\omega_1[(\theta + i\alpha)^{1/3} - (\theta - i\alpha)^{1/3}]\}$$

where $\alpha = \sqrt{(4/9)\ (-s)^3 - \theta^2}$. The second term vanishes when α goes to zero, so that the streamfunction is continuous along the characteristic $\theta = (2/3)\ (-s)^{3/2}$. The curvature of all streamlines in the physical plane are discontinuous where they cut this first characteristic since the derivatives with respect to θ and s are discontinuous. The streamlines in this region may be expressed more simply in the form

$$\psi = (2/\omega_1)\ (2/3)^{1/3}(-s)^{1/2}\sqrt{1 + c^2}\cos\ [(\delta/3) - \nu]$$

where $\delta = \cos^{-1}\{\theta/[(2/3)\ (-s)^{3/2}]\}$ and $\nu = \tan^{-1} c$. The angle δ varies from 0 to π for positive values of the streamfunction. On the second characteristic, we have $\delta = \pi$ and $\theta = -(2/3)\ (-s)^{3/2}$. Thus the equation above reduces to

$$\psi = \frac{2}{\omega_1}\left(\frac{2}{3}\right)^{1/3}(-s)^{1/2}\sqrt{1 + c^2}\cos\left(\frac{\pi}{3} - \nu\right) = \frac{1}{\omega_1}\left(\frac{2}{3}\right)^{1/3}(-s)^{1/2}\ (1 + \sqrt{3}\ c)$$

In order that the streamfunction be continuous on the second characteristic, the extension of the positive streamlines beyond the point of the tangency on the second characteristic must be defined by

$$\psi = \frac{2(1 + \sqrt{3}\ c)}{\omega_1}\left(\frac{2}{3}\right)^{1/3}(-s)^{1/2}\cos\delta/3$$

where δ ranges from π to $3\pi/2$. The streamline pattern in the hodograph plane is shown in Fig. 4. The flow in the physical plane is similar to that in Fig. 3 except that curvature of the streamlines and the velocity gradient are discontinuous along the characteristic COC′.

The quantity C must be restricted by the condition that the Jacobian $J = (\omega_1^2/\rho q^2)\ (s\psi_\theta^2 + \psi_s^2)$ have the same sign in the region outside the cusp of the characteristics as in the region where the streamline segments touch both characteristics. Now

$$\psi_\theta = -\frac{2}{3\omega_1}\left(\frac{2}{3}\right)(-s)^{1/2}\sqrt{1 + c^2}\sin\left(\frac{\delta}{3} + \nu\right)\frac{\partial\delta}{\partial\theta}$$

$$\psi_s = \left(-\frac{a}{\omega_1} + \frac{1}{2s}\right)\psi - \frac{2}{3\omega_1}\left(\frac{2}{3}\right)(-s)^{1/2}\sqrt{1 + c^2}\sin\left(\frac{\delta}{3} + \nu\right)\frac{\partial\delta}{\partial s}$$

and with

$$\partial\delta/\partial\theta = -1/\alpha$$

$$\frac{\psi_s}{\psi_\theta} = 3\left(-\frac{a}{\omega_1} + \frac{1}{2s}\right)\cot\left(\frac{\delta}{3} + \nu\right)\alpha + \left(\frac{d\theta}{ds}\right)_{\delta\ =\ \text{constant}}$$

On the first characteristic $(d\theta/ds)_{\delta\ =\ \text{constant}} = -(-s)^{1/2}$, and the Jacobian becomes

$$J = \frac{\omega_1^2}{\rho q^2}\psi_\theta^2\left[\left(\frac{\psi_s}{\psi_\theta}\right)^2 + s\right] = (\text{positive function of } s)\ \frac{\cot\nu}{\alpha} + 0(1) > 0$$

In order that J go to plus infinity as α goes to zero, we require that $\cot\nu > 0$ which is equivalent to $c > 0$. On the second characteristic $(d\theta/ds)_{s\ =\ \text{constant}} = (-s)^{1/2}$, and

$$J = (\text{positive function of } s) \times \{-\cot\ [(\pi/3) + \nu]/\alpha\} > 0$$

This requires that $\cot\ [(\pi/3) + \nu] < 0$, which is equivalent to $c < \sqrt{3}$. Combining the two inequalities, we see that

$$0 < c < \sqrt{3}$$

in order that J be positive in the region between the two characteristics.

Let us investigate the effect of these limits for c on the discontinuity at the sonic point along the center streamline. For $\psi = 0$, we have

$$dx/ds = (s\omega_1^2/q)\ (\psi_\theta)_{\psi\ =\ 0}$$

In the subsonic region

$$(\psi_\theta)_{\psi\ =\ 0} = (2/3)^{1/3}\ (1/\omega_1 s)$$

and in the supersonic region

$$(\psi_\theta)_{\psi\ =\ 0} = (2/3)^{1/3}\ (1/\omega_1 s)\ (1 + \sqrt{3}\ C)$$

As $s \to +0$ we obtain $ds/dx = \{q^*/[\omega_1(0)]\}\ (3/2)^{1/3}$; and as $s \to -0$, $ds/dx = \{q^*/[\omega_1(0)]\}\ (3/2)^{1/3}\ [1/(1 + \sqrt{3}\ C)]$. By letting C take on the limits 0 and $\sqrt{3}$,

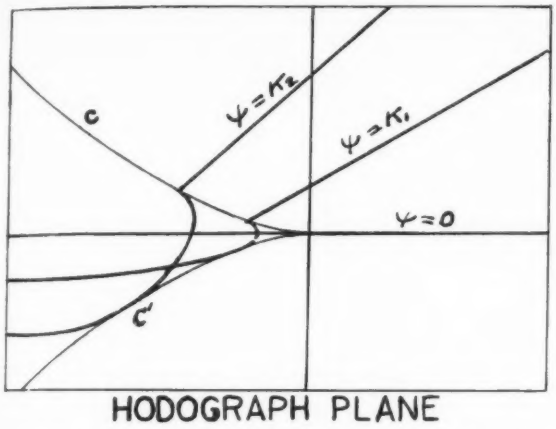

FIG. 4. Sketch of streamlines in the hodograph plane for flow having discontinuous curvature. $\mu = 1$. The streamlines in the physical plane are similar to Fig. 3. Streamline curvature is discontinuous on COC'.

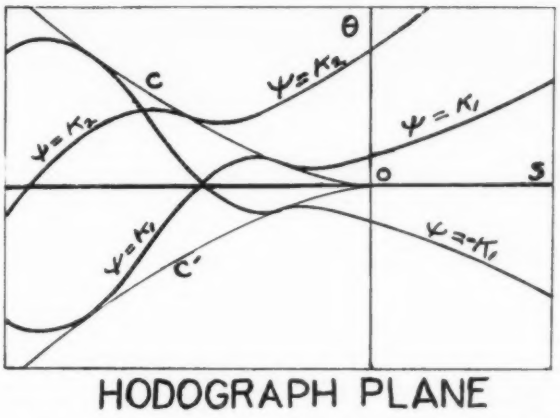

FIG. 5. Sketch of streamlines in the hodograph plane for $1 < \mu < 3/2$. Physical plane similar to Fig. 3 except curvature of sonic line DOD' is zero at O.

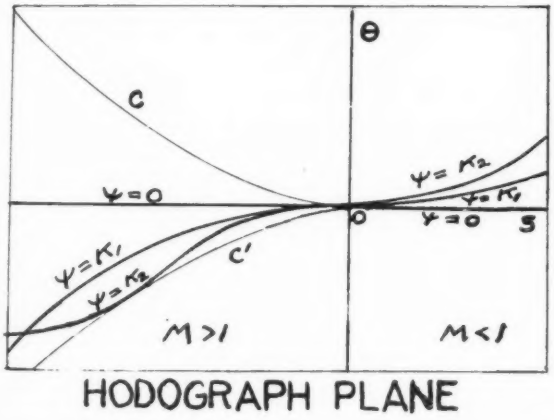

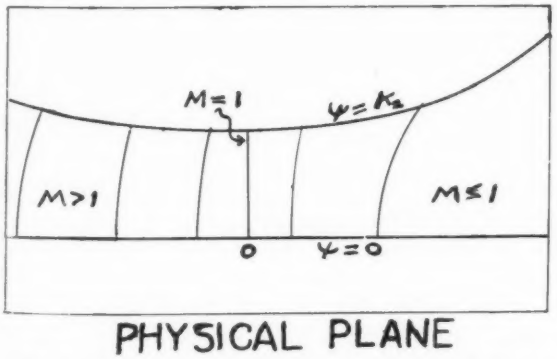

FIG. 6. Sketch of streamlines in the hodograph and physical planes for $3/2 < \mu < 7/4$. Accelerated flow. Straight sonic line is at O in physical plane. Other lines are constant velocity lines.

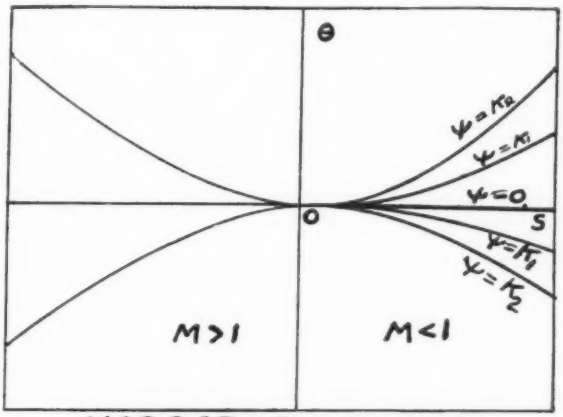

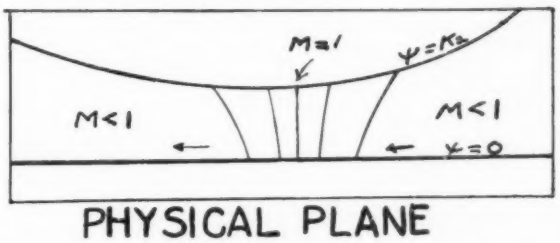

FIG. 7. Sketch of streamlines in the hodograph and physical planes for $3/2 < \mu < 7/4$. Accelerated-decelerated flow. Straight sonic line and lines of constant subsonic Mach Number are shown.

we obtain the inequalities

$$\left(\frac{ds}{dx}\right)_{s\to+0} \geq \left(\frac{ds}{dx}\right)_{s\to-0} > \frac{1}{4}\left(\frac{ds}{dx}\right)_{s\to+0}$$

The inequality may also be written

$$4\left|\frac{dq}{dx}\right|_{\text{supersonic}} > \left|\frac{dq}{dx}\right|_{\text{subsonic}} \geq \left|\frac{dq}{dx}\right|_{\text{supersonic}}$$

This is the same result obtained by Frankl using more general methods of analysis.

Falkovich[9] has solved the problem for discontinuous curvature along the first characteristic, but his method involves the solution of a complicated differential equation to match the conditions on the first characteristic.

(VIII) Properties of the Flow for Values of the Parameter $1 < \mu < 3/2$

The flow for $1 < \mu < 3/2$ has properties similar to the flow for $\mu = 1$. The streamlines in the hodograph plane have one notable difference: they are tangent to both the characteristics $\theta = \pm(2/3)\ (-s)^{3/2}$. To show this we shall first express Eq. (23) as a function of θ and t, where $t = 2r/(\theta - r)$. We obtain

$$\omega_1\psi = [t\,\theta/(2+t)]^{1-(2\mu/3)}\,[\alpha_1(\mu)t^{(2\mu/3)-1}\,F_3(-t) + \beta_1(\mu)t^{(4-2\mu)/3}\,F_4(-t)]$$

The quantities $\alpha_1(\mu)$ and $\beta_1(\mu)$ replace the more complicated expressions for the coefficients in Eq. (23). For $|t| < 1$, we have

$$\omega_1\psi = \theta^{1-(2\mu/3)}\,G(t)$$

where $G(t)$ takes the form

$$G(t) = \sum_{n=0}^{\infty} d_n t^n + \sum_{n=0}^{\infty} e_n t^{(7-4\mu)/3+n}$$

After some elementary manipulation, the slope of the streamline becomes

$$\frac{d\theta}{ds} = -\frac{\psi_s}{\psi_\theta} = -\frac{2}{3}\frac{s^2}{\theta^2}\left(\left[2 + 2t + \frac{t^2}{2} - \frac{\omega_1{}^1}{\omega_1}\cdot\frac{\theta t G(t)}{(2+t)G'(t)}\right]\Big/\left\{2 + 2t + \frac{[1-(2\mu/3)]tG(t)}{2+2tG'(t)}\right\}\right)$$

Here we have made use of the relations

$$\partial t/\partial\theta = \{[2(2+t)\,(1+t)]/\theta t\}$$

and

$$\partial t/\partial s = (1/3)\,(s^2/\theta^2)\,[(2+t^3)/t]$$

Now for small t,

$$[tG(t)]/[(2+t)G'(t)] = ct^{(4\mu/3)-(1/3)} + 0(t^{8(\mu-1)/3})$$

Thus

$$\left(\frac{d\theta}{ds}\right)_\psi = -\frac{2}{3}\frac{s^2}{\theta}\left\{1 - c\left[\frac{\omega_1{}^1}{\omega_1}\theta + \left(1 - \frac{2\mu}{3}\right)\right]t^{(4\mu/3)-(1/3)} + \cdots\right\}$$

Therefore, on the characteristic $\theta = (2/3)\ (-s)^{3/2}$, we find that

$$(d\theta/ds)_\psi = -(2/3)\ (s^2/\theta) = -(-s)^{1/2}$$

which is the same as $d\theta/ds$ for the characteristic $\theta = (2/3)\ (-s)^{3/2}$. It should be noted that the expression above is not valid for $\mu = 1$, for in this case $t^{(2/3)-(4\mu/3)} = t$ and $d_1 = -e_0$. Therefore the function $G(t)$ contains no power of t less than 2 (except for the term of order one). This can be seen by expanding Eq. (27) in powers of t. The first derivatives for $\mu = 1$ are all finite on the first characteristic. At the second characteristic, however, the derivatives do become infinite and the streamlines are tangent to the second characteristic (see Fig. 2).

The streamlines in the hodograph plane for the upper half of the nozzle are shown in Fig. 5 for $1 < \mu < 3/2$. In the upper left quadrant of the hodograph plane and the portion of the upper right quadrant bounded by the $s = 0$ axis and the curve $\theta - r = 2r$ or $\theta = (1/2)^{1/3}\ (-s)^{3/2}$ Eq. (23) is used to evaluate the streamfunction. For the region containing the characteristic for which $r = 0$, Eq. (24) is used for the streamfunction. Inside the two characteristics $\theta = \pm(2/3)\ (-s)^{3/2}$ the quantity r is imaginary; consequently, the real part of Eqs. (23) and (24) must be taken as the streamfunction. For the segments of the streamlines which touch both characteristics, the argument of r is equal to $\pi/2$ and the argument of $\theta - r$ varies from 0 on $\theta = (2/3)\ (-s)^{3/2}$ to $-\pi$ on the characteristic $\theta = -(2/3)\ (-s)^{3/2}$. On $\theta = 0$, the argument of $\theta - r$ is $-\pi/2$. For the segments of the streamlines beyond the second characteristic the argument of r is $3\pi/2$ and the argument of $(\theta - r)$ varies from $-\pi$ on the second characteristic to $-3\pi/2$ on the line $\theta = 0$. Eq. (23) is seen to vanish on $\theta = 0$ for the latter choice of arguments and therefore gives the correct branch of the streamfunction for the streamline $\psi = 0$. The Jacobian $J = \partial(x, y)/\partial(\theta, s)$ becomes infinite on both characteristics but only changes sign at the second characteristic.

We shall now investigate the properties of the flow due to the singular nature of the solution on the first characteristic. The curvature K of the streamlines is found by using Eq. (21). We obtain

$$K = \left|\frac{d\theta}{dl}\right| \approx \frac{(-s)^{1/2}q + 0[t^{(4\mu/3)-(1/3)}]}{2\omega_1{}^2|\psi_\theta||c|\ (-s)\ \{(\omega_1{}^1/\omega_1)\,\theta + [1-(2\mu/3)]\}\ t^{(4\mu/3)-(1/3)}}$$

Since $\omega_1\psi_\theta = 4e_0\theta^{-2\mu/3}t^{(1/3)-(4\mu/3)} + 0(t^{-1})$, we find that

$$K = 0(\theta^{(2\mu/3)-(1/3)})$$

for small θ on the characteristic $\theta = (2/3)(-s)^{3/2}$.

It is apparent that the curvature vanishes as θ goes to zero for values of $\mu > 1/2$. The velocity gradient along the streamline is found also by using Eq. (10). We obtain

$$\left|\frac{dq}{dl}\right| = \left|\frac{ds}{dz}\right| \left|\frac{dq}{ds}\right| \propto \theta^{(2\mu/3)-(2/3)}$$

on the characteristic $\theta = (2/3)(-s)^{3/2}$. Thus both the velocity gradient along each streamline and the streamline curvature vanish as we approach the axis of symmetry along the Mach line in the physical plane corresponding to $\theta = (2/3)(-s)^{3/2}$, when $\mu > 1$. (If $\mu = 1$, then the velocity gradient does not vanish.) The velocity gradient and curvature vary similarly along the second characteristic, $\theta = -(2/3)(-s)^{3/2}$.

The coordinates of the sonic line can be calculated from a series expansion that converges for all finite values of θ. Separating Eq. (20) into real and imaginary parts, we obtain

$$\left.\begin{aligned} \frac{dx}{d\theta} &= -\frac{\omega_1^2\psi_s}{q}\cos\theta - \frac{1}{\rho q}\psi_\theta \sin\theta \\ \frac{dy}{d\theta} &= -\frac{\omega_1^2\psi_s}{q}\sin\theta + \frac{1}{\rho q}\psi_\theta \cos\theta \end{aligned}\right\} \tag{28}$$

By differentiating Eq. (23) with respect to θ, we find that

$$\omega_1\psi_{\theta\theta} = -[1-(2\mu/3)]\, r^{-(2\mu/3)-1}\theta\,[AF_1(\chi) + B\chi^{1/3}F_2(\chi)] + r^{1-(2\mu/3)}\,[AF'(\chi) + (B/3)\chi^{-(2/3)}F_2(\chi) + B\chi^{1/3}F_2'(\chi)]\,[\chi(r+\theta)/r^2]$$

where

$$\chi = (r-\theta)/2r$$

When $s = 0$, then $\chi = 0$, and ψ_θ reduces to

$$\omega_1\psi_\theta = -[1-(2\mu/3)]A\theta^{-(2\mu/3)} \tag{29}$$

Similarly

$$\omega_1\psi_s = -\frac{\omega_1^1}{\omega_1}\psi - \frac{2}{3}\left(1-\frac{2\mu}{3}\right) r^{-(2\mu/3)-1}\, s^2\,[AF_1(\chi) + B\chi^{1/3}F_2(\chi)] - r^{1-(2\mu/3)}\left[AF_1'(\chi) + \frac{B}{3}\chi^{-(2/3)}F_2(\chi) + B\chi^{1/3}F_1'(\chi)\right]\frac{\theta S^2}{3r^3}$$

Now near $s = 0$ but $\theta \neq 0$,

$$\chi = [(r-\theta)/2r] = (1/2) - 1/[2\sqrt{1 + (4/9)(s^3/\theta^2)}]$$

$$\chi = [(1/9)(s^3/\theta^2)] + 0(s^6)$$

Therefore, for $s = 0$, we find that

$$\psi_s = [(\omega_1'/\omega_1^2)A\theta^{1-(2\mu/3)}] - [(B/3)(9)^{2/3}\theta^{(1-2\mu)/3}] \tag{30}$$

Substituting Eqs. (29) and (30) into Eq. (28) and integrating leads to

$$x = -\left(\frac{\omega_1'}{q^*}A\right)\theta^{2-(2\mu/3)}\sum_{n=0}^{\infty}\frac{3\theta^{2n}(-1)^n}{(6-2\mu+6n)(2n)!} + \frac{\omega_1}{q^*}B(9)^{3/3}\theta^{(4-2\mu)/3}\sum_{n=0}^{\infty}\frac{\theta^{2n}(-1)^n}{(4-2\mu+6n)(2n)!} + \left(1-\frac{2\mu}{3}\right)\left(\frac{1}{\omega_1\rho^*q^*}\right)A\theta^{1-(2\mu/3)}\sum_{n=0}^{\infty}\frac{3\theta^{2n-1}(-1)^n}{(9-2\mu+6n)(2n+1)!} \tag{31}$$

$$y = -\frac{\omega_1'}{q^*}A\theta^{2-(2\mu/3)}\sum_{n=0}^{\infty}\frac{3\theta^{2n+1}(-1)^n}{(9-2\mu+6n)(2n+1)!} + \left(\frac{\omega_1}{q^*}\right)B(9)^{2/3}\theta^{4-(2\mu/3)}\sum_{n=0}^{\infty}\frac{\theta^{2n+1}(-1)^n}{(7-2\mu+6n)(2n+1)!} - \left(1-\frac{2\mu}{3}\right)\left(\frac{1}{\omega_1\rho^*q^*}\right)A\theta^{1-(2\mu/3)}\sum_{n=0}^{\infty}\frac{3\theta^{2n}(-1)^n}{(3-2\mu+6n)(2n)!} \tag{32}$$

Now the slope of the sonic line near $\theta = 0$ is

$$\frac{dy}{dx} = \frac{dy}{d\theta}\Big/\frac{dx}{d\theta} = \left[-\left(1-\frac{2\mu}{3}\right)\left(\frac{1}{\omega_1\rho^*q^*}\right)A\theta^{-(2\mu/3)} + 0(\theta^{(4-2\mu)/3})\right]\Big/\left[\frac{\omega_1 B}{3q^*}(9)^{2/3}\theta^{(1-2\mu)/3} + 0(\theta^{1-(2\mu)/3})\right]$$

$$\frac{dy}{dx} = -\left\{[(3-2\mu)A]/[\omega_1(9)^{2/3}B]\right\}\theta^{-1/3} + O(\theta^{4/3})$$

Since $A < 0$, $B > 0$, and $1 < \mu < 3/2$, then the slope is positive for $\theta > 0$. From consideration of the lowest order term of Eq. (31) and of Eq. (32) we see that x and y increase with θ. The sonic line is then seen to be concave to the incoming flow which is in the negative x direction. Now the curvature of the sonic line near the origin is of the order of

$$\frac{d^2x}{dy^2}\Big/\sqrt{1+\left(\frac{dx}{dy}\right)^2} = \left[\frac{d}{d\theta}\left(\frac{dx}{dy}\right)\frac{d\theta}{dy}\right]\Big/\sqrt{1+\left(\frac{dx}{dy}\right)^2} = O(\theta^{-(2/3)+(2\mu/3)})$$

The curvature of the sonic line vanishes where it crosses the axis of symmetry of the nozzle for $\mu > 1$.

(IX) The Flow Through a Nozzle with Straight Sonic Line $3/2 \leq \mu < 7/4$

For values of μ greater than $3/2$, the solutions given in Eq. (23) could be used to construct flows through nozzles in which the sonic line is straight. However, we shall establish solutions that are more convenient. We shall assume the function ψ' can be expressed in the form

$$\psi' = \theta s^{-\mu} F[-(9/4)\ (\theta^2/s^3)]$$

If this expression is substituted into the Tricomi equation, the following differential equation results.

$$\eta(1-\eta)F'' + \left[\frac{3}{2} - \left(\frac{4}{3}+\frac{2\mu}{3}\right)\eta\right]F' - \frac{\mu(\mu+1)}{9}F = 0$$

where $\eta = -(9/4)\ (\theta^2/s^3)$. This is the hypergeometric equation whose solution is

$$F\left(\frac{1+\mu}{3}, \frac{\mu}{3}; \frac{3}{2}; -\frac{9}{4}\frac{\theta^2}{s^3}\right)$$

Unlike the solution given in Eq. (23), the value of $3/2$ for μ does not lead to a trivial solution but yields

$$\psi' = \frac{\theta}{s^{3/2}} F\left(\frac{5}{6}, \frac{1}{2}; \frac{3}{2}; -\frac{9}{4}\frac{\theta^2}{s^3}\right) \qquad (33)$$

This hypergeometric function can be summed; for, with

$$(9/4)\ [\theta^2/(-s)^3] = \xi^2$$

and

$$\Gamma\ [(3/2)+n] = [(1/2)+n]\Gamma[(1/2)+n]$$

we have

$$F\left(\frac{5}{6}, \frac{1}{2}; \frac{3}{2}; \xi^2\right) = \frac{1}{\xi}\sum_{n=0}^{\infty}\frac{\Gamma[(5/6)+n]\xi^{2n+1}}{\Gamma(5/6)(2n+1)n!}$$

The quantity on the right-hand side can be recognized as

$$F\left(\frac{5}{6}, \frac{1}{2}; \frac{3}{2}; \xi^2\right) = \frac{1}{\xi}\int_0^{\xi}(1-\xi^2)^{-(5/6)}\,d\xi$$

Finally, for the solution to the Tricomi equation we have

$$\psi' = \int_0^{3\theta/2(-s)^{3/2}} (1-\xi^2)^{-(5/6)}\,d\xi$$

after neglecting a constant multiplier. If the trigonometric substitution $\xi = \sin\phi$ is made we obtain

$$\psi' = \int_0^{\sin^{-1}[3\theta/2(-s)^{3/2}]} \sec^{2/3}\phi\ d\phi$$

For subsonic flow, $\xi = it$ where t is real. Then

$$\psi' = -\int_0^{3\theta/2(s)^{3/2}} (1+t^2)^{-5/6}\,dt = \int_0^{\tan^{-1}[3\theta/2(s)^{3/2}]} \sec^{1/3}\phi\ d\phi \qquad (34)$$

The negative sign is chosen in Eq. (34) so that the streamlines in the physical plane form a converging-diverging stream. For the supersonic region, the streamfunction may be expressed as an incomplete Beta function

$$\psi' = -2^{-(2/3)}B_x(1/6, 1/6)$$

where

$$x = \frac{1}{2} - \frac{3\theta}{4(-s)^{3/2}}$$

$$B_x(p, q) = \int_0^x x^{p-1}\ (1-x)^{q-1}\,dx$$

For values of μ other than $3/2$, the quantity $s^{-\mu}$ becomes complex on passing into the supersonic region. For s negative and $\eta < 1$ we choose the branch

$$\psi' = \theta(-s)^{-\mu}\cos n\ \mu\pi\ F(\eta) \qquad (35)$$

where n is an odd integer such that $\cos n\mu\pi$ is negative. With this choice we obtain the hodograph pattern shown in Fig. 6. This represents a nozzle in which the velocity is accelerated to supersonic velocities. If we choose another branch for the transition from the sonic point back into the subsonic region we obtain the pattern shown in Fig. 7 where the lower branch is obtained from

$$\psi' = \theta s^{-\mu}\cos 2n\ \mu\pi F(\eta) \qquad (36)$$

where n is an integer such that $\cos 2n\mu\pi < 0$. This gives a channel that has a subsonic exhaust and in

which the sonic velocity is attained on a line across the throat of the channel.

The origin in the hodograph plane is a branch point of the streamfunction. Approaching the origin along the different lines in the hodograph plane we obtain different values of ψ. To illustrate the point, we write the streamfunction as

$$\psi = (s^{-\mu+(3/2)}/\omega_1)\ (-\eta)^{1/2}\ F(\eta)$$

For $\mu > 3/2$, η goes to 0, and $s^{-\mu+(3/2)}$ goes to infinity as θ and s go to zero, so that ψ remains finite. Thus near the origin the streamline $\psi = K$ is the path

$$(1/\omega_1)s^{-\mu+(3/2)}\ (-\eta)^{1/2} = [3\theta\ s^{-\mu}]/[2\ \omega_1(0)\,] = K + 0(s^{2\mu-3})$$

For $s < 0$, the streamfunction

$$\psi = \frac{1}{\omega_1}\int_0^{3\theta/2(-s)^{3/2}} (1 - \xi^2)^{-5/6}\, d\xi \qquad (37)$$

becomes tangent to the characteristic, $(3/2)\ [\theta/(-s)^{3/2}] = 1$. The streamfunction may be continued in two ways. In the region outside this characteristic the integrand becomes complex. The streamfunction in this region becomes

$$\psi = \frac{1}{\omega_1}\int_0^1 (1 - \xi^2)^{-5/6}\, d\xi + \frac{\cos\,[(5\pi/6)\ (2n + 1)]}{\omega_1}\int_1^{3\theta/2(-s)^{3/2}} (\xi^2 - 1)d\xi$$

$$\psi = \frac{1}{\omega_1}\,\psi'(1) + \frac{\cos\,[(\pi/3)\ (n - 5/2)]}{\omega_1}\int_1^{3\theta/2(-s)^{3/2}} (\xi^2 - 1)^{-5/6}\, d\xi$$

This streamfunction has two branches. For $n = 1$, the cosine vanishes. For $n = 0$, $\cos\,[(\pi/3)\ (n - 5/2)] < 0$ and the flow continues expanding. For $n = 2$, $\cos\,[(\pi/3)\ (n - 5/2)] > 0$ and the flow is decelerated, giving a combination nozzle and supersonic diffusor with a second throat. If the streamlines are continued back into the region $3\theta/[2(-s)^{3/2}] < 1$, the streamfunction becomes

$$\psi = \frac{1}{\omega_1}\,\psi'(1) + \cos\frac{n\pi}{3}\int_{3\theta/2(-s)^{3/2}}^1 (1 - \xi^2)^{-5/6}\, d\xi$$

For $n = 3$ we obtain the orginal streamfunction, which vanishes for $\theta = 0$. For $n = 2$ we obtain $\cos\,(2\pi/3)$, which is negative, giving a nozzle and diffusor combination. For $n = 0$, we obtain the expanding flow, although, less expanding than that with $n = 2$ for the continuation into $3\,\theta/2(-s)^{3/2} > 1$.

For values of μ other than $3/2$, the analytic continuation of the hypergeometric function into the region around the characteristic $3\theta/2(-s)^{3/2} = 1$ is given by

$$F\left(\frac{1+\mu}{3},\ \frac{\mu}{3};\ \frac{3}{2};\ -\frac{9\theta^2}{4s^3}\right) = \left\{\left[\Gamma\left(\frac{3}{2}\right)\Gamma\left(\frac{7}{6} - \frac{2\mu}{3}\right)\right] \div \left[\Gamma\left(\frac{7}{6} - \frac{\mu}{3}\right)\Gamma\left(\frac{3}{2} - \frac{\mu}{3}\right)\right]\right\} \times F\left(\frac{1+\mu}{3},\ \frac{\mu}{3};\ \frac{1}{6} + \frac{2\mu}{3};\ 1 + \frac{9}{4}\frac{\theta^2}{s^3}\right) + \left\{\left[\Gamma\left(\frac{3}{2}\right)\Gamma\left(\frac{2\mu}{3} - \frac{7}{6}\right)\right] \Big/ \left[\Gamma\left(\frac{1+\mu}{3}\right)\Gamma\left(\frac{\mu}{3}\right)\right]\right\} \times \left(1 + \frac{9}{4}\frac{\theta^2}{s^3}\right)^{(7/6)-(2\mu/3)} F\left(\frac{7}{6} - \frac{\mu}{3},\ \frac{3}{2} - \frac{\mu}{3};\ \frac{13}{6} - \frac{2\mu}{3};\ 1 + \frac{9\theta^2}{4s^3}\right)$$

In order that ψ be finite on the characteristic, we see that $\mu < 7/4$. Since $(7/6) - (2\mu/3) < 1$, the derivative of $\{1 + [(9/4)\ (\theta^2/s^3)]\}^{(7/6)-2\mu/(3)}$ becomes infinite on the characteristic, and the streamlines are tangent to the characteristics $1 + [(9/4)\ (\theta^2/s^3)] = 0$.

(X) Properties of the Flow

The physical coordinates of the flow may be found by integrating Eqs. (8) and (9) with the streamfunctions given above. However, it may be more convenient to express Eq. (2) in terms of ψ and φ' by using Eq. (5). This yields

$$dz = -[(\omega_1/q)e^{i\theta}d\varphi'] + [(\omega_1\omega_1'/q)e^{i\theta}\psi d\theta] + [(id\psi/\rho)e^{i\theta}] \qquad (37)$$

To find φ' we note that, by Eq. (6),

$$\psi_s' = -\theta s^{-\mu-1}\ (\mu F + 3\eta F') = \varphi_\theta'$$

or

$$\varphi_\theta' = (2/9)s^{-\mu+2}\ (\mu F + 3\eta F')\ (\partial\eta/\partial\theta)$$

Integrating we obtain

$$\varphi' = s^{-\mu+2}\left\{\left[F\left(\frac{\mu-2}{3},\ \frac{\mu-3}{3};\ 1/2;\ \eta\right)\right]\Big/(\mu - 2)\right\} + \frac{2}{3}\,\eta\,F\left(\frac{\mu+1}{3},\ \frac{\mu}{3};\ \frac{3}{2};\ \eta\right)$$

Following a similar procedure for $\mu = 3/2$, we have

$$\psi_s' = \frac{9}{4}\,\frac{\theta}{(-s)^{5/2}}\,(1 - \eta)^{-(5/6)}$$

$$\varphi_\theta' = \frac{1}{2}\,(-s)^{1/2}\,(1 - \eta)^{-5/6}\,\frac{\partial\eta}{\partial\theta}$$

and finally,

$$\varphi' = -3(-s)^{1/2}\,(1 - \eta)^{1/6}$$

We note that φ' is identically zero on the sonic line of the physical plane. Thus, since $s = 0$, $\theta = 0$ on the

sonic line in the physical plane, then $d\theta = 0$ and $d\varphi' = 0$; and consequently, Eq. (37) reduces to

$$(dz)_{s=0} = (id\psi)/\rho^*$$

Thus the sonic line is straight and the streamline ψ_K, say, cuts it at

$$x = 0$$

$$y = \psi_K/\rho^*$$

The streamlines then can be constructed by integrating Eq. (37) numerically from the sonic line with $\psi = \psi_K$ a constant and with the values of θ, s, q, ρ, and φ' determined by $\psi(\theta, s) = \psi_K$.

Let us investigate the curvature of the streamlines where they cut the vertical sonic line. To use Eq. (21) for the curvature, we need the slope of the streamlines at $s = 0$—namely,

$$\left(\frac{d\theta}{ds}\right)_\psi = -\frac{\psi_s}{\psi_\theta} = \frac{\theta s^{-\mu-1}(\mu F + 3\eta F') + \omega_1'\theta s^{-\mu} F(\eta)}{s^{-\mu}(F + 2\eta F')}$$

To approach the streamline ψ_K at the origin, we must let θ and s go to zero along the path $\theta = Ks^\mu$ for $\mu > 3/2$, K being a constant. We find by Eq. (21) and the relation above for $d\theta/ds$ that

$$\left(\frac{d\theta}{dl}\right)_{\varphi=\psi_K} = 0(s^{\mu-1}) \to 0 \quad \text{as } s \to 0$$

Thus the streamlines have zero curvature where they intersect the sonic line.

In a similar way, it can be shown that the acceleration of the fluid vanishes at the sonic line. From Eq. (19) we have

$$\left|\frac{ds}{dl}\right| = \frac{dq}{dl}\frac{ds}{dq} = \frac{q}{\omega_1^2}\left\{1/\psi_\theta[(d\theta/ds)_\psi^2 + s]\right\}$$

Therefore the acceleration of the fluid along a streamline at the sonic line is

$$\lim_{s\to 0}\frac{dq}{dt} = \lim_{\eta\to 0}\frac{dq}{dl}\frac{dl}{dt} = \lim_{\eta\to 0} q\frac{dq}{dl} = \lim_{s\to 0} 0(s^{\mu-1}) = 0$$

and

$$\frac{dq}{dt} \to 0 \quad \text{as } s \to 0$$

Here, the limit was taken along the path $\theta = Ks^\mu$ as in the foregoing explanation.

It is of some interest to find the curvature of the line of constant velocity where they cross the axis of the nozzle. For this purpose, it is convenient to expand ψ in powers of θ. Thus,

$$\psi = \frac{\theta}{\omega_1 s^\mu} - \frac{\mu(\mu+1)}{6\omega_1 s^{\mu+3}}\theta^3 + 0(\theta^5)$$

Differentiating with respect to θ and s, we obtain for the two derivatives

$$\psi_\theta = \frac{1}{\omega_1 s^\mu} - \frac{\mu(\mu+1)}{2\omega_1 s^{\mu+3}}\theta^2 + \ldots$$

$$\psi_s = \left(-\frac{\mu}{\omega_1 s^{\mu+1}} - \frac{1}{\omega_1^2}\frac{1}{s^\mu}\frac{d\omega_1}{ds}\right)\theta + 0(\theta^3)$$

Now the sign of the curvature at the axis of the constant velocity lines is given by the sign of $d^2x/dy^2 = [(d/d\theta)(dx/dy)](d\theta/dy)$. From Eq. (28),

$$\left.\begin{aligned}\frac{dx}{dy} &= \left(\frac{dx}{d\theta}\right)\Big/\left(\frac{dy}{d\theta}\right) = \frac{\rho\omega_1^2\psi_s\cos\theta + \psi_\theta\sin\theta}{\rho\omega_1^2\psi_s\sin\theta - \psi_\theta\cos\theta}\\ \frac{dx}{dy} &= \frac{[\rho\omega_1^2(d\theta/ds)_\psi] - \tan\theta}{[\rho\omega_1^2(d\theta/ds)_\psi]\tan\theta + 1}\end{aligned}\right\} \quad (38)$$

Using

$$\left(\frac{d\theta}{ds}\right)_\psi = -\left(\frac{\psi_s}{\psi_\theta}\right) = \left[\mu s^{-1} + \frac{1}{\omega_1}\frac{d\omega_1}{ds}\right]\theta + 0(\theta^3)$$

differentiating dy/dx with respect to θ and dividing by

$$\frac{dy}{d\theta} = -\frac{\omega_1^2\psi_s\sin\theta}{q} + \frac{\psi\theta}{\rho q}\cos\theta$$

$$= (1/\rho q\omega_1 s^\mu) + 0(\theta)$$

we obtain

$$\left(\frac{d^2x}{dy^2}\right)_{\theta=0} = \rho q\omega_1 s^\mu\left(\frac{\rho\mu\omega_1^2}{s} + \omega_1\rho\frac{d\omega_1}{ds} - 1\right) \geq 0$$

for $s \geq 0$. Since the flow is in the negative x direction, the lines of constant velocity at the axis are concave to the incoming flow. This concavity disappears as we approach the sonic point $s = 0$ if $\mu > 1$.

Using a similar analysis for $s < 0$, we obtain

$$\frac{d^2x}{dy^2} = -\rho q\omega_1(-s)^\mu \times \left[\rho\omega_1^2\frac{\mu}{(-s)} - \rho\omega_1\frac{d\omega_1}{ds} + 1\right]\cos n\mu \geq 0$$

Thus the streamlines are concave to the incoming flow in the supersonic region as well as the subsonic (see Fig. 7).

(XI) Construction of Perfect Nozzles by Means of the Hodograph Method

In the preceding pages, we have investigated solutions of the Tricomi equation having the required singularities to represent the transonic flow region of a Laval nozzle. In addition to one of the fundamental solutions discussed previously, we may also add other solutions that are regular in the region of the s, θ plane in which we are interested. If we wish to design an inlet that starts from a uniform parallel subsonic flow, then we must introduce a function with an arctangent singularity at some point s_0, θ_0 in the hodograph plane, representing the angle and velocity of flow at infinity.

A development of such a function is sketched briefly by Carrier and Ehlers. However, a more usable form was obtained by Falkovich[9] which we shall derive simply. By the substitution

$$t = (2/3)s^{3/2}$$

the Tricomi equation transforms to

$$\psi_{tt}' + \psi_{\theta\theta}' + [(1/3t)\psi_t'] = 0$$

Falkovich introduced the orthogonal transformation

$$[(\theta + it) + it_0]/[(\theta + it) - it_0] = e^{\alpha+i\beta}$$

Since this is the bilinear transformation, the lines α = constant and β = constant are circles in the (t, θ) plane. Under this transformation the differential equation becomes

$$\psi_{\alpha\alpha}' + \psi_{\beta\beta}' + \frac{1}{3 \sinh \alpha (\cosh \alpha + \cos \beta)} \times \left[(1 + \cosh \alpha \cos \beta) \frac{\partial \psi'}{\partial \alpha} + \sinh \alpha \sin \beta \frac{\partial \psi'}{\partial \beta}\right] = 0$$

Since we desire a solution with an arctangent singularity, we assume a solution of the form

$$\psi' = (\cosh \alpha + \cos \beta)^{1/6} \beta \chi(\alpha)$$

With the further substitution that $\cosh \alpha = \tau$, the differential equation for χ reduces to the hypergeometric equation

$$\tau(1 - \tau) \frac{d^2\chi}{d\tau^2} + \left(\frac{1}{2} - \frac{7}{6}\tau\right)\frac{d\chi}{d\tau} - \frac{1}{144}\chi = 0$$

whose solutions are

$$F\left(\frac{1}{12}, \frac{1}{12}; \frac{1}{2}; \tau\right) \quad , \quad \tau^{-(1/2)} F\left(\frac{1}{12}, \frac{7}{12}; 1; \frac{1}{\tau}\right)$$

Thus with τ and β replaced by their equivalent relations in terms of s, θ, and s_0, we obtain for the streamfunction, using the second solution of χ,

$$\psi = \frac{1}{\omega_1}\left\{\left(\frac{4}{3} s_0^{3/2}\right) \Big/ \left[\theta^2 + \frac{4}{9}(s^3 + s_0^3)\right]\right\}^{1/6} \times F\left(\frac{1}{12}, \frac{7}{12}; 1; \left\{\left[\theta^2 + \frac{4}{9}(s^{3/2} - s_0^{3/2})\right]^2 \div \left(\theta^2 + \frac{4}{9}s^3 + \frac{4}{9}s_0^3\right)^2\right\}\right) \times \tan^{-1}\left[\frac{4 s_0^{3/2}\theta/3}{\theta^2 + 4(s^3 - s_0^3)/9}\right] \quad (39)$$

By the proper choice of the branch of the above many-valued function, it is possible to make all the streamlines in the hodograph plane converge to the point $\theta = 0$, $s = s_0$ and thereby prescribe a uniform flow at ∞ with a velocity given by s_0 with zero angle of inclination. Thus the nature of our channel may be changed by varying our choice of s_0.

In addition to the two singular hodograph solutions, we may consider solutions that are regular. We must require, however, that $\psi = 0$ for $\theta = 0$ and that ψ be an odd function of θ in order to obtain a symmetrical channel with a straight axis. Some possible solutions are those obtained by separation of variables—namely,

$$\left.\begin{aligned}
\psi_1 &= \frac{1}{\omega_1} s^{1/2} J_{\pm(1/3)}\left(\frac{2}{3}\alpha s^{3/2}\right) \sinh \alpha\theta \\
\psi_2 &= \frac{1}{\omega_1} s^{1/2} K_{\pm(1/3)}\left(\frac{2}{3}\alpha s^{3/2}\right) \sin \alpha\theta \\
\psi_3 &= \theta/\omega_1 \\
\psi_4 &= \theta s/\omega_1
\end{aligned}\right\} \quad (40)$$

These six solutions are analytic everywhere in the s, θ plane. We may also construct a family of solutions of the Tricomi equations by noting that, if ψ_1' is a solution, then $\psi_2' = -\int \psi_1' d\theta$ is a solution if we add an appropriate function of s. Starting with $\psi' = \theta$ and $\psi' = \theta s$, we obtain the following family of solutions by integrating with respect to θ and adding a term in s whenever necessary.

$$\left.\begin{aligned}
\psi_1' &= \theta \\
\psi_2' &= \theta^2 - [(1/3)s^3] \\
\psi_3' &= s^3\theta - \theta^3 \\
\psi_4' &= -s^3\theta^2 + (\theta^4/2) + (s^6/15) \\
\psi_5' &= -[(s^3\theta^3)/3] + (\theta^5/10) + [(s^6/15)\theta] \\
\psi_1' &= -\theta s \\
\psi_2' &= s\theta^2 - [(1/6)s^4] \\
\psi_3' &= -s\theta^3 + [(1/2)s^4\theta] \\
\psi_4' &= s\theta^4 - s^4\theta^2 + [(1/21)s^7] \\
\psi_5' &= -[(s\theta^5)/5] + [(s^5\theta^3)/3] - [(1/21)s^7\theta]
\end{aligned}\right\} \quad (41)$$

Only the odd numbered solutions are suitable for computing flows in a symmetrical channel. These solutions were first given by Tricomi in the form

$$\psi_1' = r^n F\left(-n, n + \frac{1}{3}; \frac{2}{3}; \frac{r + \theta}{2r}\right)$$

$$\psi_2' = r^n s F\left(-n, n + \frac{5}{3}; \frac{4}{3}; \frac{r + \theta}{2r}\right)$$

where n is a positive integer, F is the hypergeometric function, and $r = \sqrt{[(4/9)s^3] + \theta^2}$. We may thus construct a solution of the hodograph equation which represents a flow through a channel by taking a combination of three types of solutions [Eqs. (22), or (25), (39), and (40), or (41)]. This gives us several parameters by which we can vary the channel shape or the axial velocity distribution. Integrating along s = constant, the position coordinates of the point (s, θ) are additive. Thus, if $\psi_1(\theta, s)$ is one streamfunction with position coordinate z_1 and $\psi_2(\theta, s)$ is another with position coordinate z_2, the coordinate of $\psi_3 = \psi_1 + \psi_2$ is then $z_1 + z_2$.

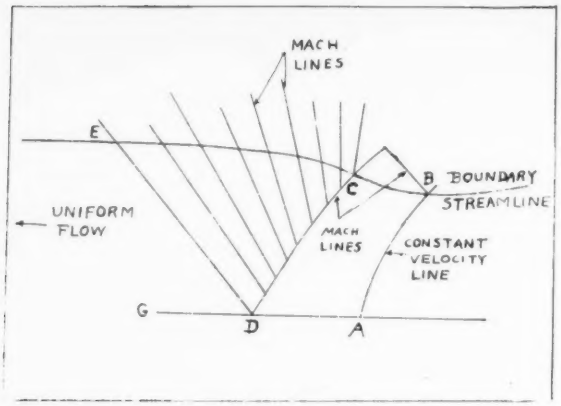

FIG. 8. Schematic diagram for terminating channel in a uniform supersonic flow.

(XII) TERMINATION OF THE NOZZLE BY A UNIFORM FLOW

It is possible by means of the method of characteristics to terminate the nozzle in a finite distance by a uniform flow. The transonic portion of the nozzle may be constructed up to some curve $q = a$ constant in the supersonic region by means of the analytic methods presented in the previous sections. Thus along this curve the quantities q, θ, and M are known. The choice of q must correspond to a Mach Number greater than about 1.10 since the method of characteristics is not so accurate for lower Mach Numbers. We must also specify that the velocity must be tangential to the center axis AG in Fig. 8. With these initial and boundary conditions, the flow may be constructed in the quadrilateral region ABCD, where BC and CD are Mach lines. Consequently, the channel walls may be found by continuing the selected streamline through this region. The extent of the region ABCD is determined by the choice of Mach Number for the uniform flow, which is the Mach Number corresponding to the axial point D.

To obtain a uniform flow beyond the point D, we make use of Prandtl-Meyer flow, which consists of one family of straight Mach waves. From the characteristic CD we construct the family of straight lines, having the direction of the Mach angle as measured from the direction of flow at each point along the characteristic CD as shown in Fig. 8. Along straight characteristics in the physical plane for two dimensional flow the quantities q, θ, and M are constant. The boundary streamlines may be extended by drawing straight line segments from each straight Mach line, having the direction of the velocity vector which corresponds to the point of intersection of the straight lines on the Mach line CD. Drawing a smooth curve through the vertices will yield the channel wall. Beyond the Mach line DE, the flow will be uniform. The accuracy with which the flow is calculated in the region DEF depends upon the number of straight lines drawn.

TABLE 1

Tabulation of s, $1/q$, q, and $1/\rho$

s	$1/q$	q	$1/\rho$
0.34	1.45156	0.68891	1.27356
0.26	1.35002	0.74073	1.33361
0.18	1.26118	0.79291	1.39801
0.16	1.24065	0.80603	1.41545
0.14	1.22071	0.81920	1.43333
0.12	1.20135	0.83240	1.45175
0.10	1.18252	0.84565	1.47078
0.08	1.16420	0.85896	1.49050
0.06	1.14636	0.87233	1.51096
0.04	1.12897	0.88576	1.53223
0.02	1.11200	0.89928	1.55437
0.00	1.09544	0.91288	1.57741
−0.02	1.07927	0.92655	1.60151
−0.04	1.06345	0.94034	1.62666
−0.06	1.04797	0.95423	1.65293
−0.08	1.03282	0.96822	1.68042
−0.10	1.01796	0.98236	1.70918
−0.12	1.00339	0.99662	1.73929
−0.14	0.98908	1.01104	1.77084
−0.16	0.97502	1.02562	1.80387
−0.18	0.96120	1.04037	1.83848
−0.22	0.93420	1.07044	1.91318
−0.27	0.90152	1.10924	2.01693
−0.32	0.86986	1.14961	2.13391

TABLE 2

Tabulation of s, s^*, and ω_1

s	s^*	ω_1
0.31	0.20075	1.16534
0.26	0.14508	1.23307
0.18	0.09521	1.30080
0.16	0.08355	1.31774
0.15	0.07782	1.32620
0.14	0.07217	1.33467
0.12	0.06109	1.35160
0.10	0.05028	1.36854
0.08	0.03973	1.38547
0.06	0.02944	1.40240
0.04	0.01939	1.41933
0.02	0.00958	1.43627
0.00	0.0000	1.45320
−0.02	−0.00936	1.47013
−0.04	−0.01851	1.48707
−0.06	−0.02745	1.50400
−0.08	−0.03619	1.52093
−0.10	−0.04474	1.53786
−0.12	−0.05311	1.55480
−0.14	−0.06129	1.57173
−0.16	−0.06930	1.58866
−0.18	−0.07714	1.60560
−0.22	−0.09233	1.63946
−0.27	−0.11046	1.68179
−0.32	−0.12077	1.72412

(XIII) CONCLUSION

In the preceding discussion, we have studied a group of hodograph solutions which have the singularity at the sonic point of the form

$$(\psi_\theta)_{\psi=0} \propto (1/s^\mu) \quad \text{as } s \to 0$$

and which yield flows through symmetrical channels. For $\mu = 1$, the sonic line is concave to the incoming flow and has finite curvature. In the neighborhood of the throat, the acceleration of the gas along a streamline is positive and the curvature is nonzero, except for the streamline of symmetry. For $1 < \mu < 3/2$, the flow pattern is similar to that for $\mu = 1$, with the exception that the sonic line has zero curvature where it crosses

the straight streamline and the acceleration of the gas along the axes vanishes at this point. For $3/2 < \mu < 7/4$, the sonic line is straight and the acceleration of the gas along the streamlines vanish at every point of the sonic line.

For $\mu = 1$, a simple procedure was set up for constructing a channel in which the curvature of the boundary is discontinuous at a point in the supersonic region. A similar procedure could be used for $3/2 < \mu < 1$.

It should be noted that for $\mu = 1$ and $3/2$, the solutions are relatively simple, and computations of the boundary of the throat of a nozzle are practical. Since the differential equation for ψ' is linear, the flows may be modified by adding to the singular solutions the solutions in Eq. (41) which are antisymmetrical in the flow direction and are regular in the neighborhood of $s = 0$.

References

[1] Meyer, Th., *Ueber zweidimensionale Bewegungsvorgaenge in einem Gas, das mit Ueberschallgeschwindigkeit stroemt*, Goettingen Dissertation, 1908.

[2] Taylor, G. I., *The Flow of Air at High Speeds Past Curved Surfaces*, R. & M. 1381, British A.R.C., 1931.

[3] Lighthill, M. J., *The Hodograph Method in Transonic Flow*, Proc. Roy. Soc. (London), Series A, Vol. 191, 1947. I. Symmetrical Channels, pp. 323–341.

[4] Frankl, F. I., *On a Family of Particular Solutions of the Equation of Darboux-Tricomi and Their Application to the Approximate Calculation of the Critical Current in a Given Plane-Parallel Laval Nozzle*, Doklady Akad. Nauk SSSR (NS), Vol. *56'* pp. 683–686, 1947. (See Math. Reviews, Vol. *9*, p. 390, 1948.) In Russian.

[5] Ehlers, F. E., Monograph IV, *Methods of Linearization in Compressible Flow*. Part II, Hodograph Method. Supplement I, *The Transonic Flow Through a De Laval Nozzle*, Tech. Rep. No. 102-AC49/5-100, Air Materiel Command, Army Air Forces, December, 1949.

[6] Ehlers, F. E., and Cohen, H. G., *An Investigation by the Hodograph Method of Flow Through a Symmetrical Nozzle with Locally Supersonic Regions*, NACA TN 2547, November, 1951.

[7] Loewner, C., *A Transformation Theory of the Partial Differential Equations of Gas Dynamics*, NACA TN 2065, April, 1950.

[8] Tricomi, F., *Sulle Equazioni Lineari Alle Derivate Parziali di 2° Ordine, di Tipo Misto*, Mem. R. Accad. Naz. Lincei, Series 5a, Vol. XIV, No. 7, pp. 134–247, 1923. (Also available in translation as Translation A9-T 26, Brown Univ., 1948.)

[9] Falkovich, S. V., *On the Theory of the Laval Nozzle*, Appl. Math. Mech. Akad. Nauk SSSR Prikl. Mat. Mech., Vol. 10, pp. 503–512, 1946. (See Math. Reviews, Vol. 8, p. 416.) In Russian.

[10] Molenbroek, P., *Ueber einige Bewegungen eines Gases mit Annahme eines Geschwindigkeitspotentials*, Archiv Math. Phys., Grunert-Hoppe, Ser. (2), Vol. 9, p. 157, 1890.

[11] Chaplygin, S. A., *On Gas Jets*, Scientific Memoirs, Moscow Univ., Math. Phys. Sec., Vol. 21, pp. 1–121, 1902. Translated by Brown Univ., 1944; also NACA TM 1063, 1944.

A Method for Investigating the Influence of Flexibility of the Mounting Structure . . .

(*Continued from page 106*)

$$s^{n+5} + (2\xi_V\omega_V + 2\xi_a\omega_a + 2\xi_{CM}\omega_{CM} + D_{n-1})s^{n+4} + \ldots = 0 \quad (37)$$

$$s^{n+3} + (2\xi_a\omega_a + 2\xi_{CM}\omega_{CM} + D_{n-1})s^{n+2} + \ldots = 0 \quad (37a)$$

$$s^{n+1} + [K_C(1 + N_n) + D_{n-1}]s^n + \ldots = 0 \quad (37b)$$

The sum of the real parts of the roots, which describe the damping quality of the control loop, is given by the negative value of the coefficient of the second highest term in any characteristic equation.

In order that the increasing degree of the characteristic equation with increasing complexity of the servo loop dynamics is not necessarily accompanied by a decrease of the damping quality of those roots that are characteristic for the preceding less complicated servo loop, the following relations should be guaranteed.

$$(2\xi_a\omega_a + 2\xi_{CM}\omega_{CM}) > K_C(1 + N_n) \geqq K_C \quad \text{and} \quad 2\xi_V\omega_V > 0 \quad (38)$$

On the other hand, in order to keep the power requirements of the servo system as low as possible, it is necessary, in a good design of a control system, to keep the term $2\xi_{CM}\omega_{CM}$ as small as possible. This means that, for a satisfactory design, the relations (36) should be replaced by

$$2\xi_a\omega_a > K_C \qquad 2\xi_V\omega_V > 0 \quad (38a)$$

and this, in turn, finally means

$$K = K_C/(2\xi_a\omega_a) < 1 \quad (39)$$

Thus, for all practical cases, the relations (32) should be replaced by

$$(\xi_a'/\omega_a')/(\xi_a/\omega_a) < (1/\omega_a'^2)/(1/\omega_a^2) \quad (40)$$

for $(\omega_a/\omega_M)^2 > 0$. The destabilizing term $s/\omega_a'^2$ in the load feedback loop of Fig. 3 thus becomes more and more dominant over the stabilizing term $2\xi_a'/\omega_a'$ in the same load feedback loop.

From these considerations it can be seen that for a large variety of control systems the performance quality of an otherwise excellent hydraulic servo system can noticeably deteriorate due to the elasticity of the mount. It is of no use to improve the actuator dynamics without due consideration of the compliance of any structural mounts.

On the Wake and Drag of Bluff Bodies*

ANATOL ROSHKO†

California Institute of Technology

Abstract

A modification to Kirchhoff's free streamline introduces the parameter $k = \sqrt{1 - C_{p_0}}$, which allows arbitrary base pressure and which must depend on the dynamics of the wake. For a cylinder of given cross-sectional shape, the drag, C_D, and the wake width, d', are functions of k only. These functions are used to relate C_D and the dimensionless shedding frequency, $S = nd/U_\infty$, to another number, $S^* = nd'/U_s$, which is based on wake parameters. It is found that $S^* \doteq 0.16$ for all cylinders. In another approach, k is evaluated by using Kármán's solution for the vortex street.

Symbols

c	=	distance from back of cylinder to trailing edge of interference element
c_D	=	drag coefficient
c_{p_0}	=	base pressure coefficient
d	=	cylinder diameter or breadth
d'	=	distance between free streamlines
h	=	width of vortex street
k	=	base pressure parameter (U_s/U_∞ or $\sqrt{1 - c_{p_0}}$)
l	=	longitudinal vortex spacing
n	=	vortex shedding frequency
R	=	Reynolds Number based on cylinder diameter ($U_\infty d/\nu$)
R^*	=	Reynolds Number based on wake parameters ($U_s d'/\nu$)
S	=	cylinder Strouhal Number (nd/U_∞)
S^*	=	wake Strouhal Number (nd'/U_s)
u	=	velocity of vortices relative to free-stream velocity
U_∞	=	free-stream velocity
U_s	=	velocity on free streamline at separation
Γ	=	circulation per vortex
ϵ	=	fraction of shear layer vorticity which goes into individual vortices
λ	=	wake width factor, h/d'

(I) Introduction

The problem of the flow about a bluff body is returned to, in the literature, again and again. The reason for this is clear enough —not only is the problem always of great practical importance, but it has so far not given way to theoretical treatment. In fact, there has been little new advance in the theory during the past 40 years, the contributions of Kirchhoff and Kármán still remaining the cornerstones from which almost all writers start. A large part of the theoretical work since then has been little more than elaboration and extension of those theories. But, as already pointed out by the early investigators, there seems little hope of arriving at a complete theory before something is understood of the essentially nonsteady processes in the wake immediately downstream of the cylinder—i.e., the dynamics of the vortex formation. It is unfortunate that more of the energy has not been applied in this direction. However, this part of the problem does indeed appear formidable, and one would like to progress a little further without having to tackle it directly.

Possibly not enough attention has been paid to the experimental information that has been accumulated and which is indispensable for the realistic formulation of theoretical models. The work of Fage and his associates[1, 2] can be singled out as a particularly fruitful source of experimental results that have not been fully exploited.

It is the purpose of the present paper to give an overall view of the aspects of the problem which must be considered, and *combined*, in any complete theory. These are, principally, the potential outer flow and the wake. It is shown that a realistic representation of the potential flow, in the vicinity of the cylinder, may be obtained by a modification of Kirchhoff's method. This depends, however, on a parameter that can be determined only from a consideration of the wake. The crucial region in the "joining" of the potential part of the solution to the wake is the region of vortex formation just behind the body. Some experimental results are presented to demonstrate how critically the whole problem depends on that region. Nevertheless, even without understanding the vortex formation, the modified Kirchhoff theory may be combined with some considerations about the wake to obtain a solution. This is still semiempirical, but the empiricism is a minimum, and a useful unification of different bluff body shapes is obtained.

(II) Modified Kirchhoff Method

The main feature of flow past a bluff body is its separation from the body surface, well ahead of the rear stagnation point, and the formation of a large wake. The presence of the wake alters the flow and the pressure distribution on the body, as compared to the potential solution, resulting in a deficit of pressure on the downstream side and an excess in front. This gives a net *pressure drag* quite distinct from that due to friction.

Presented at the Aerodynamics Session, Twenty-Second Annual Meeting, IAS, New York, January 25–29, 1954.

* The experiments reported were performed in the 20- by 20-in. low-turbulence wind tunnel at GALCIT. The major portion of this work was under the financial sponsorship of the National Advisory Committee for Aeronautics. The author is indebted to Dr. H. W. Liepmann, under whose program of general turbulence research the present investigation was conducted.

† Research Fellow, Department of Aeronautics.

In the approach taken by Kirchhoff, the problem is to find the drag by calculating the pressure distribution. For this, one has the experimental observation that the separated boundary layer continues downstream as a free shear layer, which is well defined at first and forms a boundary of demarcation between the wake and the (distorted) potential outer flow. The problem consists then of finding the shape of this boundary (which is idealized as a surface of velocity discontinuity, or so-called *free streamline*) so that the potential outer flow, and thus the pressure distribution, may be calculated. The basic assumption in the Kirchhoff theory is that the pressure everywhere in the wake is the free-stream pressure, p_∞. This then is also the pressure on the "base" of the body, downstream of the separation point, as well as all along the free streamline. The magnitude of the velocity at the separation and on the free streamline must then be the free-stream value, U_∞. Thus, in the hodograph plane, the free streamline is simply a circle and permits an elegant solution.

However, the calculated drag is considerably lower than what is observed, the discrepancy being directly due to the assumption about the base pressure, which is observed to be actually much lower than p_∞. On the other hand, the measured pressure is remarkably uniform over the base. This, and the fact that free streamlines appear to be good representations of the free shear layers, indicates that the Kirchhoff method should be sound, provided more realistic (lower) values are chosen for the base pressure. But then the pressure in the wake can no longer be uniform, for it must eventually become p_∞, far downstream. On the other hand, there need not be too much concern about the details of the solution far downstream, for in any case the free streamline representation will be valid for only a few diameters downstream of the body. The main aim should be to find a model that will give an accurate representation in the vicinity of the body and permit the pressure distribution on the body to be calculated.

Such a solution was first obtained by Riabouchinsky,[3] who avoids the problem of the pressure distribution in the wake by constructing a closed wake, or cavity, instead of letting it extend to infinity downstream. The pressure in the cavity is uniform but may have arbitrary values. Thus a family of cavity flows is obtained in which the dimensions of the cavity, as well as the pressure distribution and drag of the body, depend on the cavity pressure as parameter. However, Riabouchinsky's solution was not exploited by him or anyone else for other than cavitation flows.

In a somewhat different approach taken by the present writer,[4] the Kirchhoff method is simply modified to allow arbitrary base pressures. To demonstrate how this is accomplished, Kirchhoff's example of a flat plate set broadside to the (two-dimensional) flow is sketched in Fig. 1. The essential step, following Helmholtz and Kirchhoff, is the mapping of the flow onto the hodograph plane, from where it may be mapped onto the plane of the complex potential, and the potential flow completely determined. The vector from o, in the hodograph plane, to any other point represents the velocity at the corresponding point in the physical plane. Thus the velocity which at "a" has the free stream value U_∞, decreases along ao until it is zero at the stagnation point. Then it increases again, along the front of the plate, until it reaches the value U_s at the separation point on the edge of the plate. Whereas in the Kirchhoff theory this is fixed at the free-stream value, here we allow it to have an arbitrary value U_s, greater than U_∞. Correspondingly, the pressure there, and on the base, will have the value

$$p_s = p_\infty + (1/2)\ [\rho(U_\infty{}^2 - U_s{}^2)]$$

which is lower than p_∞. Written as a pressure coefficient, the base pressure is

$$C_{ps} = \frac{p_s - p_\infty}{(1/2)\rho U_\infty{}^2} = 1 - \left(\frac{U_s}{U_\infty}\right)^2 = 1 - k^2 \quad (1)$$

where

$$k = (U_s/U_\infty) \geq 1$$

From s, in the hodograph plane, the free streamline must return to a, the point at infinity. Now one feels that, since the pressure is uniform over the base, it should be uniform for some distance downstream in the wake—that is, that the pressure and the magnitude of the velocity along the free streamline are constant at first. The corresponding trace in the hodograph plane is a circular arc, and we simply assume that the arc extends through a full 90° as shown, until the direction is parallel to the free stream. From this point, b, it proceeds to a without further change of direction. In this way we obtain, in the hodograph plane, a "notched" circular hodograph that can easily be mapped into the complex potential plane, and, in the physical plane, a wake that has a definite width, d'. The solution depends on the single parameter k—i.e., on the base pressure. The Kirchhoff solution is the limiting case, $k = 1$, shown in the hodograph by the dotted circle. A typical pressure distribution for arbitrary k is sketched in Fig. 1.

It is shown in Fig. 4 that if the value of k (i.e., of C_{ps}) is chosen to correspond with the measured base pressure, then the calculated pressure distributions along the free streamline and on the front of the body agree well with the measured distributions, so that the measured and calculated values of drag are also in excellent agreement. On the other hand, such good agreement is not obtained when the pressure on the free streamline is assumed to start increasing immediately after separation. Therefore the assumption of a circular, notched hodograph appears to be a good one and may be applied with confidence to other cylinder shapes. In addition, it defines a definite wake width, d', which will presently prove to be most useful. The Riabouchinsky model gives equally good agreement between measured

and calculated drag, for it also assumes constant pressure along the free streamline. It also gives a definite wake dimension for each value of k. Thus, for representing the early part of the flow, the two solutions are entirely equivalent, although they differ slightly in numerical detail.

The dependence of the drag (C_D) and the wake width (d'/d) on the parameter k, which fixes the base pressure, is shown in Figs. 2 and 3, which have been adapted from reference 4.

The Kirchhoff method is by no means restricted to this case of the "bluff plate." In fact, there is extensive literature on free streamline theory in which applications to many different body shapes may be found. Almost always, however, the Kirchhoff assumption is retained—that the base pressure is p_∞—and correspondingly the resulting values of drag are always too low. For instance, when applied to the circular cylinder,[5, 6] the theory gives a drag coefficient 0.5, as compared to the experimental value of about 1.0.

In the application of the theory to a circular cylinder, or any smooth cylinder without edges, some additional difficulties are encountered, for in such cases the separation point is not fixed once and for all. It is assumed then that at separation the free streamline has the same curvature as the body surface. This gives a unique additional condition that makes the problem determinate. Although this does not give the "pressure bump" that is actually required to separate the boundary layer, it does give a solution that is reasonable in the large, and which may be expected to give reasonable values of the drag, provided the base pressure is chosen realistically and is not restricted to the Kirchhoff value. In reference 4 the notched hodograph has been adapted to this purpose. Just as for the bluff plate, a solution is obtained in which the drag and the wake width depend on the parameter k. They have been plotted in Figs. 2 and 3, along with the results for the bluff plate. These figures contain, in addition, the results for a wedge of vertex angle 90°.

While in each case the calculated flow and the drag correspond well with experimental results, provided k is chosen appropriately, the theory now is not closed, for it does not tell how to determine the parameter k. This, in fact, is the position we should expect to be in, for we cannot expect to obtain a complete solution without considering the mechanics of the wake. As will be shown in the next section, the wake plays an essential part in setting the base pressure, especially that part of the wake in the first few diameters downstream of the cylinder.

(III) The Coupling Region

Although the free shear layers conform well at first with the calculated free streamlines, this agreement does not hold far downstream. Instead, the well-known periodic formation and shedding of vortices occurs, resulting, further downstream, in the periodic wake structure known as the Kármán vortex street. It is this transition from the potential free streamline flow to the wake regime that is at present so little understood, but which must eventually hold the key to a complete theory. The crucial nature of this region, which might appropriately be called the "coupling region" between wake and potential outer flow, may be demonstrated strikingly by some simple experiments.

In the first of these a thin partition, or splitter plate, placed along the centerline of the wake downstream of a cylinder, is found to stop the vortex shedding. The partition need not extend all the way downstream, but only for the first four or five diameters. It appears that if the two shear layers on either side of the wake cannot "see" each other in the region where they tend to roll up, then there is no stabilizing mechanism to fix a definite, periodically alternating, vortex formation, and the shear layers then break down in some other manner, independently of each other. What is more remarkable, the splitter plate has an extremely strong influence on the drag of the cylinder. In some measurements on a circular cylinder, reported in reference 7, the drag coefficient was changed from 1.1 to 0.7 by introducing a splitter plate that extended for five diameters downstream of the cylinder. The corresponding change of base pressure coefficient, C_{ps}, was from -1.0 to -0.5. In short, the prevention of vortex formation reduces the base suction.

Some indication of what is happening may be obtained from Fig. 4, which gives the corresponding pressure distributions along the wake centerline, with and without splitter plate. This not only demonstrates the change effected in the base pressure, but also shows a pressure "valley" downstream of the base, especially pronounced when the splitter plate is absent. The minimum pressure occurs about one diameter downstream of the base, just in the region where the vortices form. Actually, the pressure there fluctuates at the shedding frequency, and it is the mean value that is given in Fig. 4. But it seems clear from this that the dynamics in the region of vortex formation are such as to create a low pressure there and that the suction on the cylinder base is intimately associated with it.

This relation between vortex formation and base pressure is further illustrated in the measurements of Fig. 5, which were obtained by using a much shorter length for the splitter plate—namely, about one diameter. This is too short to completely shield the shear layers from each other, but it does interfere with the vortex formation. For instance, the shedding frequency, at fixed free-stream velocity, is changed when the position of the plate is altered along the centerline. In Fig. 5, the shedding frequency, n, is given in the dimensionless form, $S = nd/U_\infty$, which is called the Strouhal Number. Since U_∞ is fixed in this experi-

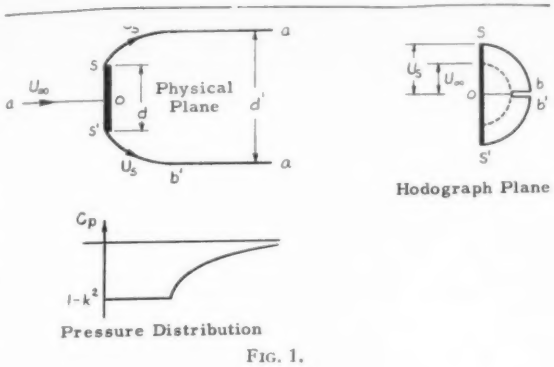

FIG. 1.

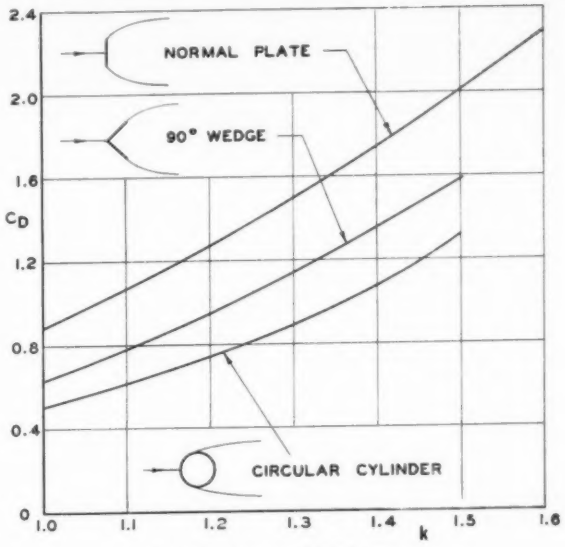

FIG. 2. Drag of bluff bodies.

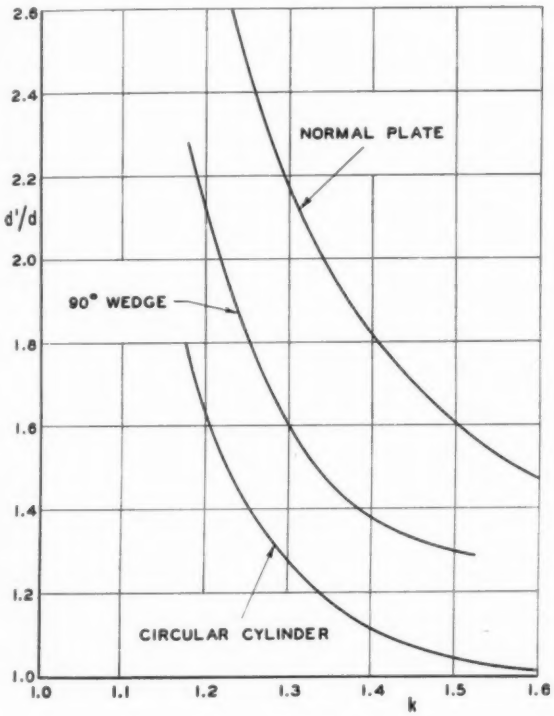

FIG. 3. Wake width.

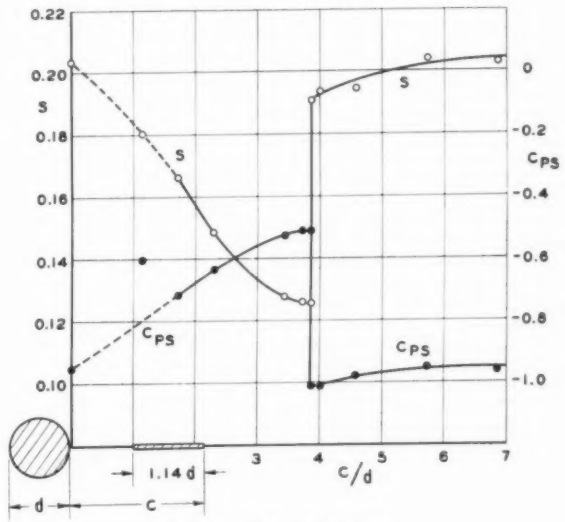

FIG. 5. Wake interference.

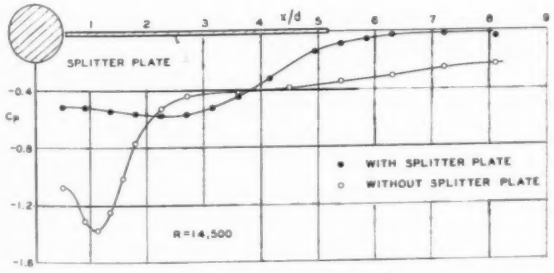

FIG. 4. Pressure on wake ℄.

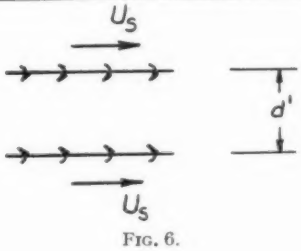

FIG. 6.

ment, S is directly proportional to the frequency. As the plate is moved downstream, the shedding frequency decreases appreciably, reaching a minimum value when the trailing edge of the plate is at four diameters downstream. Then, when the plate is moved just beyond this critical position, the shedding frequency abruptly increases, almost to its undisturbed value, corresponding to flow without interference.

The effect of the short plate in altering the shedding frequency seems to be as follows. When it is not too far from the base, the vortices form on its downstream side; this downstream shift of the formation position is accompanied by a decrease of the frequency. On the other hand, when the plate is far downstream it can have no effect, and the vortices form in their normal way. At some intermediate, critical position of the plate, the vortices have a choice of forming on either its upstream or its downstream side. Since there is no possibility for a gradual transition from one regime to the other, there must be an abrupt jump at that position.

This phenomenon is in itself interesting, but the experiment demonstrates two other important points. First, the interference is effective only in the region where the vortices form; farther downstream it has no important effect on the vortex shedding. Second, the interrelation between the vortex formation and the base pressure is clearly demonstrated by the measurements of base pressure, C_{ps}, which are also given in Fig. 5 and which were made simultaneously with the measurement of the shedding frequency. As the plate is moved downstream, the decrease in shedding frequency is accompanied by an increase in base pressure, which abruptly decreases again at the critical position. The increase in base pressure—i. e., decrease in suction—is no doubt partly due to the removal of the minimum pressure point from the base as the region of vortex formation is forced to move downstream. In addition, the minimum pressure itself may increase, but this point was not investigated.

The measurements given here were for the circular cylinder, but the same effects are observed for other bluff cylinders. What is clear from these experiments is that in every case the flow in the coupling region, in the first few diameters downstream of the base, is critical for the determination of the base pressure and of the overall flow. The important effect of interference elements on the vortex formation, and thus on the base pressure, indicates that there will have to be some understanding of the dynamics of these vortices. That problem is made difficult not only by its nonstationary nature, but also by the fact that, for the Reynolds Numbers of interest, the vortex formation takes place in turbulent fluid.[8]

This introduces the difficulties that are encountered in any turbulent flow and makes a theoretical determination of the base pressure parameter, k, seem rather remote at present. However, there are other possibilities for exploiting the results of the free streamline theory. Two of these are explored in the following two sections.

Table 1

	C_D	S
Circular cylinder	1.0	0.21
90° wedge	1.3	0.18
Bluff plate	1.7	0.14

(IV) Bluffness

One of the features of bluff body problems which has not received sufficient attention is the idea of "bluffness" itself, though the usage of the term implies something about the associated flow characteristics. However, this usage has been mainly qualitative or intuitive. With the results of the free streamline theory it becomes possible to place these intuitive ideas on a somewhat firmer basis and to correlate them with some other experimental observations that are not so intuitive. The main features associated with bluffness may be enumerated as follows.

(1) Of two bodies having the same frontal area, the bluffer one tends to diverge the flow more, to create a larger wake, and to experience a higher drag. The results of the free streamline theory are quite in accord with this definition, as is evident from Figs. 2 and 3. In Fig. 2 the three cylinders are arranged in terms of increasing drag, in the order: circular cylinder, 90° wedge, and flat plate (normal to the flow). Their bluffness is, by definition, increasing in that order. Then, in Fig. 3, the same ordering of bluffness is obtained in terms of the wake width.

(2) It is a matter of observation that bluffer cylinders have lower Strouhal Numbers. For instance, for the three cylinders that we have singled out for discussion, the typical values of Strouhal Number are given in Table 1, together with typical values of drag coefficient, for comparison. Fage and Johansen[2] made the pertinent observation that the shedding frequency is related not to the cylinder dimension but to the width of the wake, being inversely proportional to it. This explains why the bluffer cylinders, which have wider wakes, have lower shedding frequencies and correspondingly lower Strouhal Numbers.

(3) In the comparisons of bluffness made in Figs. 2 and 3 and it has been implied that the value of k is is the same, or nearly so, for the different cylinders. This is fairly well supported by the experimental results. For different cylinders the base pressures are approximately equal, within about 10 per cent, provided there is no interference in the wake. Whatever variations of base pressure do exist do not show any systematic variation with bluffness but appear, rather, to be related to Reynolds Number effects. Thus the variation between different cylinders is no more than what may be obtained for the same cylinder at differ-

ent Reynolds Numbers. The remarks here apply to a range of Reynolds Numbers of about 500 to 10^5 for the circular cylinder and to even higher values for the other two. This is the range in which C_D is ordinarily described as being constant, but actually this also varies somewhat with R, and, in fact, the variations are associated with those in C_{ps}. Likewise, the Strouhal Number may be described as constant only to the same degree, its variations also being associated with the variations in C_{ps}. Over this Reynolds Number range the values of C_D and S are within 10 per cent of those given in Table 1 and, for our present purposes, may be assumed to be constant.

(4) The above remarks apply to cylinders with undisturbed wakes. If interference elements are placed in the wake, as described in the above experiments, then significant changes are produced in C_{ps}, and, correspondingly in C_D and S. The important result is that, for a *given* cylinder, a decrease in drag is accompanied by a decrease in shedding frequency. This is at odds with the behavior indicated in Table 1 for *different* cylinders, but it will be seen to be entirely in agreement with the observation that shedding frequency decreases when wake width increases. For, as seen from Figs. 2 and 3, a decrease in drag of a *given* cylinder corresponds to an increase of wake width. This seems contrary to intuition, but it may be pointed out that the increase in wake width is accompanied by a decrease in wake velocities sufficient to give a net decrease in wake energy.

(It should be noted here that the results of Figs. 2 and 3 for the circular cylinder are not applicable when the separation point is on the back side of the cylinder, as happens at Reynolds Numbers above the critical value of about 10^5. In such cases the wake width will be smaller than the cylinder dimension, and increasing wake width will correspond to *increasing* drag. In those cases where the separation point is on the back, the free streamline theory encounters some difficulties, which are connected with the fact that the hodograph plane becomes double sheeted.)

(5) The wake structure of different bluff bodies is similar. That is, the shape, or bluffness, of the body has no characteristic effect on the wake other than to determine its geometrical and velocity scales.

These several observations on the characteristics of bluffness may be incorporated into a simple dimensional analysis. Consider the two parallel vortex sheets sketched in Fig. 6, which are intended to be idealizations of the two free shear layers created by some bluff body. If these vortex layers roll up to form vortices, then the frequency with which this occurs should depend only on the characteristic velocity, U_s, and the dimension, d', associated with the configuration. It should not depend on the body that created it. In other words, there should be a Strouhal Number for the *wake*, defined as

$$S^* = nd'/U_s \tag{2}$$

which should be universal for the vortex shedding from different bluff bodies. Of course it may be expected that there will be some variation with Reynolds Number, just as for the ordinary Strouhal Number. For the present, we propose to take this into account only roughly, by defining a wake Reynolds Number

$$R^* = U_s d'/\nu \tag{3}$$

To take the Reynolds Number effects into account more precisely will complicate matters considerably. For instance, the shear layers set up by different bluff bodies will not be the same, even at the same R^*, for they may have had different histories up to the point where they start to roll up. Thus they may be thicker or thinner, may have become turbulent earlier or later, etc., and these features will have an important influence on the vortex dynamics. They will therefore be extremely important for the vortex dynamics and the base pressure. However, our considerations are only kinematic, and, for that, the secondary Reynolds Number effects, the details of the free streamline shape, etc., may be less important.

To confirm that such a universal wake Strouhal Number exists, some measurements were made on the three different cylinders, with and without wake interference, as follows. The wake Strouhal Number is related to the ordinary Strouhal Number by

$$S^* = \frac{nd}{U_\infty}\frac{d'}{d}\frac{U_\infty}{U_s} = \frac{S}{k}\frac{d'}{d} \tag{4}$$

To determine S^*, two measurements are needed. S is determined in the usual way from a measurement of the shedding frequency. k is determined from a measurement of the base pressure, using the relation (cf. Eq. 1)

$$k = \sqrt{1 - C_{ps}} \tag{5}$$

These are the only measurements needed, for the other factor, d'/d, then is given by the free streamline results in Fig. 3. The relation (5) may be regarded as the essential one in the coupling between the potential flow and the wake, for it determines, for a given cylinder, the wake velocity and dimension in terms of the base pressure. The results, plotted in Fig. 7, show that there is indeed a universal relation, $S^* = S^*(R^*)$. Possibly the scatter is too large to show any functional trend, as has been attempted with the solid line, and one should simply assume that S^* is constant at about the value 0.16. The discrepancies at the lower values of R^* are probably more than experimental and may be related to some of the secondary Reynolds Numbers referred to above. At those low values, the free shear layers may be laminar for a considerable length, before transition occurs, and this transition point may be quite different for different cylinders, even at the same R^*.

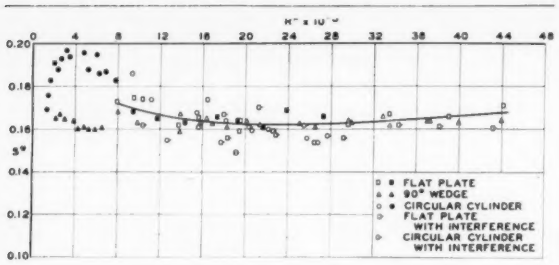

FIG. 7. Wake Strouhal Number.

It will be noted that the parameter S^* incorporates the observation made by Fage and Johansen—namely, that the shedding frequency depends on the wake dimension rather than the cylinder dimension. S^* is more general in that it includes also the wake velocity, U_s. This was not necessary in Fage's treatment, since all the cylinders considered had essentially the same base pressure and thus the same U_s. By including U_s, the parameter S^* can be extended to a larger class of flows, in particular those for which the base pressure changes appreciably, as for instance with wake interference. Still another important point of difference is that the wake width is not measured, as in Fage's case, but is calculated from the free streamline theory, using the measured base pressure. This is especially convenient when the results are used in the reverse direction. For instance, it is possible to infer the drag of a given cylinder simply from a measurement of its shedding frequency, for then the factor

$$k(d/d') = S/S^* \doteq S/0.16 \tag{6}$$

is readily computed and k is determined with the help of Fig. 3. The drag coefficient is then obtained from Fig. 2. (In case S^* varies a little with R^*, the calculation may still be made easily by iteration.)

(V) On Closing the Kármán Solution

There is another way in which the potential free streamline flow may be joined to the wake. It will be recalled that in Kármán's treatment of the vortex street there are two undetermined parameters, which are usually found from experiment. These two parameters, which are essentially a dimension and a velocity, are just the ones that are needed to relate the vortex street, or wake, to whatever body produces it, as explained in the last section. Now since the free streamline theory also gives a velocity and dimension (U_s and d'), which vary with k, it would appear to be straightforward to determine k uniquely by combining the two theories. For instance, the drag must be the same, whether calculated from the free streamline theory or from Kármán's drag formula for the vortex street.

The possibility of joining the free streamline flow to the vortex street was first proposed by Heisenberg.[9] He retained the Kirchhoff assumption that the base pressure is at the free-stream value, and this forced a redundancy on his model, for the drag is then fixed at the Kirchhoff value. With the free streamline theory, in which the base pressure is variable, a more realistic formulation is possible.

Unfortunately, the lack of understanding about the coupling region again precludes a strictly theoretical solution. For instance, it becomes necessary to know how much of the vorticity in the shear layers appears in individual vortices farther downstream. One might be inclined to assume that all of it does, but Fage and Johansen[2] showed that such is not the case, and they estimated that only about one-half of the vorticity goes into individual vortices, the rest being canceled by mixing with opposite vorticity in the coupling region. This introduces an empirical factor into the solution, but it will nevertheless be of interest to carry it through. The details are as follows.

Along a shear layer (Fig. 6) the circulation per unit length is U_s, and the average velocity is $(1/2)U_s$, so that the rate at which circulation is transported downstream is $(1/2)\ U_s^2$. In the vortex street, where the vorticity is concentrated into individual vortices, each having circulation Γ, the rate of transport of circulation in each row is $n\Gamma$, where n is the shedding frequency. But according to the observation by Fage, this is only a fraction, ϵ, of the transport along the shear layer—that is

$$n\Gamma = \epsilon U_s^2/2 = \epsilon k^2 U_\infty^2/2 \tag{7}$$

The vortices move past a given point with the velocity $U_\infty - u$, where u is their velocity relative to the free stream, while their spacing along a row is l. Therefore, the frequency with which they pass the point is $(U_\infty - u)/l$, which must be equal to the shedding frequency, n. Introducing this into Eq. (7) and rearranging it in dimensionless form, gives

$$[1 - (u/U_\infty)]\ [\Gamma/(U_\infty l)] = \epsilon(k^2/2) \tag{8}$$

Then, by introducing one of Kármán's stability parameters, $\Gamma/(ul) = 2\sqrt{2}$, it is possible to eliminate Γ from Eq. (8), and to obtain

$$\frac{u}{U_\infty} = \frac{1}{2}\left(1 \pm \sqrt{1 - \frac{\epsilon k^2}{\sqrt{2}}}\right) \tag{9}$$

This may be regarded as the expression that establishes the relation between velocities in the wake with those in the free streamline flow.

Now Kármán's formula for the drag, which he obtained from a momentum calculation on the vortex street, may be written in the form

$$C_D = (h/d)\ \{[5.65\ (u/U_\infty)] - [2.25\ \ (u/U_\infty)^2]\} \tag{10}$$

Taking h/d to the left-hand side and using Eq. (9) to replace u/U_∞ results in the expression

$$C_D\,\frac{d}{h} = 1.70\left(1 \pm \sqrt{1 - \frac{\epsilon k^2}{\sqrt{2}}}\right) + 0.563\,\frac{\epsilon k^2}{\sqrt{2}} \tag{11}$$

On the other hand, the drag may also be obtained from the free streamline theory (Fig. 2) and, when combined with the wake width d'/d (Fig. 3), gives the parameter $C_D(d/d')$ as a function of k. We now need an expression that establishes the relation between the dimension, and for this we may simply write

$$h = \lambda d' \tag{12}$$

where λ is a factor that is unknown and which again expresses the lack of knowledge of the region of vortex formation. The solution is then finally determined from the equation

$$C_D(d/h) = (1/\lambda)C_D(d/d') \tag{13}$$

The left-hand side is a function of k and ϵ and comes from the theory of the vortex street. The right-hand side is a function of k and λ and may be calculated from the free streamline theory for each cylinder. The values of k which satisfy both sides and which are the solutions are at the intersections of the two functions. In Fig. 8, the left-hand side has been plotted for several values of ϵ. The right-hand side has been plotted for the three different cylinders, with $\lambda = 1$. A most useful result is that all three fall on a *single* curve. (The branching at the higher values of k may be due to the approximate methods that had to be used for calculating the wedge and the circular cylinder. An $11^1/_4°$ wedge also falls on this universal curve.)

To actually find a solution, it is necessary to know ϵ, which can at present be found only empirically. But the important result is that this needs to be done for only one cylinder, since the others fall on the same curve. In other words, it tells that k is the same for for all the cylinders, and this, it was noted earlier, checks well with experiment. Variations in k due to variations in Reynolds Number or due to wake interference would then correspond to variations in ϵ. Actually the other empirical factor, λ, in Eq. (13) should also be included in the discussion. But it will not change the fact that all the cylinders lie on the same curve; it will merely shift the position of the curve. The value $\lambda = 1$, which is the only one plotted, seems to be as good as can be inferred from the experimental information for cylinders without wake interference. The vortex spacing h itself is not well defined experimentally, tending to increase downstream.

Once a value of k is determined, the theory will also give the shedding frequency. For instance, the universal Strouhal Number is

$$S^* = \frac{nd'}{U_s} = \frac{U_\infty - u}{l}\,\frac{d'}{U_s} = \left(1 - \frac{u}{U_\infty}\right)\left(\frac{d'}{l}\right)\left(\frac{1}{k}\right)$$

If it is again assumed that $\lambda = 1$, then the factor d'/l may be replaced by Kármán's stability ratio, $h/l = 0.281$, so that

$$S^* = (0.281/k)\,[1 - (u/U_\infty)] \tag{14}$$

u/U_∞ may be replaced from Eq. (9).

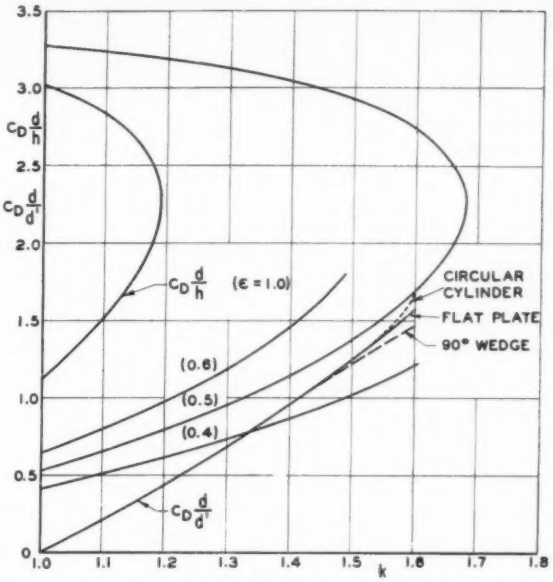

FIG. 8. Wake solutions.

For cylinders without wake interference, the base pressure coefficient for a wide range of Reynolds Numbers lies between the values -0.8 and -1.0, tending more nearly to the latter value at high Reynolds Numbers. A suitable average value for k then is 1.4. On Fig. 8 this gives an intersection at $C_D(d/d') = 0.96$ and $\epsilon = 0.43$. Then from Eq. (9), $u/U_\infty = 0.18$, and, from Eq. (14), $S^* = 0.164$, remembering that $\lambda = 1$. These are all in fair agreement with the experimental information. The drag coefficients corresponding to this value of k are 1.10, 1.32, and 1.74 for the circular cylinder, 90° wedge, and flat plate, respectively. The corresponding Strouhal Numbers calculated from Eq. (4) are 0.206, 0.167, and 0.127. Both drag coefficients and Strouhal Numbers compare favorably with the values listed in Table 1.

(VI) Concluding Remarks

The experiments with the interference elements demonstrate convincingly that the critical region for the determination of the whole flow field of a bluff body is the region of vortex formation in the first four or five diameters behind the body. Some understanding of this region will be necessary for a really complete theory without empiricism.

The flow in the vicinity of the body, as well as the drag, is described adequately by the free streamline theory, provided the right value is chosen for the base pressure. Thus the theory depends on the parameter k, but it might be pointed out that this is the *only* empirical parameter. In addition, the experimental evidence indicates, and the considerations of Section V confirm, that k is the same for different bluff bodies under similar wake conditions. This allows, in prin-

ciple the solution of different bluff bodies from only a single measurement on one of them.

The free streamline theory, based on the notched hodograph or on Riabouchinsky's model, defines a wake width that varies with base pressure. This is a relationship that is extremely useful for correlating the real wake with the flow near the body, for the drag of a given body is then associated with a wake dimension and a wake velocity. It makes possible, for instance, a simple similarity treatment of the vortex shedding and the definition of a universal Strouhal Number, S^*, with which the drag may be determined from a measurement of the shedding frequency, or vice versa. Other wake phenomena might be correlated in the same way.

The results of this paper are applicable to any other two-dimensional bluff body shape if the free streamline theory is worked out for it. This sometimes presents computational difficulties, but often no more than for the cases with Kirchhoff's assumption to which a great deal of effort has been devoted. Most of the considerations of this paper could also be applied to three-dimensional bluff bodies, especially bodies of revolution, if the appropriate free streamline flows could be worked out. Here the methods of conformal mappings are not available to facilitate the calculations, nor is there a theory of the wake corresponding to Kármán's theory of the vortex street.

In the experiments presented here the maximum cylinder Reynolds Numbers were about 20,000, but the same treatment should apply to much higher Reynolds Numbers. For bodies like the flat plate and wedge, in which the separation point is fixed, this should be straightforward. For cases like the circular cylinder, in which the separation point moves to the back at higher Reynolds Numbers, it is necessary to work out a suitable free streamline theory. Otherwise, the interaction between wake and cylinder should be qualitatively the same as at the lower Reynolds Numbers. For instance, some recent measurements[10] on circular cylinders above the critical Reynolds Number show that the Strouhal Number is about 0.4 when the drag coefficient is 0.4. The typical value of base pressure at these Reynolds Numbers is -0.4, for which $k = 1.2$. Assuming that the universal Strouhal Number, $S^* = 0.16$, applies here, the wake width may be calculated from Eq. (4). It is found to be $d'/d = 0.5$, which is reasonable, and supports the view that the processes in the wake are essentially unchanged at Reynolds Numbers above critical.

References

[1] Fage, A., and Johansen, F. C., *On the Flow of Air Behind an Inclined Flat Plate of Infinite Span*, R. and M. 1104, British A.R.C., 1927; also Proc. Roy. Soc. (London), Ser. A, Vol. 116, No. 773, pp. 170–197, September, 1927.

[2] Fage, A., and Johansen, F. C., *The Structure of Vortex Sheets*, R. and M. 1143, British A.R.C., 1927; also Phil. Mag., Ser. 7, Vol. 5, No. 28, pp. 417–441, February, 1928.

[3] Riabouchinsky, D., *On Some Cases of Two-Dimensional Fluid Motion*, Proc. London Math. Soc., Vol. 25, pp. 185–194, 1926.

[4] Roshko, A., *A New Hodograph for Free Streamline Theory*, NACA TN 3168, July, 1954.

[5] Brodetsky, S., *Discontinuous Fluid Motion Past Circular and Elliptic Cylinders*, Proc. Roy. Soc. (London), Ser. A, Vol. 102, No. 718, pp. 542-553, February, 1923.

[6] Schmieden, C., *Die Unstetige Stromung um einen Kreiszylinder*, Ingenieur-Archiv., Band 1, s. 104–109, 1929.

[7] Roshko, A., *On the Drag and Shedding Frequency of Bluff Cylinders*, NACA TN 3169, July, 1954.

[8] Roshko, A., *On the Development of Turbulent Wakes from Vortex Streets*, NACA, TN 2913, March, 1953.

[9] Heisenberg, W., *Die absoluten Dimensionen der Karmanschen Wirbelbewegung*, Phys. Z., Vol. 23, p. 363, 1922.

[10] Delany, N. K., and Sorensen, N. E., *Low-Speed Drag of Cylinders of Various Shapes*, NACA TN 3038, November, 1953.

Third U.S. National Congress of Applied Mechanics

Preliminary Announcement

The Third U.S. National Congress of Applied Mechanics will be held at Brown University, Providence, R.I., during June 11–14, 1958. It is hoped that the scheduling of conflicting meetings can be avoided by this early announcement of the date chosen for the Congress. Further announcements concerning the preparation of papers will be made as the Congress draws nearer.

Inquiries regarding the Congress should be addressed to one of the following members of the Organizing Committee at Brown University, Providence 12, R.I.: Prof. D. C. Drucker, Secretary; Prof. E. H. Lee, Treasurer; or Prof. W. Prager, Chairman.

Readers' Forum

BRIEF REPORTS of investigations in the aeronautical sciences and discussions of papers published in the JOURNAL are presented in this special department. Publication is completed as soon as possible after receipt of the material. The Editorial Committee does not hold itself responsible for the opinions expressed by the correspondents.

Differentiation of Experimental Data Using Least Squares Fitting

Fredric F. Ehrich*
Westinghouse Electric Corporation, Aviation Gas Turbine Division, Philadelphia, Pa.
September 17, 1954

RECENT DISCUSSION in this column[1-4] has centered on the problem of numerical differentiation of experimental data. Simplified formulations have been offered for finding the derivatives at the central point of an odd number of uniformly spaced points. These formulations derive from fitting high order polynomials to the given points and taking the derivatives at required points.

It is proposed that a technique less sensitive to experimental error involves fitting a low order polynomial to the experimental points by means of the method of least squares. The derivatives of the low order polynomial are then a reasonable approximation to the derivatives of the experimental data and should reduce sensitivity to experimental error.

Consider N points given by the indices

$$n = \frac{-(N-1)}{2}, \ldots -2, -1, 0, 1, 2, \ldots \frac{(N-1)}{2} \quad (1)$$

where N is an odd number, as in Fig. 1. A straight line defined by

$$y = C_1 x + C_0 \quad (2)$$

may be fitted by least squares to the points giving, after some manipulation and simplification

$$y(x_0) = C_1 x_0 + C_0 = (1/N) \sum_n y_n \quad (3a)$$

$$y'(x_0) = C_1 = \frac{12}{N(N^2-1)(\Delta x)} \sum_n n y_n \quad (3b)$$

A parabola defined by

$$y = C_2 x^2 + C_1 x + C_0 \quad (4)$$

may be fitted by least squares to the points giving, after a lengthy but straightforward derivation

$$y(x_0) = C_2 x_0^2 + C_1 x_0 + C_0 = \frac{1}{N} \sum_n y_n - C_2 (\Delta x)^2 \frac{(N^2-1)}{12} \quad (4a)$$

$$y'(x_0) = 2C_2 x_0 + C_1 = \frac{12}{N(N^2-1)(\Delta x)} \sum_n n y_n \quad (4b)$$

$$y''(x_0) = 2C_2 = \frac{30}{N(N^2-1)(N^2-4)(\Delta x)^2} \times \sum_n (12n^2 - N^2 + 1) y_n \quad (4c)$$

Both results give identical formulation for the slope at the central point.

In the case of $N = 5$ points, Eqs. (4a), (4b), and (4c) become

$$y(x_0) = \frac{1}{35}[-3y_{-2} + 12y_{-1} + 17y_0 + 12y_1 - 3y_2] \quad (5a)$$

$$y'(x_0) = \frac{1}{10(\Delta x)}[-2y_{-2} - y_{-1} + 0 + y_1 + 2y_2] \quad (5b)$$

$$y''(x_0) = \frac{1}{7(\Delta x)^2}[2y_{-2} - y_{-1} - 2y_0 - y_1 + 2y_2] \quad (5c)$$

These compare with the full polynomial formulations[2,3] of

$$y(x_0) = y_0 \quad (6a)$$

$$y'(x_0) = \frac{1}{12(\Delta x)}[y_{-2} - 8y_{-1} + 0 + 8y_1 - y_2] \quad (6b)$$

$$y''(x_0) = \frac{1}{12(\Delta x)^2}[-y_{-2} + 16y_{-1} - 30y_0 + 16y_1 - y_2] \quad (6c)$$

A quantitative comparison of the two results may be had by using the formulas to take the derivatives of an analytic curve whose derivatives are known precisely. A convenient example is the exponential curve

$$y = e^x \quad (7)$$

since all its derivatives are equal. Then using the table

n	x_n	y_n
−2	3.80	44.70
−1	3.90	49.40
0	4.00	54.60
1	4.10	60.34
2	4.20	66.69

we may apply the equations for finding the derivatives and get

	Exact	Least Square Parabola	Fourth Order Polynomial
y	54.60	54.60	54.60
dy/dx	54.60	54.92	54.61
d^2y/dx^2	54.60	54.86	53.75

A further comparison may be had if we suppose that the value of y at $x = 4.00$ were mistakenly taken to be 54.70 instead of 54.60. Then we have:

	Exact	Least Square Parabola with Error in Data	Fourth Order Polynomial with Error in Data
y	54.60	54.65	54.70
dy/dx	54.60	54.92	54.61
d^2y/dx^2	54.60	52.00	28.75

* Supervising Engineer, Analytical and Mechanical Development Section, Engineering Department.

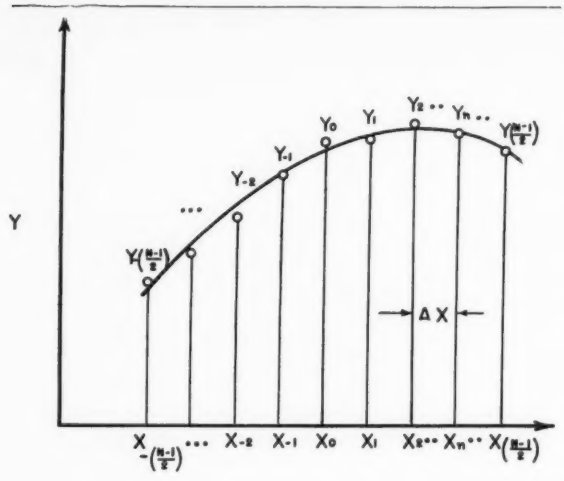

FIGURE 1

It is seen that the fourth order polynomial is completely inadequate for calculating the second derivative.

This least square technique does not lend itself to calculation of derivati.es at points other than the central point.

It should be noted that Eqs. (3a) and (3b), and Eqs. (4a,) (4b) and (4c) are extremely efficient and straightforward formulas for the actual least squares fitting—i.e., calculation of the coefficients.

References

[1] Kauffman, W. M., and Shinbrot, M., *A Method for Differentiation of Experimental Data*, Readers' Forum, Journal of the Aeronautical Sciences, Vol. 20, p. 428, June, 1953.

[2] Wang, Chi-Teh, and DeSanto, Daniel F., *Differentiation of Experimental Data by Means of Higher Order Finite-Difference Formulas*, Readers' Forum, Journal of the Aeronautical Sciences, Vol. 20, p. 792, November, 1953.

[3] Jordan, Peter F., *Differentiation of Experimental Data*, Readers' Forum, Journal of the Aeronautical Sciences, Vol. 21, p. 417, June, 1954.

[4] Schurmann, Ernest E. H., and Smith, Theron L., *Methods for Determining the First and Second Derivatives of Experimental Data*, Readers' Forum, Journal of the Aeronautical Sciences, Vol. 21, p. 420, June, 1954.

A Particular Solution of a Nonlinear Differential Equation Which Occurs in the Dynamics of Conservative Systems and Its Application to Undamped Airplane Motion

Eugene Covert
Aeronautical Engineer, Naval Supersonic Laboratory, Massachusetts Institute of Technology, Cambridge, Mass.
September 20, 1954

As the operating speed and altitude of airplanes are increased, the constant-speed stability equation is characterized by a reduction in damping and the appearance of a nonlinear pitching moment (i.e.—"spring") term. The loss in damping is due primarily to the high speed and altitude while the introduction of the nonlinear spring is characteristic of flight at transonic speeds. Since, as the damping becomes small, the response of the airplane approaches that given by the solution of the equation of motion for zero damping,[1] the solution for undamped motion is of some interest to the designer. The purpose of this note is to formulate the solution to this problem when the forcing function is a step function, or an impulse function. These solutions can be found using the classical methods of mathematics; however, the presentation below is easier to interpret.

If α and δ are the variations in angle of attack and elevator deflection from a trim position, the governing undamped differential equation can be written as[2]

$$\ddot{\alpha} + m(\alpha) = m_\delta \cdot \delta(t) \tag{1}$$

and

$$\dot{\theta} = \dot{\alpha} + \frac{g}{\alpha_{TRIM} V_{TRIM}} \alpha \tag{2}$$

where

V_{TRIM} = forward velocity at trim
g = acceleration due to gravity
θ = pitch angle, positive nose up

and positive δ is such as to pull the nose up. The dot denotes differentiation with respect to time. The spring constant [i.e.—$m(\alpha)$] can be found by matching the trim pitching moment curve with the proper cubic in α. m_δ is proportional to the slope of the pitching moment curve due to elevator deflection. $\delta(t)$ is here restricted to a step function having a magnitude $\delta_0[1(t)]$ or the Dirac impulse function $[\delta_0(t|0)]$.

By changing the variables from α and t to α and $\dot{\alpha}$ Eq. (1) becomes

$$\frac{d}{d\alpha}\left(\frac{\dot{\alpha}^2}{2}\right) + m(\alpha) = m_\delta \delta\ (t) \tag{3}$$

If $m(\alpha) = a\alpha^2 + b\alpha^2 + c\alpha$ and $\int_{\alpha(0)}^{\alpha} m(\alpha)\, d\alpha = M(\alpha)$

then Eq. (3) may be now integrated once to give

$$\frac{\dot{\alpha}^2}{2} - \frac{\dot{\alpha}^2(0)}{2} + M(\alpha) = \int_{\alpha(0)}^{\alpha} m_\delta \cdot \delta(t)\, d\alpha = \int_0^t m_\delta \dot{\alpha}(t) \cdot \delta(t)\, dt \tag{4}$$

The right-hand integral in Eq. (4) can be evaluated for the step function by integrating by parts once and recognizing that the derivative of a step function is a Dirac function $[\delta_0(t|0)]$, thus

$$m_\delta \delta_0 \int_0^t \dot{\alpha} 1(t)\, dt = m_\delta \cdot \delta_0 \left[\alpha - \int_0^t \alpha \delta_0(t|0)\, dt\right] = m_\delta \cdot \delta_0 \{\alpha - \alpha(0)\} \tag{5}$$

When $\delta(t)$ is an impulse the angular velocity has a jump proportional to δ_0 at zero time, that is

$$\dot{\alpha}(t) = \dot{\alpha}(0) + \lim_{\epsilon \to 0} m_\delta \delta_0 \int_{-\Sigma}^{\Sigma} \delta_0(t)|0)\, dt \tag{6}$$

Substituting this expression in the right-hand side of Eq. (4), then

$$\int_0^t m_\delta \delta(t) \dot{\alpha}(t)\, dt = m_\delta \delta_0 \dot{\alpha}(0) + \left(\frac{m_\delta \delta_0}{2}\right)^2 \tag{7}$$

If the results of Eqs. (5) or (7) are denoted by $g(\alpha)$, then Eq. (4) can be solved for $\dot{\alpha}$ and integrated to give

$$\mp \int_{\alpha(0)}^{\alpha} \frac{d\eta}{\sqrt{2g(\eta) - 2M(\eta) + \dot{\alpha}^2(0)}} = t \tag{8}$$

where η is a dummy integration variable. The sign on the integral is chosen to correspond to the proper initial direction of the motion, e.g.—if $\alpha(0) < 0$ choose the negative sign and if $\alpha(0) \geq 0$ the positive sign is chosen. Since $M(\eta)$ is a fourth degree polynomial, the solution can be expressed in terms of inverse Jacobian elliptic functions[3, 4] and can be inverted to give solutions in terms of $\alpha = \alpha(\sigma t, k)$. σ and k are constants in the solution.

To illustrate the above procedure consider the differential equation for a step input.

$$\ddot{\alpha} + 1.25\alpha^3 - 1.75\alpha^2 + 0.4\alpha = 0.8\delta_0 1(t) \tag{9}$$

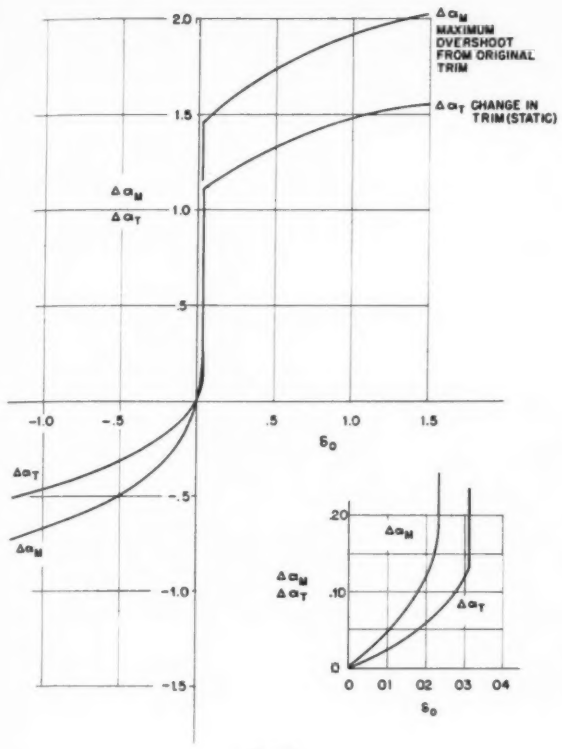

FIG. 1.

with initial conditions

$$\alpha(0) = \dot{\alpha}(0) = 0 \tag{10}$$

Substitution in Eq. (8) gives

$$\mp \int_0^{\alpha} \frac{d\eta}{\sqrt{1.6\delta_0\eta - 0.4\eta^2 + 1.17\eta^3 - 0.63\eta^4}} = t \tag{11}$$

In this case the positive sign is used with the positive δ_0 and the negative sign with the negative δ_0. Due to the initial conditions the motion always takes place between the root $\eta = 0$ of the radical and its next positive or negative root. When $\delta_0 = 0$ there is a double root at $\eta = 0$ which implies no motion. Fig. 1 shows the maximum amplitude of the motion and the static trim angle as a function of δ_0. It will be noted that for a relatively small positive change in control setting there is a large change in trim and overshoot. This is caused by the unstable region in the moment curve. The lower right-hand part of the figure shows the behavior of the two curves on a larger scale in the vicinity of this control deflection.

For small δ_0 the solution can be written as[3]

$$\alpha = \frac{a\ sn^2(\sigma t, k)}{b - c\ sn^2(\sigma, t, k)}$$

and for large δ_0 (see reference 4)

$$\alpha = \frac{a[1 - cn(\sigma t, k)]}{b + c\ cn(\sigma t, k)}$$

where a, b, c, σ, and k are constants, depending upon the roots of the quartic in the radical. Once $\alpha(\theta)$ is known, then $\theta(t)$ can be found simply from Eq. (2) by numerical integration.

The most obvious effects of the nonlinear moment curve upon the undamped motion are: (1) the overshoot is greater than twice the trim or less than twice the trim depending upon whether the negative slope of the moment curve is decreasing or increasing; (2) near the instability region small changes in control deflection have a large effect upon the airplane orientation and (3) the frequency of the motion depends upon the size of the input. Thus a great deal of useful information concerning the nature of the motion can be found from the elementary analysis of the undamped case.

REFERENCES

[1] Trilling, L., and Covert, E. E., *On the Quasi-Steady Pitching Oscillations of Transonic Aircraft.* (To be published.)

[2] Jones, B. M., *Dynamics of the Airplane*, Division N, Vol. V, Aerodynamic Theory (W. F. Durand, Ed.), Julius Springer, Berlin, 1935, pp. 99, 100.

[3] Peirce, B. O., *A Short Table of Integrals*, 3rd Rev. Ed.; Ginn and Co., Boston, 1929, pp. 66–72.

[4] Gröbner, W., and Hofreiter, N., *Integraltafel Erster Teil, Unbestimmte Integrale;* Springer-Verlag, Vienna and Innsbruck, 1949.

Further Comments on "The Effect of Boundary Layer on Sonic Flow Through an Abrupt Cross-Sectional Area Change"[1]

Robert S. Wick
Senior Research Engineer, Jet Propulsion Laboratory, California Institute of Technology, Pasadena, Calif.

September 20, 1954

COLE AND MILLS[2] have published experimental data on sonic flow through axially symmetric sudden enlargements of cross section which can be compared directly to the author's[1] results obtained for sonic flow through two-dimensional rectangular sections. The test section used by the author was of constant width, and the sudden enlargement consisted of a sudden change in the height of the test section. Thus, there were two corners in which a base pressure could be measured, and, since these corners were not interconnected, it is possible to have a nonsymmetrical condition if the pressure downstream of the expansion is raised high enough relative to the entrance condition P_1. This

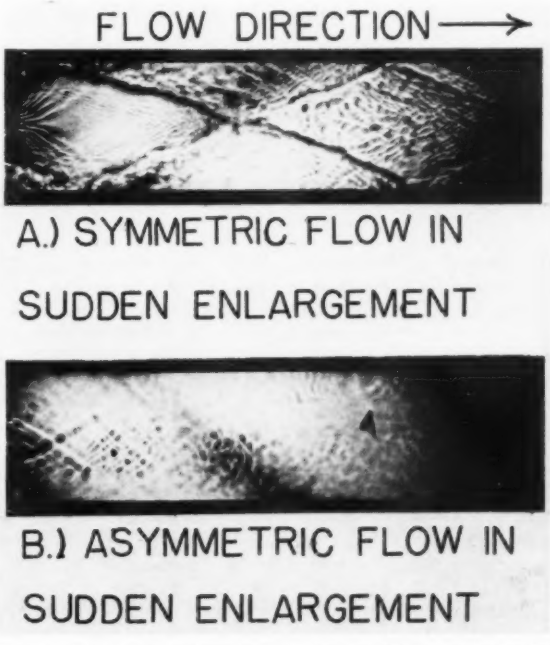

FIG. 1. Hydraulic analogy results show possible asymmetry in flow through sudden enlargements.

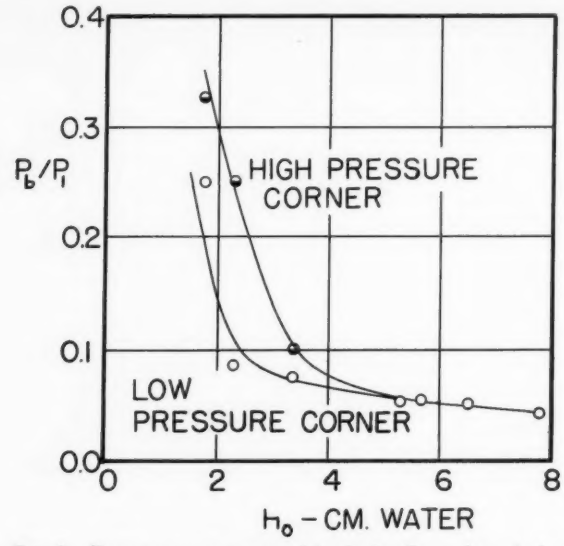

FIG. 2. Base pressures measured by hydraulic analogy during asymmetric flow through a sudden enlargement.

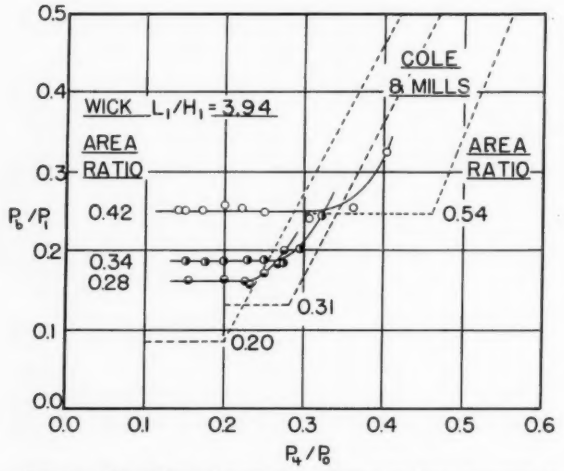

FIG. 3. The effect of reservoir pressure on base pressure in sudden enlargements. Comparison of two-dimensional tests to axially symmetric tests.

was observed by the author in both the two-dimensional, air-flow apparatus and water-table hydraulic analogy tests. Two photographs are presented in Fig. 1 of water-table results which illustrate the possible asymmetry in the two-dimensional apparatus. Fig. 2 illustrates qualitatively from water-table data how the base pressure ratio varies as the asymmetry increases with decreasing reservoir pressure h_0 (or increasing downstream pressure).

In the axially symmetric tests of Cole and Mills, the base pressure over the annular surface must be constant, since all corner regions are interconnected. In Fig. 3 some data of Cole and Mills are compared with those of the author. It must be remembered that the base pressures reported by the author were measured in only one corner of the two-dimensional flow apparatus. (The nomenclature in the figures is the same as that used in the author's paper.) The explanation for the fact that the base pressure ratio continuously decreases as the reservoir pressure P_0 is raised until a certain constant value is reached is that the flow in the downstream section is subsonic at the lower reservoir pressures, and therefore the base pressure is determined by conditions downstream of the corner. From a one-dimensional analysis [Eq. (5) of reference 1]

$$\frac{P_1A_1}{P_2A_2} = \frac{M_2}{M_1}\left\{\frac{1 + [(\gamma - 1)/2]M_2^2}{1 + [(\gamma - 1)/2]M_1^2}\right\}^{1/2} \tag{1}$$

and the fact that $P_1/P_0 = 0.528$ for sonic flow at the throat as well as the assumption that for subsonic flow in the expanded section P_2 is approximately equal to P_4 for subsonic flow, we obtain

$$M_2(1 + [(\gamma - 1)/2]M_2^2)^{1/2} = \frac{(0.528)\,(1.2)\,(A_1/A_2)}{P_4/P_0} \tag{2}$$

This one-dimensional result indicates that as the pressure ratio P_4/P_0 is lowered the Mach Number M_2 in the expanded section may be expected to increase toward unity and also that the value of P_4/P_0 at which this occurs is lower the smaller the expansion ratio A_1/A_2. The latter observation was found experimentally to be true by both Cole and Mills and the author, as is shown in Fig. 3. When the flow in the expanded section becomes supersonic, the base pressure, i.e.—pressure in the corner, is no longer determined by conditions in the downstream section but rather by conditions upstream of the sonic throat. In this flow regime both Cole's and Mills' and the author's data indicate that the base pressure ratio is a function to the first order of the expansion ratio. The diameter of the throat of Cole's and Mills' apparatus was $^3/_8$-in., whereas the dimensions of the throat used by the author were 0.380- by 0.500-in. Consequently, an excellent opportunity is afforded to compare the two-dimensional tests with the axially symmetric tests in the regime where upstream conditions may be expected to govern the base pressure ratio. The three sets of points of the author in Fig. 4 correspond to different throat lengths as indicated by the ratio L_1/h_1. The nozzle of Cole and Mills consisted of a thin nozzle plate with a $^1/_8$-in. radius on the entrance edge, and consequently the straight section of the throat must have been very short (approximately 0.2-in.).

The theoretical calculations of Korst[3] for the two-dimensional case are also shown in Fig. 4. The agreement appears to be very good for $L_1/h_1 = 3.94$. However, Korst states that the trend of the

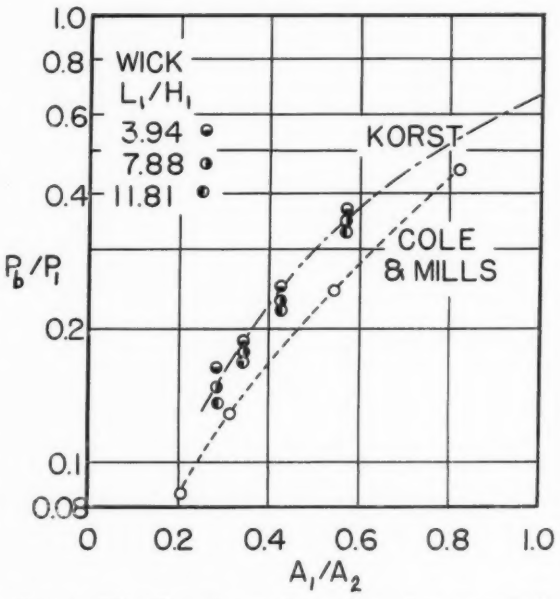

FIG. 4. The effect of expansion ratio on base pressure in sudden enlargements. Comparison of two-dimensional tests to axially symmetric tests.

data with respect to the effect of upstream boundary layer is incorrect as indicated by his theory. Korst attributes this to three-dimensional effects of the side walls, which is entirely possible when one considers that the available air supply limited the tests to an apparatus with $h_1/W = 0.7$.

An extension of the interior flow tests to the axially symmetric case such as Cole and Mills have done but with the throat section lengthened so that different boundary layers are present would be very worth while. This additional information would aid in understanding the effect of expansion waves on the wake boundary layer (see Figs. 1, 2, and 8 of reference 1). This effect is not present in the case of external flow, and one would expect the effect to be more pronounced at entrance Mach Numbers in the neighborhood of unity. As stated, the validity of comparing external flow to internal flow is limited by a number of factors. The chief advantages of studying internal flow are that from an experimental point of view the experimental equipment is cheaper and is easier to instrument for probing and for obtaining static pressures and optical data. Also, it is possible to have complete information on the nature of the boundary layer at the entrance to the sudden expansion.

As Korst points out, Eqs. (2) and (3) of the author's paper were incorrectly stated. Also, Eq. (4) should read

$$\frac{P_b}{P_1} = \frac{(1 + \gamma M_2^2)P_2/P_1 - (1 + \gamma M_1^2)A_1/A_2}{1 - A_1/A_2}$$

The caption of Fig. 4 of the author's paper should include the information that $L_2 = 7.0$, in. and $H_1 = 0.38$ in.

Professor Korst in a private communication indicates that he has extended his theory to the three-dimensional case and that within the range calculated ($A_1/A_2 = 0.6$ to 1.0) it agrees with the experimental data of Cole and Mills.

References

[1] Wick, Robert S., Journal of the Aeronautical Sciences, Vol. 20, No. 10, pp. 675–682, October, 1953.

[2] Cole, B. N., and Mills, B., *The Theory of Sudden Enlargements Applied to the Poppet Exhaust-Valve, With Special Reference to Exhaust-Pulse Scavenging*, Proc. (B) I.M.E., Vol. 1B, No. 8, pp. 364–378, 1952–1953.

[3] Korst, H. H., *Comments on "The Effect of Boundary Layer on Sonic Flow Through an Abrupt Cross-Sectional Area Change,"* Readers' Forum, Journal of the Aeronautical Sciences, Vol. 21, No. 8, pp. 568–569, August, 1954.

Determining the Mode Shapes and Frequencies of Low Aspect Ratio Multispar Wings

Marvin L. Stein

Senior Research Engineer, Convair-San Diego Division of General Dynamics Corporation, San Diego, Calif.

September 28, 1954

The dynamic equations for determining the vibration modes and frequencies of a low-aspect ratio multispar wing assume the form

$$Pf = \omega^2 Mf \tag{1}$$

where $P = (P_{ij})(i, j = 1, 2, \ldots, n)$ is a matrix of elastic coefficients and

$$M = \begin{pmatrix} M_1 & & 0 \\ & M_2 & \\ & & \ddots \\ 0 & & M_n \end{pmatrix}$$

is a diagonal matrix whose nonzero elements are concentrated masses.[3] The scalar parameter ω^2 represents the square of the frequency while the vectors f which satisfy Eq. (1) for any given value of ω^2 give the mode shapes corresponding to that frequency. From physical considerations M is positive definite while $P_{ij} = P_{ji}$ for all i and j—i.e., P is symmetric.

In general there will be only $m \leq n$ distinct values of ω^2 for which (1) has a solution f. The computational problem is to actually determine the allowable frequencies or eigenvalues and their corresponding mode shapes or eigenvectors. An extensive mathematical literature deals with this problem (see, for example, Hestenes and Karush[2]).

An equivalent formulation of Eq. (1) which is easier to handle computationally can be obtained by introducing the matrix

$$Q \equiv \begin{pmatrix} \frac{1}{\sqrt{M_1}} & & 0 \\ & \frac{1}{\sqrt{M_2}} & \\ & & \ddots \\ 0 & & \frac{1}{\sqrt{M_n}} \end{pmatrix}$$

One can then consider the eigenvalue problem

$$Az = \omega^2 z \tag{2}$$

where

$$A = QPQ, \tag{3}$$

for if ω^2 is an eigenvalue of (2) and z the corresponding eigenvector, then ω^2 and

$$f \equiv Qz \tag{4}$$

can easily be shown to satisfy Eq. (1). Since Q and P are both symmetric, A will also be symmetric. This fact is essential to the mathematical theory on which the computational technique is based and allows for considerable simplification of this technique.

A theory for solving eigenvalue problems of type (2) when A is symmetric has been developed in detail by Hestenes and Karush.[1] The "near-optimum" gradient method to be outlined here is a modification of the Hestenes-Karush method of "optimum-α." The application of this modified optimum-α technique to finding eigenvectors corresponding to zero eigenvalues has been previously described by Stein.[4] The generalization to eigenvectors associated with nonzero eigenvalues proceeds as follows:

(a) Choose an arbitrary initial vector z_i

(b) Compute the Rayleigh quotient $\mu(z_i)$, where

$$\mu(z_i) = (z_i^*, Az_i)/(z_i^*, z_i)$$

(c) Form the gradient vector $\xi(z_i)$, where

$$\xi(z_i) \equiv \xi_i = Az_i - \mu(z_i)z_i$$

(d) Compute the Rayleigh quotient for the gradient

$$\mu(\xi_i) = (\xi_i^*, A\xi_i)/(\xi_i^*, \xi_i)$$

(e) Form the scalar

$$\alpha = [\mu(\xi_i) - \mu(z_i)]^{-1}$$

(f) Choose β on the range $0 < \beta < 1$

(g) Compute the new estimate

$$z_{i+1} = z_i - \beta\alpha\xi_i$$

and repeat, replacing z_i by z_{i+1}.

The values of the quotient $\mu(z_i)$ generated by the above process will converge monotonically downward to the lowest eigenvalue while the sequence of vectors z_i will converge to the corresponding eigenvector z. The monotonicity of μ affords a good computational check. The gradient vectors ξ_i go to zero and give an indication of the accuracy of z_i and $\mu(z_i)$ as eigenvector and eigenvalue extimates.

The same procedure will also serve to find the next highest eigenvalue and its corresponding eigenvector. However, care must be taken to choose the initial estimate z_0 orthogonal to all eigenvectors y_k that are already known, i.e., to choose z_0 such that

$$(z_0^*, y_k) = 0 \qquad (i = 1, 2, \ldots, r) \tag{5}$$

The method, in theory, will preserve the relations (5) for all succeeding estimates z_i. However, in practice, an occasional reorthogonalization will be required because of the round-off error.

IBM computer techniques for carrying out a gradient method known as the method of "fixed-α" have been described by E. Yowell.[5] Since these techniques are much like those to be employed in the present method a separate description will not be necessary here.

References

[1] Hestenes, M. R., and Karush, W., *A Method of Gradients for Calculation of the Characteristic Roots and Vectors of a Real Symmetric Matrix*, J. Research NBS 47, 5 (1951), RP 2227.

[2] Hestenes, M. R., and Karush, W., *Solutions of $AX = \lambda BX$*, J. Research NBS 47, 6 (1951), RP 2275.

[3] Schuerch, H. U., *Analysis of Redundant Structures by Elastic Coefficients*, Consolidated Vultee Aircraft Corporation, Report ZS-181 (4-30-53).

[4] Stein, M. L., *Gradient Methods in the Solution of Systems of Linear Equations*, J. Research NBS 48, 6 (1952), RP 2330.

[5] Yowell, E., *The Determination of Eigenvectors and Eigenvalues of Symmetric Matrices*, Proceedings of the Computation Seminar of August, 1951, IBM Corporation, New York, N.Y.

Slender Bodies of Low Wave Drag

R. N. Haskell and G. C. Grogan

Convair-Fort Worth Division of General Dynamics Corporation, Fort Worth, Tex.

September 23, 1954

SOLUTIONS OF MINIMUM wave drag slender bodies of revolution which have been published to date are all restricted to that class of shapes termed "smooth." This requires the cross-sectional area gradient to be continuous everywhere including the nose of the body. Such a restriction is often incompatible with current design requirements.

A particular case of importance is that of a ducted body whose inlet radius and radius slope are largely set by internal aerodynamic considerations. It was to solve this problem that the authors developed a general method of designing low (though not necessarily the absolute minimum) wave drag bodies of revolution. To illustrate the method the following specific example will be studied.

Let the body be of unit length, and the following geometrical constraints be imposed:

$R(0)$ = radius at station $x = 0$
$R'(0)$ = radius slope at $x = 0$
$R(1)$ = radius at $x = 1$
$R'(1) = 0$ = radius slope at $x = 1$

The problem is to determine the body shape satisfying the above constraints and having low drag.

The appropriate drag expression is (from Lighthill[1])

$$\frac{D}{q} = -\frac{1}{2\pi}\int_0^1\int_0^1 S''(x)S''(t)\log|x-t|\,dt\,dx - \frac{S'(0)}{\pi}\int_0^1 S''(x)\log x\,dx + \frac{[S'(0)]^2}{2\pi}\log\frac{2}{\beta R(0)} \quad (1)$$

where

$S(x)$ = cross-sectional area at station x
$S''(x) = d^2S(x)/dx^2$
$\beta = \sqrt{M^2-1}$

By letting the area distribution be a power series as

$$S(x) = \sum_{i=0}^{n} a_i x^i \quad (2)$$

the above drag expression may be integrated giving

$$\frac{D}{q} = \frac{1}{\pi}\sum_{j=2}^{n}\sum_{i=2}^{n} a_j a_i b_{ij} + \frac{S'(0)}{\pi}\sum_{i=2}^{n}\frac{i}{i-1}a_i + \frac{[S'(0)]^2}{2\pi}\log\frac{2}{\beta R(0)} \quad (3)$$

where

$$b_{ij} = \frac{ij(j-1)}{i+j-2}\left[\frac{1}{i+j-2} + 1 + \frac{1}{2} + \frac{1}{3} + \ldots + \frac{1}{i-1}\right]$$

The constraints for the variational problem may be expressed as:

$$\begin{aligned} S(0) &= a_0 = \pi R^2(0) \\ S'(0) &= a_1 = 2\pi R(0)R'(0) \\ S(1) &= \sum_{i=0}^{n} a_i = \pi R^2(1) \\ S'(1) &= \sum_{i=0}^{n} i a_i = 0 \end{aligned}$$

By introducing Lagrangian multipliers the expression to be minimized is:

$$\frac{1}{\pi}\sum_{j=2}^{n}\sum_{i=2}^{n} a_j a_i b_{ij} + \frac{S'(0)}{\pi}\sum_{i=2}^{n}\frac{i}{i-1}a_i + \frac{[S'(0)]^2}{2\pi}\times\log\frac{2}{\beta R(0)} + \lambda_1\left[\sum_{i=2}^{n} a_i + a_0 + a_1 - S(1)\right] + \lambda_2\left[\sum_{i=2}^{n} i a_i + a_1\right] \quad (4)$$

since a_0 and a_1 are already known.

The above is minimized by differentiating it with respect to the a_i's (ranging from $i = 2, 3, \ldots, n$) and λ_1, λ_2. The resulting simultaneous equations to be solved for the unknowns are:

$$\left.\begin{aligned} \frac{2b_{22}}{\pi}a_2 + \frac{(b_{23}+b_{32})}{\pi}a_3 + \ldots + \frac{(b_{2n}+b_{n2})}{\pi}a_n + 1\lambda_1 + 2\lambda_2 &= 0 \\ \frac{(b_{23}+b_{32})}{\pi}a_2 + \frac{2b_{33}}{\pi}a_3 + \ldots + \frac{(b_{3n}+b_{n3})}{\pi}a_n + 1\lambda_1 + 3\lambda_2 &= 0 \\ \frac{(b_{24}+b_{42})}{\pi}a_2 + \frac{(b_{34}+b_{43})}{\pi}a_3 + \ldots + \frac{(b_{4n}+b_{n4})}{\pi}a_n + 1\lambda_1 + 4\lambda_2 &= 0 \\ \vdots \qquad\qquad \vdots \qquad\qquad \vdots \qquad\qquad \vdots \\ \frac{(b_{2n}+b_{n2})}{\pi}a_2 + \frac{(b_{3n}+b_{n3})}{\pi}a_3 + \ldots + \frac{2b_{nn}}{\pi}a_n + 1\lambda_1 + n\lambda_2 &= 0 \\ 1a_2 + 1a_3 + \ldots + 1a_n &= S(1) - S'(0) - S'(0) \\ 2a_2 + 3a_3 + \ldots + na_n &= -S'(0) \end{aligned}\right\} \quad (5)$$

Solutions for the case of

$R(0) = 0.05$
$R'(0) = 0.1$
$R(1) = 0.1$
$\beta = 1$

have been determined for three values of n($n = 3$, 4, and 5) and the results are shown in Fig. 1.

As is to be observed the radius curve quickly damps out with increasing n while the corresponding drags decrease. Comparison of this method for smooth bodies with minimum drag shapes has shown the convergence to be quite rapid and certainly adequate for engineering purposes.

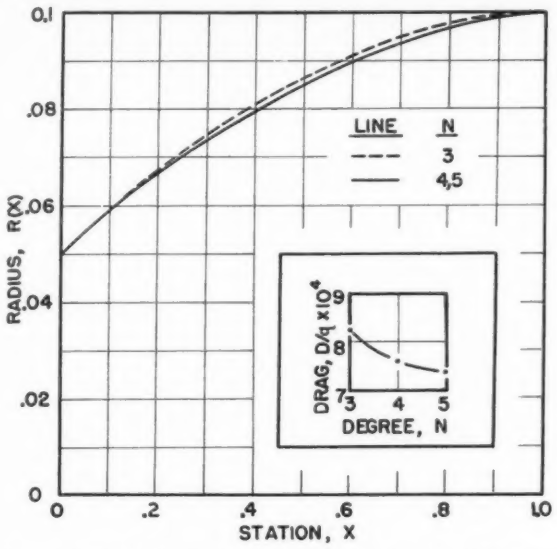

FIG. 1. Effect of degree of area distribution power series on profile shape and wave drag of example problem.

The illustrative example may be varied to include additional constraints such as prescribed areas and/or volumes. The drag expression (3) is appropriate but Eqs. (4) and (5) will have to include the additional constraint terms. If it is desired to include additional area gradient discontinuities the additional terms for the drag expression may be easily developed from reference 1. The remainder of the problem is treated in the identical manner as the example.

REFERENCE

[1] Lighthill, M. J., *Supersonic Flow Past Slender Bodies of Revolution the Slope of Whose Meridian Section Is Discontinuous*, Quart. Jour. Mech. & Appl. Math., Vol. 1, pp. 90–102, 1948.

Difference Solution of Shock Diffraction Problem[1]

H. F. Ludloff and M. B. Friedman
Daniel Guggenheim School of Aeronautics, New York University
October 22, 1954

THE TIME DEPENDENT, nonlinear equations of motion and the appropriate boundary condition have been formulated with the objective of obtaining a solution describing the reflection and diffraction of a strong shock from an arbitrary corner. The method of solution used is of more general interest than this particular problem. It is a difference procedure with the following characteristics:

(1) In spite of the conical character of the problem, the equations of motion are formulated in x-, y-, t-coordinates, in which the equations are hyperbolic.

(2) The equations are written in "divergence form" (see authors' IAS preprint 456), so that in the limit they go over automatically into the conservation laws.

(3) The difference form of the equations supplies automatically a certain amount of artificial viscosity which is necessary for the creation of varying shock intensities.

In the proposed difference form:

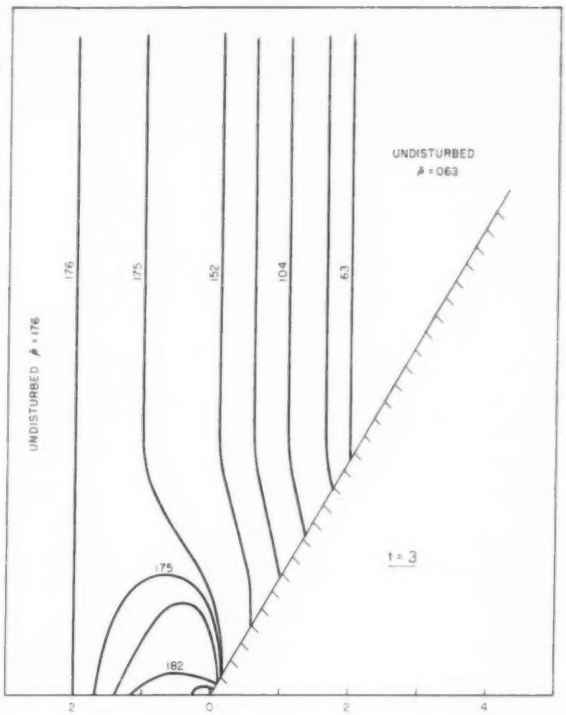

FIG 1.

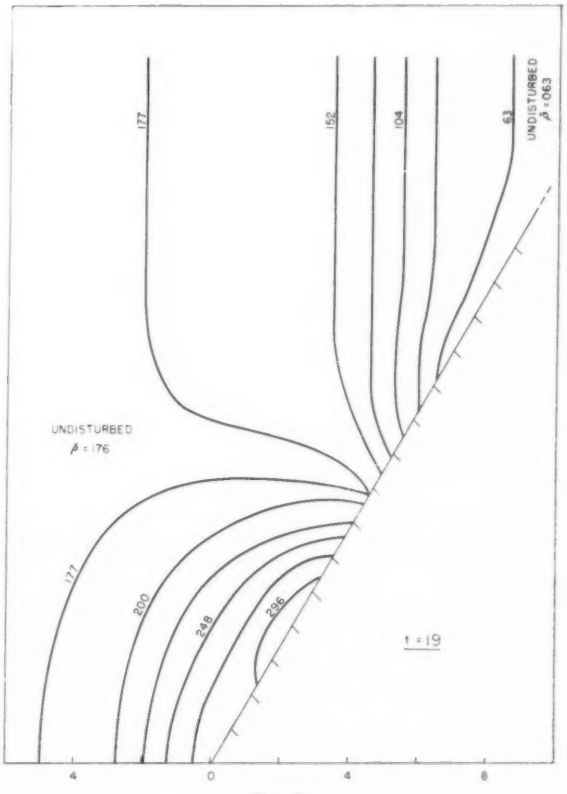

FIG. 2.

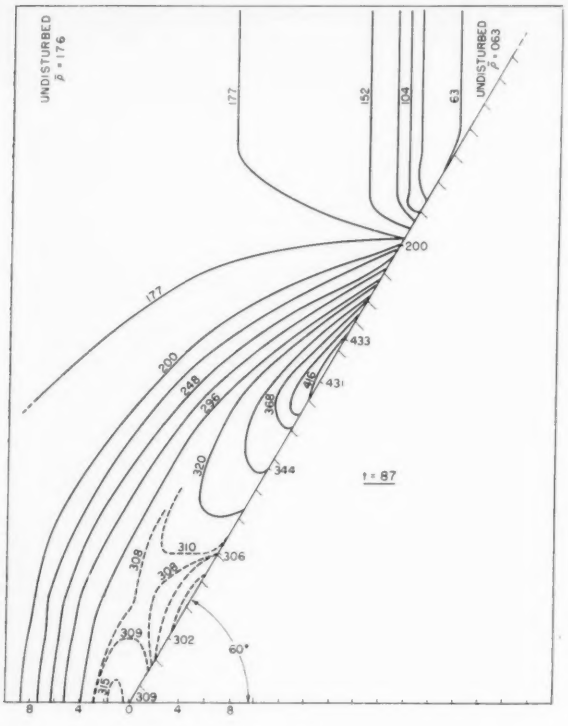

FIG. 3.

(*a*) The four equations of motion, applied at each interior point (j, k) of the field, are:

$$\left.\begin{aligned}
\rho_{j,k}^{t+1} &= \frac{1}{4}\sum_i \rho_i{}^t + \frac{\Delta t}{\Delta x}\cdot R_{K,\delta}^t(\rho, m, r),\\
m_{j,k}^{t+1} &= \frac{1}{4}\sum_i m_i{}^t + \frac{\Delta t}{\Delta x}\cdot T_{K,\delta}^t(\rho, m, r, E),\\
r_{j,k}^{t+1} &= \frac{1}{4}\sum_i r_i{}^t + \frac{\Delta t}{\Delta x}\cdot U_{K,\delta}^t(\rho, m, r, E),\\
E_{j,k}^{t+1} &= \frac{1}{4}\sum_i E_i{}^t + \frac{\Delta t}{\Delta x}\cdot V_{K,\delta}^t(\rho, m, r, E)
\end{aligned}\right\} \qquad (A)$$

In Σ, i runs through $j+1, k; j-1, k; j, k+1; j, k-1$. The four dependent variables ρ, m, r, E are the density, the two mass-flow vector components parallel and oblique to the wall, and the total energy. R, T, U, and V are certain, nonlinear difference operators, applied to the subsequent quantities ρ, m, r, E. The superscripts refer to the time cycle. The subscripts refer to the location of the net points, which occur in certain combinations K, δ. $(\Delta t/\Delta x) = (\Delta t/\Delta y)$ are chosen in accordance with the stability criterion.

(*b*) The one true boundary condition on the wall, and the initial conditions describing the field of the plane shock are obvious.

Some results of the IBM 701 machine computations are shown below. The development of the compression produced by the corner can be seen from the plot of the isopycnics ($\bar{\rho} = 62.5 \times \rho/\rho_0$ = const.) at three subsequent time cycles $t = 3$, 19, and 87. After the incident shock strikes the corner, a small circular compression pulse forms which is subsequently distorted and swept upstream in the wake of the advancing shock. At the same time, the ρ-gradients at the boundaries of the compressed domain steepen and assume the expected shape of the reflected shock. The density distribution along the wall, the ρ-value at the stagnation point and the angle of the reflected shock at the intersection point with the incident shock agree with the interferograms. In the vicinity of the latter point, there should be a completely homogeneous domain. At $t = 87$, such a region just starts to develop.

Note that the way in which the machine evolves, cycle by cycle, the final conical field, guided by the hyperbolic equations of motion, corresponds to the actual happenings in nature, except for an artificial slowdown of the sequence of events to be explained presently.

The initial field of the plane shock front may be described exclusively in terms of ideal fluid concepts; the same holds true for the final configuration. On the other hand, the gradual transition from the initial to the final field—i.e., the creation of new entropy values, initially not present, can only take place if some kind of viscous action is taken into account. Therefore, the ideal fluid equations of motion could not describe events, if used in their analytic form; inadvertently, the difference form (A) introduces the viscous action necessary to reach the objective. The difference quotients appearing in (A) are all of first order. Now, suppose each difference quotient is expanded about the corresponding derivative in powers of a mesh-width parameter. The expanded equations, then, consist of the ideal fluid equations, augmented by second order and higher derivatives. But the latter appear and behave like Navier-Stokes terms and Barnett terms, etc., in which the magnitude of the viscosity is related to the mesh width. Naturally, this artificial viscosity is not the correct one. However, that does not influence the final result which is again independent of viscosity, but only the speed with which the final configuration is reached. Thus, it happens that the difference formalism yields more than one could hope to obtain from an analytic solution; and at present even more than the experiment can provide. (See Figs. 1–3.)

REFERENCE

[1] Investigation supported by Mechanics Branch of ONR and Aeroball. Dept. of NOL.

On the Design of Two-Dimensional Supersonic Nozzles by the Method of Characteristics*

Bernard Chaix† and Peter Henrici†
Institute for Aerodynamics, Federal Institute of Technology, Zurich, and National Bureau of Standards, Washington, D.C.‡
December 31, 1954

(1) INTRODUCTION

THE DESIGN of two-dimensional supersonic nozzles for a parallel and uniform jet by the method of characteristics is subject to the difficulty that the initial conditions for the velocity potential in the transonic region of the nozzle are not known and have to be derived from suitable assumptions or from independent calculations. The two following hypotheses can be traced back to the early days of nozzle design: (a) the computation is started at the throat of the nozzle under the assumption of parallel flow in the transonic region (see, e.g., Preiswerk,[2] Puckett[5]); (b) the computation is started in the divergent part of the nozzle under the assumption that the flow can be approximated there by a suitable source flow (see, e.g., Kisenko,[4] Busemann,[3] and Foelsch,[7] who, however, replaces the method of characteristics by an analytical method; also the "hydraulic" method of O. Reynolds, mentioned by Courant and Friedrichs[9] rests on similar ideas). Concerning (a), Lighthill[8] and Sauer[10] have shown by computations based upon the power-series method of Meyer[1] that the assumption of uniform flow in

* The work of the second author was supported by the Office of Naval Research, U.S. Navy.

† The authors are indebted to Professor J. Ackeret, Zurich, for his active interest in this investigation and for making possible the experimental work.

‡ Guest worker.

the transonic region does not correspond to reality and that the curves M = const. are in first approximation parabolic arcs (open to the nozzle inlet) with a radius of curvature comparable to that of the nozzle walls at the throat. Using these results, Harrop et al.[12] constructed a set of nozzles starting from the (arbitrarily chosen) line $M = 1.2$, although earlier Erdmann[6] had started from a line along which the velocity is parallel to the axis.

In the present note we describe a method which has been used in the design of a set of new nozzles at the Institute for Aerodynamics at the Federal Institute of Technology in Zurich. This method has the feature in common with the one described in reference 12 that the initial line of the characteristic net is determined by an analytical method. However, not the line M = const. but the *Machline* originating from the throat of the nozzle is used as carrier of the initial data. This line, which we call S-line (or simply S) in view of its peculiar shape, has been determined experimentally by reconstruction of the flow from the geometry and the pressure distribution of previous nozzles and analytically by considerations in the theory of characteristics and by a power-series expansion of the velocity potential of the flow. In the analytical work the basic assumption of references 1, 10, and 12, that the velocity distribution on the centerline is linear, is no longer made. The geometrical data of the S-line are expressed directly in terms of three geometrical parameters of the nozzle, namely (i) width of the throat, (ii) curvature at the throat, and (iii) rate of change of curvature at the throat.* Full details of the method including a discussion of the boundary-layer effects and comparisons with experimental results will be given in a forthcoming paper. Here we shall only announce without proofs some of the analytical results.

The following notations will be used (see also Fig. 1):

ω	=	Prandtl-Meyer angle of expansion
α	=	slope of the streamlines
γ	=	adiabatic exponent of the gas considered (= 1.4 for air)
O	=	sonic point on the nozzle axis
T	=	throat of the nozzle, starting point of the S-line
A	=	point of intersection of S-line and nozzle axis
W	=	turning point of the S-line
M	=	point of maximum slope in the converging part of the nozzle
R, r	=	radius of curvature

O is also the origin of a (x, y)-coordinate system (positive x-axis coinciding with the nozzle axis). Small letters with a $\sim$ (such as $\tilde{x}$, $\tilde{y}$) refer to the S-line, capitals to the wall.

(2) Aerodynamic Properties of the S-Line

Because S is a characteristic line, $\omega + \alpha = \omega_T$ on S. Between T and W the characteristics intersecting S are compression lines, thus $\tilde{y}'' \leqq 0$ between T and W. Between W and A the intersecting characteristics are expansion lines and therefore $\tilde{y}'' \geqq 0$ there. The characteristic intersecting S at W originates at 0. On this characteristic, $\omega - \alpha = \omega_0 = 0$. Therefore at W,

$$\omega_W = \alpha_W = (1/2)\omega_T$$

This relation is exact, and no simplifying assumptions have been made in its derivation. It shows that between T and W the S-line is crossed by compression lines whose total strength amounts to $(1/2)\omega_T$. Since ω_T is not negligible,† the effect of this compression on the downstream region, if not properly corrected, can be considerable.‡ In particular it appears that method (b) mentioned in the introduction yields good results only for nozzles with a very flat inlet, for even if the transonic part of the nozzle is obtained correctly by backwards construction starting in the diverging part, these compression lines coming from the S-line will not be recovered.

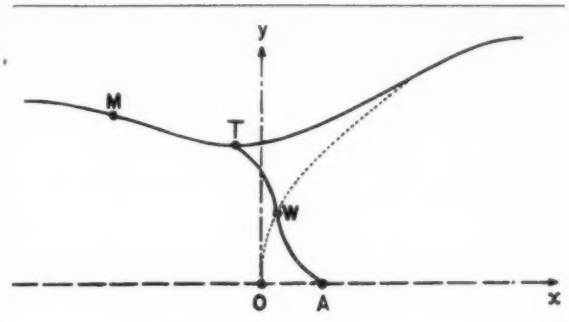

Fig. 1.

(3) Geometrical Properties of the S-Line

Since the whole characteristic net depends on the shape of the initial line, it is important to know S as exactly as possible. We characterize S geometrically by expressing coordinates, slope, and radius of curvature at each of the three points T, W, and A in terms of the three variables Y_T, R_T, and

$$k_T' = \left[\frac{d(1/R)}{dX}\right]_{X=X_T}$$

This last quantity can be interpreted geometrically as follows: one assumes for the nozzle contour the equation

$$Y - Y_T = \frac{1}{2R_T}(X - X_T)^2 + \frac{k_T'}{6}(X - X_T)^3$$

If this were exact, one had between the maximum slope in the upstream part and k_T' the relation

$$Y_M' = -\frac{1}{2}\frac{1}{k_T' R_T^2}$$

With the aid of the auxiliary quantities

$$p = \frac{Y_T}{R_T}$$

$$q = \sqrt{\gamma + 1}\, R_T^{3/2}\, y_T^{1/2} k_T'$$

these twelve relations (of which some are necessarily trivial) can be expressed as follows:

$$\tilde{x}_T = \frac{\sqrt{\gamma+1}}{6} Y_T p^{1/2}\left\{1 + \frac{2\gamma - 15}{60} p\right\}$$

$$\tilde{y}_T = Y_T$$

$$\tilde{y}_T' = -\frac{\sqrt{3}}{\sqrt{\gamma+1}} p^{-1/2}\left\{1 + \frac{10q - 8\gamma + 15}{90} p\right\}$$

$$\tilde{r}_T = \frac{\sqrt{3}+1}{\sqrt{\gamma+1}} Y_T p^{-1/2}\left\{1 + \frac{10\sqrt{3}q + (-3+4\sqrt{3})\gamma - 45}{90} p\right\}$$

$$\tilde{x}_W = \frac{\sqrt{\gamma+1}}{3.2^{3/2}} Y_T p^{1/2}\left\{1 + \frac{(-20 - 10\sqrt[3]{2})q + (4 - \sqrt[3]{2})\gamma - 70}{180} p\right\}$$

$$\tilde{y}_W = \frac{1}{\sqrt[3]{2}\sqrt{3}} Y_T\left\{1 + \frac{(5 - 10\sqrt[3]{2})q + (18 - 7\sqrt[3]{2})\gamma + 45}{270} p\right\}$$

* Mathematically this means that the nozzle contour in the transonic region is approximated by a polynomial of third degree.

† We measured $\omega_T = 4$ degrees in one $M = 1.66$-nozzle.

‡ It does not seem impossible that the sudden decrease in M, which was observed in reference 10 near the inflection point of several nozzles and which cannot be explained completely by boundary-layer effects, is due to this compression.

$$\tilde{y}_W' = -\frac{\sqrt[3]{2}\sqrt{3}}{\sqrt{\gamma+1}}\,p^{-1/2}\times \left\{1+\frac{10q+(4-6\sqrt[3]{2})\,\gamma+(15-10\sqrt[3]{2})}{90}\,p\right\}$$

$$\tilde{r}_W = \infty$$

$$\tilde{r}_a = \frac{\sqrt{\gamma+1}}{3}\,Y_T p^{-1/2}\left\{1+\frac{-5q+2\gamma}{30}\,p\right\}$$

$$\tilde{y}_A = 0$$

$$\tilde{y}_A' = -\frac{\sqrt{3}}{\sqrt{\gamma+1}}\,p^{-1/2}\left\{1+\frac{10q-8\gamma+15}{90}\,p\right\} \quad (=y_T')$$

$$\tilde{r}_A = \frac{2}{\sqrt{\gamma+1}}\,Y_T p^{-1/2}\left\{1+\frac{\gamma+9}{6}\,p\right\}$$

These relations have to be interpreted as leading terms of power series expansions in p. In order that the approximations be good, the values of the curly brackets must therefore be close to 1. All formulas have been derived from a general power series expansion of the velocity potential. In that expansion sufficiently many terms have been taken into account, so that the coefficients in the above formulas are definite.* It is seen that the influence of q (and hence of the upstream geometry of the nozzle) is only of the second order.

From the above data it is possible to interpolate the complete S-line with sufficient accuracy either graphically or analytically.

(4) Concluding Remarks

Three nozzles for $M = 1.37$, 1.66, and 1.27, respectively, of which the last was constructed completely on the basis of the theory presented in this note, have been tested thoroughly. It was found that the discrepancies between the theory and the experiment, expressed in terms of ω, are less than one quarter of a degree, whereas for ω_T the discrepancy between *first order* theory (curly brackets neglected) and experiment amounted to as much as 2 degrees.

All characteristic nets have been constructed graphically. This seemed completely adequate for the present purpose. If a very high accuracy is desired, however, it is possible today to compute characteristic nets on fast electronic computers.† The objections raised in reference 7 against the method of characteristics are thus certainly no longer justified.

Finally it should be pointed out that the technique outlined above can be applied no matter what hypothesis has been adopted for the shaping of the downstream part of the nozzle. In particular, it can be used in connection with the method of continuous wall curvature as proposed by Evvard and Marcus[11] and in reference 12. In the case of the new Zurich nozzles the walls were shaped by an iteration method in such a way as to render the decrease of the pressure gradient as uniform as possible.

References‡

[1] Meyer, Th., *Ueber zweidimensionale Bewegungsvorgänge in einem Gas, das mit Ueberschallgeschwindigkeit strömt*, Dissertation, Göttingen, 1908.

[2] Preiswerk, E., *Anwendung gasdynamischer Methoden auf Wasserströmungen mit freier Oberfläche*, Mitteilungen aus dem Institut für Aerodynamik, Eidgenössische Technische Hochschule, Zürich, No. 7, 1938.

[3] Busemann, A., *Lavaldüsen für gleichmässige Ueberschallströmungen*, Zeitschrift des Verbandes deutscher Ingenieure 84, pp. 857–862, 1940.

[4] Kisenko, M. S., *Comparative results of tests on several different types of nozzles*, NACA TM No. 1066, 1944.

[5] Puckett, A. E., *Supersonic nozzle design*, Journ. Appl. Mech. 13, pp. A265–A270, 1946.

[6] Erdmann, S. F., *Note on the problem of initial values in the design of supersonic nozzles in connection with a measured velocity distribution*, National Luchtvaartlaboratorium: NLL Report No. F 21, 1947.

[7] Foelsch, K., *A new method of designing two-dimensional Laval nozzles for a parallel and uniform jet*, Report No. NA-46-235-2, North American Aviation, Inc., Inglewood, Calif., 1947.

[8] Lighthill, M. J., *The hodograph transformation in transonic flow. I. Symmetrical channels*. Proc. Roy. Soc. London 191, pp. 323–341 (1947).

[9] Courant, R., and Friedrichs, K. O., *Supersonic flow and shock waves*, p. 380, New York, 1948.

[10] Sauer, R., *Einführung in die theoretische Gasdynamik*, 2. Aufl., Berlin-Göttingen-Heidelberg, 1951, S. 98.

[11] Evvard, J. C., and Marcus, L. R., *Achievement of continuous wall curvature in design of two-dimensional symmetrical supersonic nozzles*, NACA TN No. 2616 (1952).

[12] Harrop, P., Bright, P. I. F., Salmon, J., and Caiger, M. T., *The design and testing of supersonic nozzles*, Ministry of supply, Aeronautical Research Council Reports and Memoranda, R & M No. 2712 (1953).

[13] Projects and Publications of the National Applied Mathematics Laboratories, October through December, 1953. NBS Report No. 3119 (1954), p. 41.

* In particular, they are free from the inconsistency which hobbles the analytical work of reference 12.

† See reference 13, where such a computation on the National Bureau of Standards Eastern Automatic Computer (SEAC) is described.

‡ We are indebted to Dr. R. Lehnert and Dr. R. K. Squires, both from the Naval Ordnance Laboratory, for calling our attention to references 7, 11, and 12.

Some Corrections and Further Contributions to "Ripple-Type Buckling of Sandwich Columns"[1]

A. C. Eringen

Associate Professor, Division of Engineering Sciences, Purdue University, Lafayette, Ind.

October 4, 1954

In a recent paper,[2] Seide has pointed out that the plus sign in front of a term, namely, $\sigma_y(x, 0)$ in the first of Eqs. (6) of my paper should be changed to minus. Seide has rightfully shown that this sign mistake is responsible for finding asymmetrical buckling shapes in place of symmetrical or antisymmetrical shapes that were the results of previous studies for simply supported sandwich columns. I have since then checked the whole computation once more and found a few other typographical errors and some additional results. I, therefore, wish to make these corrections in the order of the equation numbers of my paper.

(i) (+) sign in front of $\sigma_y(x, 0)$ in Eq. (6) should be (−).

(ii) As a result of (i), (+) signs in front of $V_{0,y}(m, 0)$ and $V_{t,y}(m, 0)$ in Eq. (7) and in Eq. (11) should be (−).

(iii) Replace Eq. (14) by

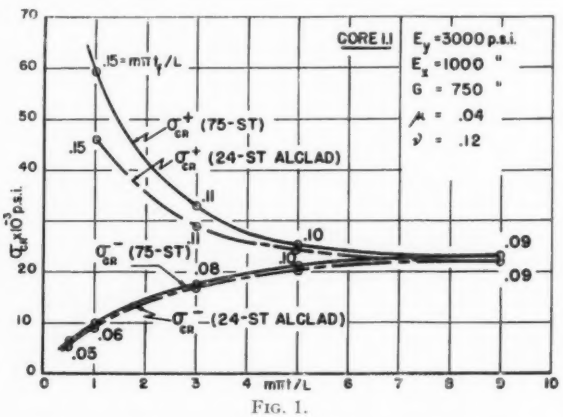

Figs. 1–4, 6 and 7. Buckling stress of a sandwich column $E_x/2G > \mu + (\mu/\nu)^{1/2}$ (with yield correction).

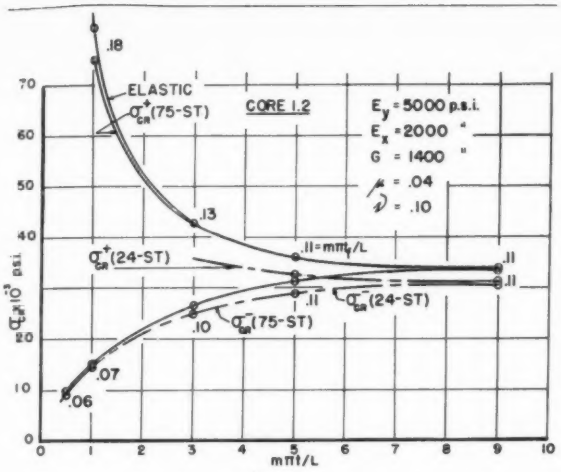

FIG. 2.

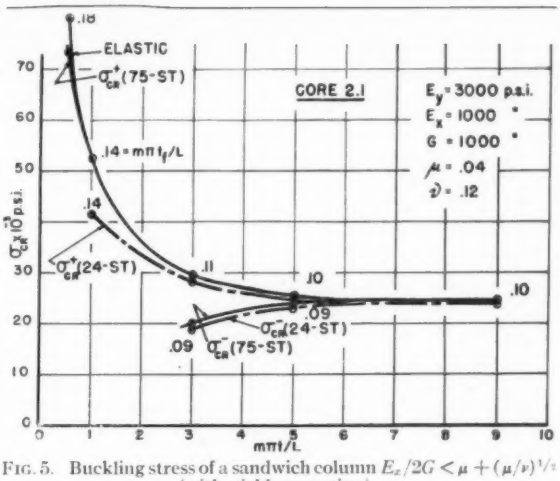

FIG. 5. Buckling stress of a sandwich column $E_x/2G < \mu + (\mu/\nu)^{1/2}$ (with yield correction).

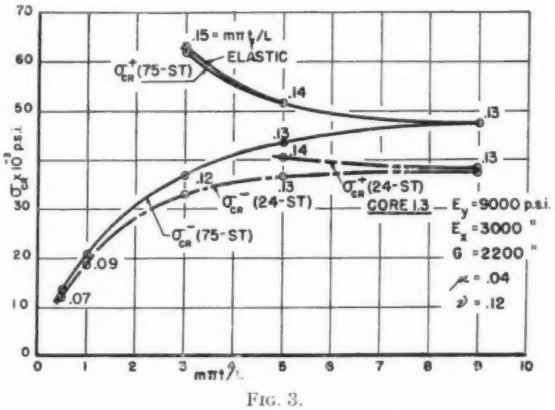

FIG. 3.

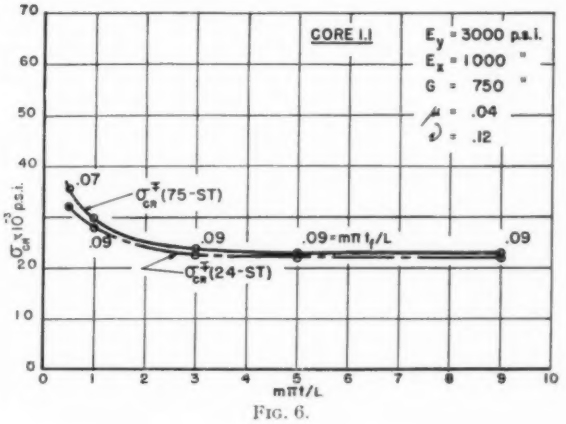

FIG. 6.

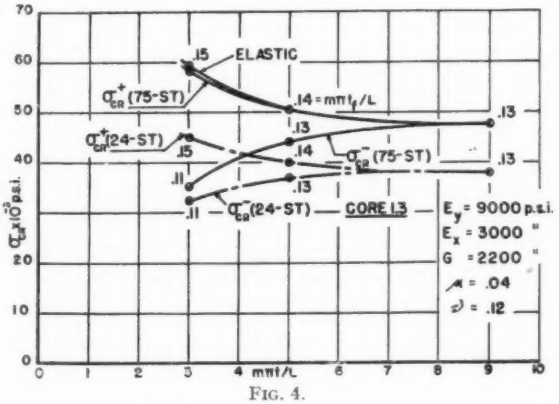

FIG. 4.

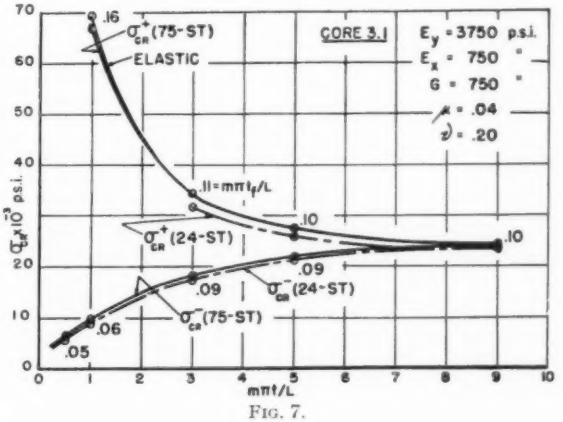

FIG. 7.

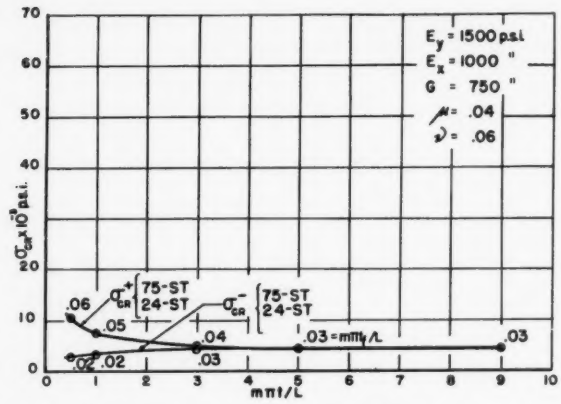

FIG. 8. Buckling stress of a sandwich column $E_x/2G < \mu + (\mu/\nu)^{1/2}$ (with yield correction).

$$\sigma_{cr} = (E_f/12)\,(m\pi t_f/L)^2 + (G/2)\,[u_1(m,0) \mp u_2(m,0)] + [E_y/(1-\mu\nu)]\,(L/m\pi t_f)\,[v_1(m,0) \pm v_2(m,0)] \quad (14)$$

(iv) Use $(\sinh 2z_1't - j' \sin 2z_2't)$ in place of

$$(\sinh^2 z_1't - j' \sin^2 z_2't)$$

in $v_1'(m,0)$ of Eq. (17).

(v) Use $(\sinh^2 z_1't - j' \sin^2 z_2't)^{-1}$ in place of

$$(\sinh^2 z_1't - j' \sin^2 z_2't)$$

in $v_2'(m,0)$ of Eq. (17).

(vi) Replace Eq. (18) by

$$\sigma_{cr} = \mp \left\{ \left[(E_f/12)\,(m\pi t_f/L)^2 + \frac{1}{2} G \cdot u_1(m,0) + E_y(1-\mu\nu)^{-1} \cdot (L/m\pi t_f)\, v_1(m,0) \right]^2 - \left[\frac{1}{2} G \cdot u_2(m,0) - E_y (1-\mu\nu)^{-1} (L/m\pi t_f)\, v_2(m,0) \right]^2 \right\}^{1/2}$$

(vii) Omit Section (5a) and (5b) of the paper.

It is curiously interesting that with this (−) sign correction the buckling formulas, Eqs. (14) and (18), are changed radically. Eq. (14) does not contain a radical sign, and Eq. (18) does not have terms other than the ones contained in a radical. Consequently, by taking upper or lower signs we obtain antisymmetrical or symmetrical buckling of previous writers. Of course, the argument of Sections (5a) and (5b) of my paper is valid for sandwich columns having unidentical faces. Even a slightest difference in the thickness or in the elastic properties will give asymmetrical buckling pattern. This is also true for other types of edge conditions. Eqs. (18) give buckling stress under pure bending moments at the edges of the sandwich column. The (−) sign of the radical in this equation has no physical significance, since it gives negative buckling stress.

New calculations were carried out on an IBM Card Program Calculator based on the data shown on Figures given in reference 1. We found that these curves hardly need modification, for the errors were less than a few per cent in the minimum critical loads obtained previously. This is probably due to the fact that cores chosen there were all rather soft. Thus, the resulting curves shown there can be used without alteration. We have, however, calculated new type minimum critical stresses that were not included in reference 1 and have extended the range of parameters so that the present curves contain the minimum critical stresses of previous computations as a point on each curve. We, therefore, give (see Figs. 1–8) a set of curves for $\sigma_{cr\ min.}$ vs. $(m\pi t/L)$ for various core and face combinations which we hope will be useful in engineering applications. On these curves the numbers next to the marked point denote the value of $(m\pi t_f/L)$ at which $\sigma_{cr\ min.}$ occur. Values of $\sigma_{cr\ min.}$ are corrected for yielding in accordance with the Kármán-Engesser formula represented by Fig. 15 of reference 1.

Seide also uses some continuity conditions [Eqs. (5) and (6) of reference 2] replacing the usual simplifications indicated in his paper by Eqs. (7) and (8) of the most of previous authors. I have had an occasion before to estimate the effect of these simplifications and had found that for

$$E_c t_c / E_f t_f \ll 1$$

this effect is negligibly small. Here E_c and E_f are moduli of elasticity, and t_c and t_f are the thickness of the core and faces, respectively. This condition is, of course, essential in practice. Moreover, this approximation—namely, $u = 0$ at the contacting surfaces—is consistent with the spirit of the linear theory.

Seide states also that, at least for the problem of buckling under compressive edge loads, the elaborate solution of a boundary value problem is unnecessary. This, of course, is false. For the edge conditions Eq. (2) of his paper—i.e., $\sigma_x(0,y) = \sigma_x(L,y) = 0$ for the core—is incorrect and only represents an approximation for sandwich columns having soft cores.

Goodier[3] gave an analysis that takes this effect into account in one case. As soon as $\sigma_x(0,y) \neq \sigma_x(L,y) \neq 0$, we cannot use the solutions of the type of Eqs. (14) of Seide's paper. Thus we need to solve a mixed type boundary value problem to which Seide objects. In my paper, I used conditions (2) only as a simplifying assumption. Actually I need not use it, since a complete solution of the boundary value problem taking into account the edge values of σ_x at $x = 0, L$ were given in reference 13 of my paper, which is being published presently.[4]

Finally, the author is indebted to Mr. J. W. Dunkin for carrying out the computations on the IBM Card Program Calculator.

REFERENCES

[1] Eringen, A. C., Journal of the Aeronautical Sciences, Vol. 19, No. 6, pp. 409–417, June, 1952.

[2] Siede, Paul, *Comments on "Ripple-Type Buckling of Sandwich Columns,"* Journal of the Aeronautical Sciences, Vol. 21, No. 4, pp. 282–286, April, 1954.

[3] Goodier, J. N., *Cylindrical Buckling of Sandwich Plates,* Journal of Applied Mechanics, Vol. 13, No. 4, p. 253, 1946.

[4] Eringen, A. C., *The Solution of a Class of Mixed-Mixed Boundary Value Problems in Plane Elasticity,* Proceedings of the Second National Congress, Ann Arbor, Mich., June, 1954.